

AIAA 2018-2019 Engine Design Competition

**F A R A** 

**Sharif University of Technology**

STS-1000: A Candidate Turboshaft Engine  
for Hybrid Electric Medium Altitude Long  
Endurance Search and Rescue UAV

High Power to Weight  
Low Fuel Consumption  
Modular & Compact

# SIGNATURE SHEET



**Prof. Kaveh Ghorbanian**  
Faculty Advisor



**M. Reza AminiMagham**  
Project Advisor



**Alireza Ebrahimi**  
Team Leader  
952166



**Amir Nazemi**  
981123



**Abolfazl Zolfaghari**  
919547



**Hojjat Etemadianmofrad**  
964808



**Vahid Danesh**  
964807



**M. Mahdi Asnaashari**  
952842



**Saeide Kazembeigi**  
978931



**Mahdi Jamshidiha**  
688249



**Amirreza Saffizadeh**  
937080



# Executive Summary

This report proposes a turboshaft engine referred to “Sharif TurboShaft 1000 (STS-1000)” as a candidate engine to replace the baseline engine TPE331-10 for the next generation “Hybrid Electric Medium Altitude Long Endurance Search and Rescue UAV” by the year 2025.

STS-1000, unlike the baseline engine, is a split single-spool turboshaft engine. The hot gas generator is a single spool with a single stage radial compressor, a reverse annular combustion chamber, and an uncooled single stage axial compressor turbine. The required shaft power is produced by a two stage axial power turbine on a separate spool which passes through the spool of the core engine and is intended to drive a power generator at the cold end of the engine. The air intake is of S-type and the exhaust duct has circular cross section.

Compared to TPE331-10, STS-1000 has a higher turbine inlet temperature, a lower stage number for the air compressor, and requires less mass flow rate. Hence, STS-1000 has a lower weight due to both shorter engine length as well as smaller air capture area. This further enables the proposed engine to have an enhanced engine-airframe integration. Furthermore, the engine components have higher efficiencies due to recent and foreseen technological advancements in aerodynamics and materials. As a consequence, STS-1000 has not only higher thermal efficiency and lower specific fuel consumption but also higher power-to-weight ratio supporting the UAV for larger loiter time and/or heavier payload.

It should be pointed out that while for some part of the engine design calculations commercial software like GSP11 and MESYS is used, in-house codes are developed in the MATLAB® environment to: (1) compute the cycle analysis of both TPE331-10 and STS-1000 engines at the design point and off-design point conditions, (2) identify the design point of STS-1000 at loiter, (3) perform the aero-thermodynamic analysis across the AC, CT, and PT, the air intake, and the exhaust duct.

While STS-1000 might be altered by including other limiting parameters (i.e., modularity, reliability, manufacturing procedure, maintenance, cost, etc.); however, we believe that the proposed design methodology is in the right direction. One may recall that aircraft engine design is an art and there is not a unique solution to a specific aircraft engine RFP. Finally, the following tables summarize the results of main importance.

**Table. A: STS-1000 Compliance Matrix**

<b>Performance</b>			
<b>Cruise Speed [KTS]</b>	220		
<b>Loiter Speed [KTS]</b>	190		
<b>Mission Fuel Burn [lb]</b>	4033.4		
<b>Cruise PSFC [lb/hr.hp]</b>	0.3997		
<b>Take-off PSFC [lb/hr.hp]</b>	0.4179		
<b>Loiter PSFC [lb/hr.hp]</b>	0.4026		
<b>Engine Weight [lb]</b>	253.42		
<b>Engine Diameter [in]</b>	21		
<b>Engine Length [in]</b>	37		
<b>Trade Studies</b>			
<b>Engine Cycle Design Area Page#</b>	<b>Engine Cycle Carpet Plot Page#</b>	<b>Cycle Summary Page#</b>	<b>Final Engine Flowpath Page#</b>
11	10	13	80
<b>Compressor Design Information Page#</b>	<b>Compressor Velocity Triangles Page#</b>	<b>Turbine Design Information Page#</b>	<b>Turbine Velocity Triangles Page#</b>
18	22 & 23	32	33

**Table. B: Engine Summary Table**

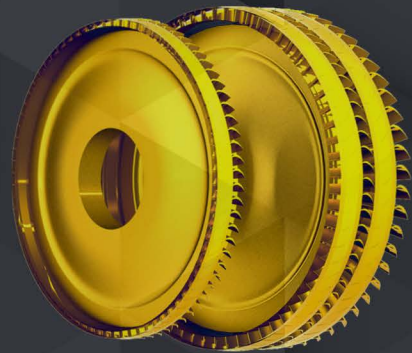
<b>Summary Data</b>	
<b>Design MN</b>	0.294
<b>Design Altitude [ft]</b>	7000
<b>Design Shaft Horsepower [hp]</b>	603
<b>Design PSFC [lb/hr.shp]</b>	0.4026
<b>Design Overall Pressure Ratio</b>	10.098
<b>Design T4.1 [°R]</b>	2150
<b>Design Engine Pressure Ratio</b>	10.098
<b>Design HPC Pressure Ratio</b>	10.2
<b>Design Chargeable Cooling Flow [%@25]</b>	0
<b>Design Non-Chargeable Cooling Flow [%@25]</b>	0
<b>Design HP Turbine Adiabatic Efficiency [%]</b>	93
<b>Design LP Turbine Adiabatic Efficiency [%]</b>	93
<b>Design HP Compressor Adiabatic Efficiency [%]</b>	88
<b>Design Shaft Power Loss [hp]</b>	3.78
<b>Design HP Shaft RPM</b>	40000
<b>Design LP Shaft RPM</b>	22000
<b>Design Shaft Off-Take Power [hp]</b>	30



- Single Stage Air Centrifugal Compressor AC (PR = 10.2)
- Adiabatic Efficiency : 88%
- Material : Titanium 6Al-4V



- Reverse Annular Combustion Chamber
- Adiabatic Efficiency : 99.5%
- Total Pressure Loss : 5%
- Material : SiC/SiC CMC



- Single Stage Axial Compressor Turbine CT (PR = 2.9)
- Two Stage Axial Power Turbine PT (PR = 3.2)
- Adiabatic Efficiency (CT & PT) : 93%
- CT Rotational Speed : 40,000 RPM
- PT Rotational Speed : 22,000 RPM
- Blade Material : SiC/SiC CMC
- Disk Material : Inconel 718



- 67.0% Higher Power to Weight Ratio at SLS
- 35.0% Lower Weight
- 10.0% Higher Power at SLS
- 30.5% Lower Fuel Consumption at Loiter
- 28.7% Lower Fuel Consumption at Cruise
- 30.0% Lower Operating Cost

# Contents

Contents.....	iii
List of Symbols.....	v
List of Figures.....	vii
List of Tables.....	ix
Chapter 1 Introduction.....	1
Chapter 2 Cycle Design.....	2
2.1 Meeting RFP Requirements .....	2
2.2 Engine Type Selection .....	5
2.3 Engine Configuration.....	5
2.4 TPE331-10 Cycle Validation .....	7
2.5 Design Point Selection .....	9
2.6 Method of Approach .....	9
2.7 STS-1000 Final Cycle Design and Analysis .....	12
2.8 UAV Performance Analysis.....	14
2.9 Overall Performance Comparison.....	15
Chapter 3 Centrifugal Compressor Design.....	16
3.1 Components Overview.....	16
3.2 Characteristics .....	18
3.3 Geometry Construction .....	25
3.4 Compressor Inflow Data .....	26
Chapter 4 Axial Turbine Design.....	28
4.1 Configuration .....	28
4.2 Design Methodology.....	29
4.3 Material Selection .....	30
4.4 Design Point Selection.....	30
4.5 Losses.....	33
4.6 Gas Path Calculation.....	33
4.7 Aerothermodynamics .....	34
4.8 Blade Design and Annulus.....	35
4.9 Throat Design.....	36
4.10 Hand Calculation.....	38
4.11 Smith Chart .....	40
4.12 Airfoil Generation .....	40
4.13 Turbine Mechanical Analysis.....	41
4.14 Turbine Inflow Data.....	42
Chapter 5 Combustion Chamber Design.....	43
5.1 Pre-Diffuser Design.....	43
5.2 Air Partitioning.....	44

5.3	Combustor Sizing.....	45
5.4	Fuel Injection .....	48
5.5	Combustor Configuration.....	48
5.6	Emission.....	49
5.7	Combustor Inflow Data.....	49
Chapter 6	Air Intake and Exhaust Duct Design.....	50
6.1	Intake Characteristics .....	50
6.2	Intake Sizing.....	50
6.3	Intake Geometry.....	52
6.4	FOD Problem.....	54
6.5	Anti-icing or De-icing .....	54
6.6	Exhaust Duct Design.....	55
6.7	Noise Control .....	56
6.8	Material Selection .....	57
6.9	Intake & Exhaust Duct Inflow Station Data.....	57
6.10	Intake Design Procedure .....	58
Chapter 7	Mechanical Analysis.....	59
7.1	Material and Manufacturing.....	59
7.2	Stress Analysis .....	60
7.3	System Vibration Analysis.....	60
7.4	Bearing Selection and Positioning .....	62
7.5	Shaft Design.....	64
7.6	Shafts' Rotor Dynamic Analysis.....	66
Chapter 8	Identification and Selection of Engine Subsystems.....	71
8.1	Oil and Lubrication System.....	71
8.2	Fuel System.....	73
8.3	Engine Control System.....	73
Chapter 9	Cost Analysis.....	75
9.1	Unit Cost .....	75
9.2	Maintenance Cost.....	75
9.3	Operating Cost .....	76
Chapter 10	Engine Weight Estimation.....	78
Chapter 11	Engine Flow Path and 3D CAD .....	79
Chapter 12	Conclusion and Recommendation .....	81
References	.....	82

# List of Symbols

## Latin

Symbol	Unit	Description	Symbol	Unit	Description
A	[in <sup>2</sup> ]	Area	PF		Pattern Factor
AR	-	Wedge Diffuser Area Ratio	Pf		Profile Factor
AS		Aspect Ratio	PR		Pressure Ratio
B		Impeller Blockage Factor	PSFC	[lb/hp.hr]	Power Specific Fuel Consumption
BL		Impeller Blade Loading	PT		Power Turbine
C	[ft/s]	Absolute Velocity	R	[in]	Radius
$C_p$		Pressure Recovery Coefficient	°R		Degree of Reaction
$C_p$	[BTU/lb°F]	Specific Heat Capacity	T	[°R]	Temperature
CLP		Combustor Loading Parameter	TIT	[°R]	High Pressure Turbine Inlet Temperature
CPR		Compressor Pressure Ratio	U	[ft/s]	Blade Speed
CT		Compressor Turbine	V	[ft/s]	Actual Velocity
D	[in]	Diameter	W	[ft/s]	Relative Velocity
DF		Diffusion Factor	W	[lbf]	Weight
DR		Diffusion Ratio	W	[in]	Width
E	[ksi]	Modulus of Elasticity	Z		Number of Blades
F.S		Safety Factor	Zw		Zweifel Number
H	[in]	Length of Blade	b	[in]	Diffuser Passage Width
HGG		Hot Gas Generator	b	[in]	Impeller Axial Width
HPT		High Pressure Turbine or Compressor Turbine	c	[in]	Chord
I	[in <sup>4</sup> ]	Moment of Inertia	d	[in]	Diameter
$K_f$		Combined Bending Load Factor	e		Polytropic Efficiency
$K_\tau$		Combined Torsion Load Factor	f		Fuel-Air Ratio
L	[in]	Length	$\dot{m}$	[lb/s]	Mass Flow Rate
LPT		Low Pressure Turbine	n		Number of Blades
M		Mach Number	r	[in]	Radius
MTOW	[lb]	Max Take-Off Weight	s	[in]	Blade Spacing
N	[rev/s]	Rotational Speed	t	[in]	Thickness
O	[in]	Throat			
OPR		Overall Pressure Ratio			
P	[hp]	Power			
P	[psi]	Pressure			

## Greek Symbols

Symbol	Unit	Description	Symbol	Unit	Description
$\alpha$	[°]	Absolute Flow Angle	$\rho$	[slug/in <sup>3</sup> ]or[lb/in <sup>3</sup> ]	Density
$\beta$	[°]	Relative Flow Angle	$\sigma$		Solidity
$\gamma$		Specific Heat Ratio	$\sigma$	[ksi]	Stress
$\eta$		Total to Total Adiabatic Efficiency	$\phi$		Fuel Equivalence Ratio
$\theta$	[°]	IGV Angle	$\varphi$		Flow Coefficient
$\mu$		Slip Factor	$\psi$		Stage Loading
$\Lambda$	[°]	Stager angle	$\omega$	[RPM]	Rotational Speed
$\pi$		Total Pressure Ratio			

## Subscript

Symbol	Description	Symbol	Description
D	Diffuser	m	Static Moment
DZ	Dilution Zone	m	mid
I	Impeller	t	Total
L	Liner	t	tip
Mech	Mechanical	r	Radial
PZ	Primary Zone	s	Static
SZ	Secondary Zone	s	Shroud
a	Cyclic Moment	ref	Reference
ax	Axial	rel	Relative
b	Buner	f	Fuel
c	Compressor	z	Axial
h	hub	$\theta$	Tangential
j	Jet flow		

# List of Figures

Figure 1.1: TPE331-10 Engine.....	1
Figure 2.1: CPR vs. Rotor Speed [3] .....	3
Figure 2.2: Turboshaft Engine Schematic View [4].....	3
Figure 2.3: Selection Methodology for the Design Point .....	4
Figure 2.4: Baseline Engine Architecture in GSP11.....	7
Figure 2.5: Power and PSFC Variation vs. CPR.....	9
Figure 2.6: Carpet Plot of PSFC vs. TIT on CPR Constant Lines.....	10
Figure 2.7: Allowable Design Area at Loiter.....	10
Figure 2.8: Allowable Design Area at Loiter with Specified Values in Boundary Conditions .....	11
Figure 2.9: Target Engine Architecture in GSP11.....	12
Figure 2.10: UAV Mission Profile .....	14
Figure 3.1: Compressor Schematic Illustration and Station Numbering .....	16
Figure 3.2: Effect of Prewhirl on Impeller Inlet and Discharge Mach Numbers [7] .....	16
Figure 3.3: Effect of Reducing Radius Ratio on Inlet Relative Mach Number [7].....	20
Figure 3.4: Typical Impeller Style [5] .....	21
Figure 3.5: Impeller Inlet Velocity Triangles at Hub, Mid and Tip.....	22
Figure 3.6: Impeller Exit Velocity Triangle .....	23
Figure 3.7: Flow Regime Chart for Wedge [12].....	23
Figure 3.8: Allowable Stress vs. Temperature for Typical Engine Materials [4] .....	25
Figure 3.9: Impeller Geometrical Construction Method.....	26
Figure 3.10: Compressor Design Flow Chart .....	27
Figure 4.1: Overall Configuration of the CT&PT.....	28
Figure 4.2: Rated Speeds of Existing High-Speed Machines [14].....	28
Figure 4.3: Cooling Technology Trend .....	30
Figure 4.4: Contour of CT Candidate Design Points.....	31
Figure 4.5: Contour Candidate Design Points of PT .....	32
Figure 4.6: Distribution of Loss Types.....	33
Figure 4.7: Stage Hub to Shroud Radius Ratio[20] .....	33
Figure 4.8: Stators And Rotors of STS-100 Turbines Pattern [19].....	34
Figure 4.9: Velocity Triangles Across the Turbines.....	34
Figure 4.10: Side View of CT.....	35
Figure 4.11: Side View of PT .....	36
Figure 4.12: Throat of Blades [19] .....	36
Figure 4.13: Turbine Design Approach .....	39
Figure 4.14: Smith Chart and Operating Point of CT and PT [18].....	40
Figure 4.15: Turbine Blade Profile Schematic [21].....	40
Figure 4.16: Centrifugal Stress of Disk and Blades [4] .....	41
Figure 4.17: Gas bending Stress of Blades [4] and [35].....	41

Figure 4.18: Approximate Rule for Section Module [22].....	41
Figure 5.1: Reverse Flow Annular Combustor [23] .....	43
Figure 5.2: Regimes of a Flat-Wall Diffuser [3].....	43
Figure 5.3: Influence of Primary Zone Temperature on CO and NO <sub>x</sub> [3].....	44
Figure 5.4: Liner Cooling Techniques[3] .....	45
Figure 5.5: Combustion Efficiency vs. $\theta$ [23] .....	47
Figure 5.6: Airblast Atomizer [23] .....	48
Figure 6.1: Inlet Flow Angle of Attack.....	50
Figure 6.2: Schematic View of the Intake .....	50
Figure 6.3: Subsonic Intake Flow Streamlines, .....	51
Figure 6.4: Intake Throat Area [3] .....	52
Figure 6.5: a) Final Intake Geometry    b) Center Line Equation.....	53
Figure 6.6: Shaft Exit Location.....	53
Figure 6.7: Compressor Entrance .....	54
Figure 6.8: Engine Intake and De-Icing Element .....	55
Figure 6.9: Exhaust Geometry .....	55
Figure 6.10: Helmholtz Resonator [30] .....	56
Figure 6.11: Multi-duct Device [30].....	56
Figure 6.12: Intake Design Approach.....	58
Figure 7.1: Manufacturing of Fiber-glass Composite Schematic .....	59
Figure 7.2: A Centrifugal Compressor Manufacturing Using a Five-axis-CNC .....	59
Figure 7.3: Campbell Diagram of Turbine Disks and Blade .....	63
Figure 7.4: Bearings' Positioning Examples [35].....	64
Figure 7.5: Engine Bearings' Positioning of STS-1000 .....	64
Figure 7.6: Position of the Forces .....	65
Figure 7.7: Cross Sections of Shafts.....	65
Figure 7.8: Schematic of Shafts and Diameter of Each Section .....	65
Figure 7.9: 2D and 3D Schematic of Shafts .....	66
Figure 7.10: Plots of Deflection (a, b), Forces (c), Stresses (d, e), and Moments (f).....	67
Figure 7.11: Campbell Diagram .....	68
Figure 7.12: Shafts Mode Shapes .....	69
Figure 7.13: Shafts Mode Shapes (Continued).....	70
Figure 8.1: A Typical Lubrication System [39].....	71
Figure 8.2: Block Diagram of a Closed-Loop Control System [44]. .....	73
Figure 8.3: Functional Process Diagram of a Simple Engine Control System [45].....	74
Figure 9.1: Operating Cost Comparison .....	76
Figure 9.2: Flowchart of STS-1000 Engine Cost.....	77
Figure 11.1: STS-1000 Cross-section and Flow Path.....	79
Figure 11.2: STS-1000 Engine 3D CAD Model.....	80

# List of Tables

Table 2.1: Baseline Similar Engines Information.....	6
Table 2.2: TPE331-10: Flight & Basic Data at On-Design Condition (Take-off).....	7
Table 2.3: TPE331-10: On-Design Cycle Summary .....	7
Table 2.4: TPE331-10: Component’s Information .....	8
Table 2.5: TPE331-10: Flight & Basic Data at Cruise .....	8
Table 2.6: TPE331-10: Flight & Basic Data at Loiter .....	8
Table 2.7: Target Engine Component Efficiency and Pressure Losses .....	9
Table 2.8: Design Point Specifications.....	12
Table 2.9: STS-1000: Flight & Basic Data at On-Design (Loiter) .....	13
Table 2.10: STS-1000: On-Design Cycle Summary.....	13
Table 2.11: STS-1000: Flight & Basic Data at Cruise.....	13
Table 2.12: STS-1000: Flight & Basic Data at Hot Take-off.....	14
Table 2.13: STS-1000: Flight & Basic Data at Normal Take-off.....	14
Table 2.14: Comparison of General Characteristics Between Target UAV and MQ-9.....	15
Table 2.15: Performance Comparison of STS-1000 to TPE331-10.....	15
Table 3.1: Impeller Type Comparison.....	17
Table 3.2: Design Parameters .....	18
Table 3.3: Design Constraints and Guidelines.....	19
Table 3.4: Compressor Inlet Flow Parameters.....	19
Table 3.5: Impeller Inlet Dimensions .....	20
Table 3.6: Impeller Exit Dimensions.....	21
Table 3.7: Impeller Inlet Velocities and Angles at Hub, Mid and Tip.....	22
Table 3.8: Impeller Exit Velocities and Angles.....	23
Table 3.9: Wedge Diffuser Geometry Parameters .....	24
Table 3.10: Compressor Thermodynamics Properties.....	24
Table 3.11: Disk and Blade Stress.....	25
Table 3.12: Compressor Inflow Data.....	26
Table 4.1: Design Point Selection Criteria .....	30
Table 4.2: Candidate Design Points of CT .....	31
Table 4.3: Candidate Design Points of PT.....	32
Table 4.4: Overall Specifications of Turbines .....	33
Table 4.5: Profile Loss Coefficient of Each Component.....	33
Table 4.6: Blade Dimensions of CT .....	35
Table 4.7: Blade Dimensions of PT.....	36
Table 4.8: Compressor Turbine Aerothermodynamics Result.....	37
Table 4.9: Power Turbine Aerothermodynamics Result.....	37
Table 4.10: Compressor Turbine Flow Path Results .....	37
Table 4.11: Power Turbine Flow Path Results .....	37

Table 4.12: Turbines Stress Analysis .....	42
Table 4.13: CT Inflow Data.....	42
Table 4.14: PT Inflow Data .....	42
Table 5.1: Diffuser Specs .....	44
Table 5.2: Air Partitioning.....	44
Table 5.3: Casing Dimensions.....	46
Table 5.4: Primary Zone Specs.....	46
Table 5.5: Secondary Zone Specs.....	46
Table 5.6: Dilution Zone Specs .....	47
Table 5.7: Main Combustor Length.....	47
Table 5.8: Combustion Efficiency .....	48
Table 5.9: Combustor Inflow Data .....	49
Table 6.1: Intake Design Parameter Assumption [27].....	51
Table 6.2: Intake Flow Thermodynamics Properties.....	51
Table 6.3: Sectional Intake Area.....	52
Table 6.4: Comparison of De-Icing and Anti-Acing .....	54
Table 6.5: Exhaust Duct Characteristics.....	55
Table 6.6: Exhaust Noise Reduction [30].....	56
Table 6.7: Intake Inflow Data .....	57
Table 6.8: Exhaust Inflow Data .....	57
Table 7.1: Components Stress Analysis.....	60
Table 7.2: Components' Blade Natural Frequencies .....	61
Table 7.3: Components' Disk Natural Frequency .....	61
Table 7.4: Components' Disk Natural Frequency .....	62
Table 7.5: Bearing Material Properties.....	64
Table 7.6: Shaft Design Parameters.....	65
Table 7.7: Natural Frequencies of Shafts.....	66
Table 7.8: Shafts Speed Levels.....	68
Table 8.1: AeroShell 500 Oil Properties Compared to Mil-Spec [43].....	72
Table 9.1: Comparison of Maintenance Cost .....	76
Table 10.1: Engine Components Volume, Density, Weight.....	78
Table 10.2: Final Engine Weight.....	78
Table 11.1: Material Properties of each Component .....	79

## Chapter 1 Introduction

The RFP is calling for the candidate engine for the next generation hybrid electric medium altitude long endurance search and rescue UAV. The baseline engine is TPE331-10, a turboprop engine manufactured by Honeywell in 1970 which used in many aircraft and UAVs like Dornier, and MQ-9.

Based on the RFP, the candidate engine should have the following advantages over the baseline engine:

- A minimum of 25% fuel consumption improvement at loiter
- Supporting a flight range greater than 1000 [nm]
- A minimum of 5% power increase at SLS
- A minimum of 10% power to weight ratio improvement at SLS
- Lighter in total weight and lower in cost

As a starting point, design and off-design cycle analysis are performed and validated. Next, a design methodology is developed to identify the design point of the candidate engine. Further, the selected design point is used to design the rotating components of the core engine that is, the air compressor (AC) and the compressor turbine (CT). Once the assurance is obtained that the performance of the AC and CT are in agreement with the cycle and engine design requirements as well as the technological limitations, the remaining main components like the power turbine, combustion chamber, intake, and exhaust are investigated.

We believe that, although the proposed engine in this report could be altered through other performance and limiting parameters (i.e., reliability, manufacturing procedure, maintenance, cost, etc.); however, we are confident of the correction of the design procedure. As knows aircraft engine design is an art and there is not a unique solution to a specific aircraft engine RFP.

**Garrett TPE331 Turboprop Engine**

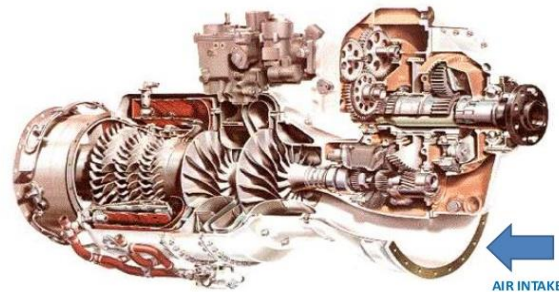


**Figure 1.1: TPE331-10 Engine**

## Chapter 2 Cycle Design

In this chapter, the cycle design of the candidate engine is explained. Further, a philosophy for the selection of the design point is introduced. First, the baseline engine is modeled by GSP11 [2]. Then, a selection methodology is used for the design point. For this purpose, a MATLAB® code is developed. Next, by using GSP11, on-design and off-design analyses of the candidate engine are performed. At the end, the data are compared with those from the RFP [1].

### 2.1 Meeting RFP Requirements

As a starting point, a selection methodology for the design point can enhance the design procedure. Thus, it is necessary to determine the RFP requirements and identify the possible solutions. The RFP requirements are as follows:

- SLS power to weight increase of 10%
- SLS power output within 5% of the baseline
- 25% improvement of fuel consumption at loiter ( $\dot{m}_f$ )

Also, it was mentioned in the RFP that the output power of the target engine should be larger than 603, 690, and 953 horsepower at loiter, cruise, and hot take-off, respectively.

For meeting the RFP requirements, several options are possible. In the following, some of these approaches are explained.

#### 2.1.1 Reduction in Fuel Consumption

Fuel flow of an aerial vehicle is determined by Eq. (2.1):

$$\dot{m}_f = f \cdot \dot{m}_a \quad (2.1)$$

According to Eq. (2.1), there are two ways for reducing the fuel consumption:

1. **Decreasing the fuel-air ratio:** In this method, TIT should be reduced, but this reduction should be compensated by other cycle parameters in order not to affect the cycle output power.
2. **Decreasing the inlet mass flow:** Reduction in diameter of the engine inlet is one method for the inlet mass flow decrement, and this would also, result in weight reduction. It should be noted that this reduction in mass flow should be in balance with the cycle improvements so it would not have an adverse effect on the required output power.

### 2.1.2 Power to Weight Ratio Increment

To increase the power to weight ratio, either power can be increased or the engine weight can be decreased. For weight decrement, volume and dimensions of the components can be optimized. In this project, it is determined to utilize a single stage centrifugal compressor which is one stage less than the baseline engine. However, it should be taken into account that the single stage compressor has to produce the desired pressure ratio. According to Figure 2.1, the desired pressure ratio and efficiency are achievable.

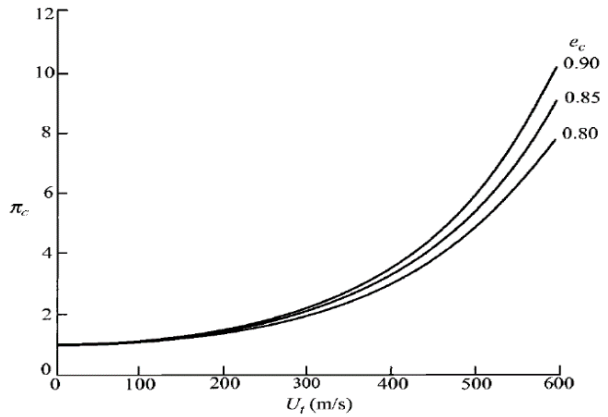


Figure 2.1: CPR vs. Rotor Speed [3]

Another approach to the weight reduction is to reduce the engine diameter which is mentioned in section 2.1.1. This will help both weight and fuel consumption reduction. Of interest for the weight reduction is also the use of enhanced materials in engine components. In this case engine limitations such as TIT and applied stresses should be taken into account. Further, the proposed engine in this report does not use a gearbox which reduces further the engine weight in comparison to TPE331-10 significantly.

### 2.1.3 Power Increase

According to [4], Eq. (2.2) illustrates a relationship for the output power of a turboshaft engine as schematically illustrated in Figure 2.2:

$$P_{\text{load}} = \dot{m}_a (1 + f - b) C_{p_{\text{pt}}} (T_{t_5} - T_{t_6}) \quad (2.2)$$

One approach to increase the output power would be

an increment of the inlet airflow. Further, increasing the turbine inlet temperature would also increase the compressor pressure ratio. Another way for increasing the power is by utilizing components with higher efficiencies. Considering the above mentioned approaches, a selection methodology for the design point is developed, Figure 2.3.

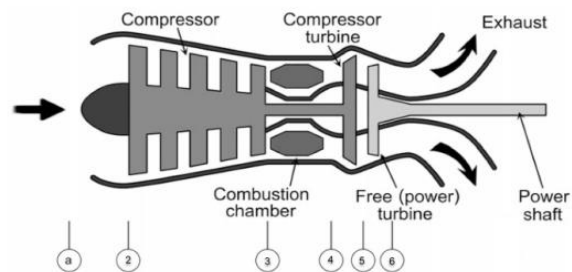


Figure 2.2: Turboshaft Engine Schematic View [4]

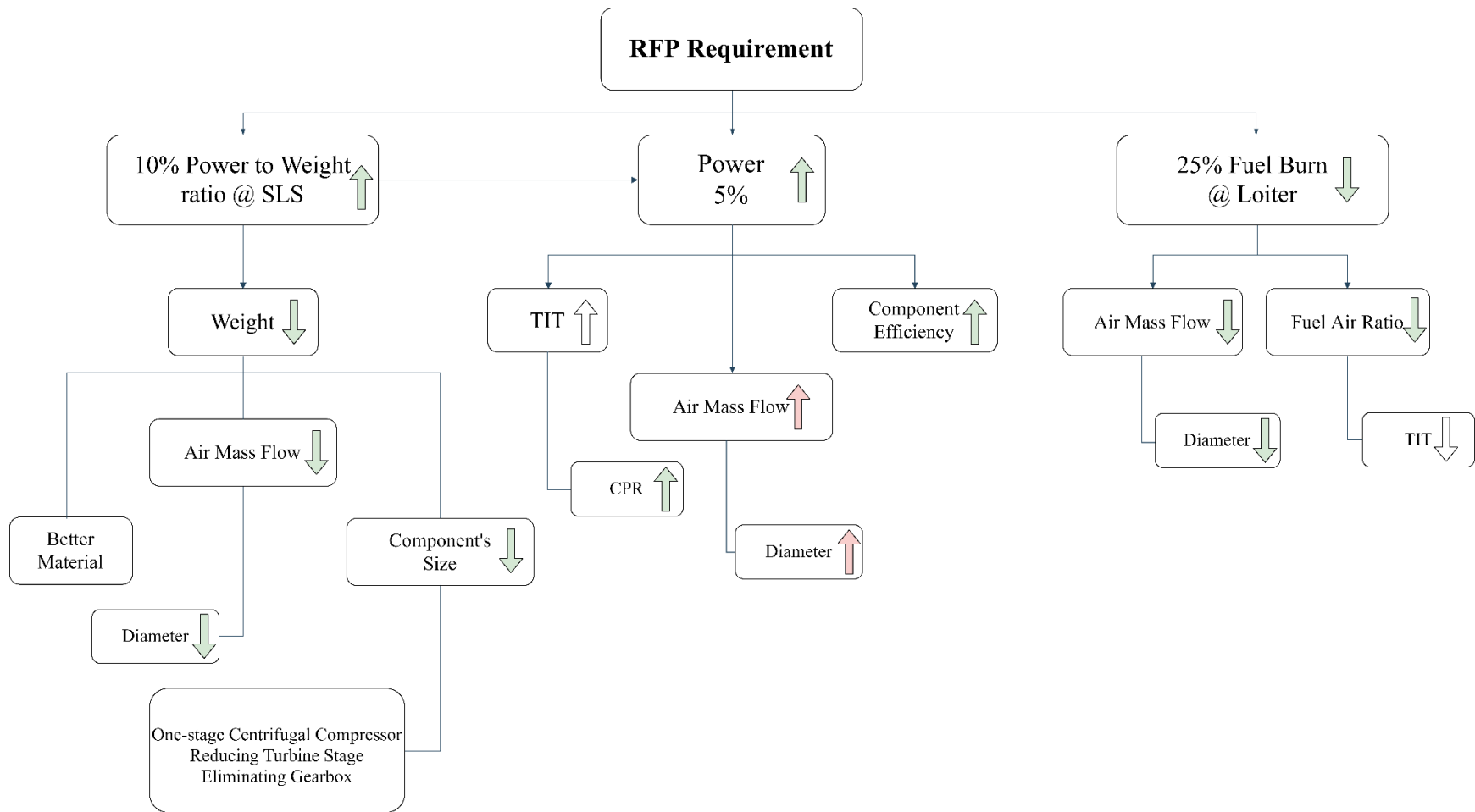


Figure 2.3: Selection Methodology for the Design Point

## 2.2 Engine Type Selection

According to the RFP requirements, the turboshaft engine is the candidate engine type. It is considered that the output shaft power of the gas generator will feed the electric generator, and with the aid of this output power, the electric motors will provide the required thrust. Further, the turboshaft engine is more convenient to extract shaft horsepower than the other types.

## 2.3 Engine Configuration

The RFP has announced TPE331-10 as the baseline engine. As a starting point, turboshaft engines similar to the baseline engine are studied. Then, the most promising engines to the baseline are identified and their technical information is studied, these information are presented in Table 2.1.

Referring to the RFP, the target engine should feed the generators in order to provide the required power to the electric motors. The required power is supplied by the power turbine with a rotational speed different than the compressor turbine shaft speed. Hence, the candidate engine is a twin-spool. Furthermore, a cold end drive configuration is considered due to the high sensitivity of the generator to the temperature.

Table 2.1: Baseline Similar Engines Information

Engine	Manufacturer	Cycle		Performance		Weight and Dimension			Turbomachinery		Burner
		OPR	TIT [°R]	Power [hp]	SFC [lb/hp.hr]	Weight[lb]	Diameter [in]	Length [in]	Compressor	Turbine	Type
TPE331-10	Honeywell	10.55	2579	940	0.543	385	27	43	2C	3HP	Reverse Annular
CTS800-2	LHTEC	14.1	2304	1360	0.448	330	26.8	31.5	2C	2HP	Annular
MTR390-2C	MTU Turbomeca Rolls-Royce	13		1284	0.460	372	26.8	42.2	2C	1HP+2LP	Reverse Annular
T76-G-10	Garret	8.6		1040	0.600	341	27	43	2C	3HP	Reverse Annular
PW207-E	Pratt Whitney Canada	8	2111	650	0.540	250	21.3	36.7	1C	1HP+1LP	Reverse Annular
PW210S	Pratt Whitney Canada		2302	1000	0.542	358	19.7	43	1A+1C	1HP+2LT	Reverse Annular
Arriel2C2	Turbomeca	9.3		944	0.618	265	22.7	39.9	1A+1C	2HP+1LP	Annular
Arrius	Turbomeca	9		750	0.641	253	26.4	38.1	1C	1HP+1LP	Reverse Annular
LTS 101-750B-1	Avco Lycoming	8.4		727	0.577	271	25.4	31.3	1A+1C	1HP+1LP	
250-C40B	Allison	9.2		715	0.570	280	25.1	41	1C	2HP+2LP	

Green color: Baseline engine

“C” and “A” stand for “Centrifugal” and “Axial” respectively

## 2.4 TPE331-10 Cycle Validation

The RFP requests a cycle analysis of the baseline engine TPE331-10. In order to validate the software and the engine model, the baseline engine is modeled in GSP11. As the first step, the cycle of TPE331-10 is validated with RFP's data in the cycle information part. Next, general components maps were scaled to match the components operating points in order to analyze the engine's cycle at off-design conditions.

### 2.4.1 On-Design Validation

To pursue this part, a turboshaft engine was modeled in GSP11 by importing necessary information of each component. It was tried to match the outputs with RFP information which was modeled in NPSS [1]. So, the

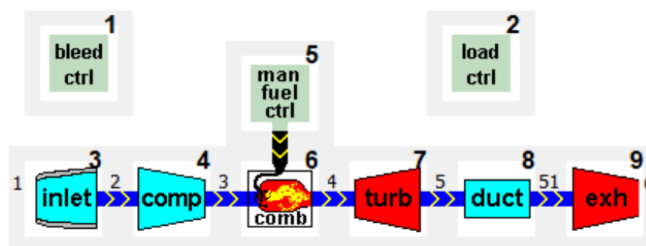


Figure 2.4: Baseline Engine Architecture in GSP11

baseline engine was modeled with high accuracy (under 3% error), and the results are as follows:

Table 2.2: TPE331-10: Flight & Basic Data at On-Design Condition (Take-off)

Flight & Ambient Condition			
Altitude [ft]	0	$\Delta T$ from ISA	0
Static Pressure [psi]	14.6	Mach	0
Static Temperature [ $^{\circ}$ R]	518.6	Velocity [ft/s]	0
Engine Performance Information			
Output Power [hp]	953.1	Fuel Flow [lb/s]	0.1515
PSFC [lb/hp.hr]	0.572	TIT [ $^{\circ}$ R]	2416.4
Mass Flow [lb/s]	7.7	CPR	10.55

Table 2.3: TPE331-10: On-Design Cycle Summary

Station	W [lb/s]	$T_t$ [ $^{\circ}$ R]	$T_s$ [ $^{\circ}$ R]	$P_t$ [psi]	$P_s$ [psi]	Mach
1	7.70	518.6	518.6	14.6	14.6	0
2	7.70	518.6	493.9	14.6	12.3	0.5
3	7.20	1112.1	1079.7	155.0	139.1	0.4
4	7.35	2416.4	2412.7	144.2	143.2	0.1
5	7.85	1538.1	1515.2	16.4	15.5	0.3
51	7.85	1538.1	1515.2	16.3	15.4	0.3
6	7.85	1538.1	1497.1	16.3	14.6	0.4

**Table 2.4: TPE331-10: Component's Information**

<b>Baseline Engine Components Information</b>			
Intake Total Pressure Ratio	1	Burner Fuel LHV [BTU/lb]	18500
Compressor Isentropic Efficiency [%]	82.15	Turbine Isentropic Efficiency [%]	85.5
Compressor Power [hp]	1555.7	Turbine Power [hp]	2509.05
Burner Total Pressure Ratio	0.93	Turbine Exit Duct Total Pressure Ratio	0.995
Burner Isentropic Efficiency [%]	97.5	Nozzle Pressure Ratio	1.12
HGG Rotor Speed [RPM]	41730	Gross Thrust [lb]	185.33

It can be seen by inspection that the obtained results are in good agreement with those from the RFP. In the following, a summary of obtained data at off-design conditions (loiter and cruise) are shown.

## 2.4.2 Off-Design Analysis

Using flight condition and adding compressor and turbine maps, the following results are obtained:

- **Cruise**

**Table 2.5: TPE331-10: Flight & Basic Data at Cruise**

<b>Flight &amp; Ambient Condition</b>			
Altitude [ft]	12500	$\Delta T$ from ISA	0
Static Pressure [psi]	9.1	Mach	0.3478
Static Temperature [ $^{\circ}$ R]	474.1	Velocity [ft/s]	371.3
<b>Engine Performance Information</b>			
Output Power [hp]	690	Fuel Flow [lb/s]	0.1077
PSFC [lb/hp.hr]	0.562	TIT [ $^{\circ}$ R]	2344.2
Mass Flow [lb/s]	5.87	CPR	11.6

- **Loiter**

**Table 2.6: TPE331-10: Flight & Basic Data at Loiter**

<b>Flight &amp; Ambient Condition</b>			
Altitude [ft]	7000	$\Delta T$ from ISA	0
Static Pressure [psi]	11.3	Mach	0.294
Static Temperature [ $^{\circ}$ R]	493.7	Velocity [ft/s]	320.3
<b>Engine Performance Information</b>			
Output Power [hp]	603	Fuel Flow [lb/s]	0.097
PSFC [lb/hp.hr]	0.58	TIT [ $^{\circ}$ R]	2247.1
Mass Flow [lb/s]	5.4258	CPR	8.61

## 2.5 Design Point Selection

A correct selection of the design point is of high importance in this journey. Since the engine spends most of its flight time at loiter, it should have the best performance at this point. Thus, loiter phase is chosen as the design point. This is also beneficial from the cost point of view because of better efficiency and performance. This selection should satisfy the limitations at off-design conditions as well.

## 2.6 Method of Approach

In section 2.1 solutions to the RFP requirements were stated. Now, according to the design philosophy, the design logic should be elaborated. The candidate engine should be designed for a UAV with long endurance, and one of the RFP requirements is a diminution of fuel consumption at loiter. Hence, using a developed code in the MATLAB® environment, PSFC variation as a function of CPR is plotted, Figure 2.5. Further, in this figure, power variation vs. CPR is shown as well. The selected values for the design parameters are given in Table 2.7.

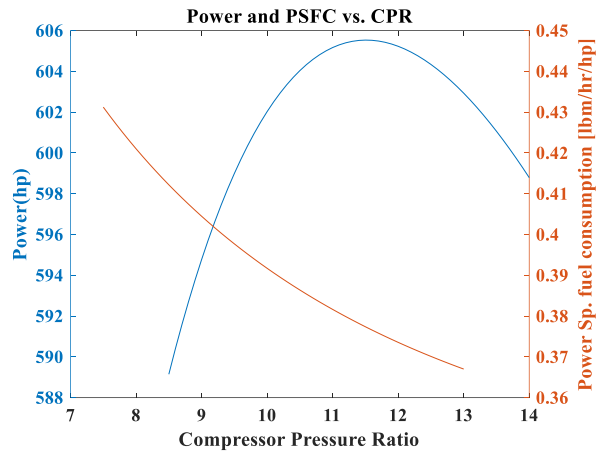


Figure 2.5: Power and PSFC Variation vs. CPR

Table 2.7: Target Engine Component Efficiency and Pressure Losses

Parameter	$\pi_{\text{Inlet}}$	$e_{\text{Comp}}$	$\pi_b$	$\eta_b$	$e_{\text{HPT}}$	$e_{\text{PT}}$	$\eta_{\text{Mech}_{HP}}$	$\eta_{\text{Mech}_{LP}}$	$PR_{\text{nozzle}}$
<b>Design Value</b>	0.99	0.91	0.95	0.995	0.92	0.92	0.995	0.99	1.07

According to Figure 2.5, it can be concluded that specific fuel consumption decreases with increasing CPR which is desirable. Furthermore, the power variation trend is in a way that it maximizes at a specific point but is not necessarily the cycle optimum point. The PSFC vs. TIT diagram with constant CPR lines is shown in Figure 2.6.

Regarding the engine performance at off-design, some phases of flight require a CPR of about 12, and for the design point which is loiter, CPR of 10.2 can be a reasonable value. It should be emphasized that a single stage, state-of-the-art radial compressor can provide a CPR near 13. Also, the new PSFC should be 75% of TPE's PSFC (considering same power). According to the simulation of baseline engine in GSP11, TPE's PSFC is 0.58[lb/hp.hr] at loiter, so PSFC of the candidate engine should be less than 0.435[lb/hp.hr]. Moreover, a point below the maximum point should be selected in the Power vs. CPR diagram, to avoid PSFC rise and observe CPR limitation in respect to technology trend.

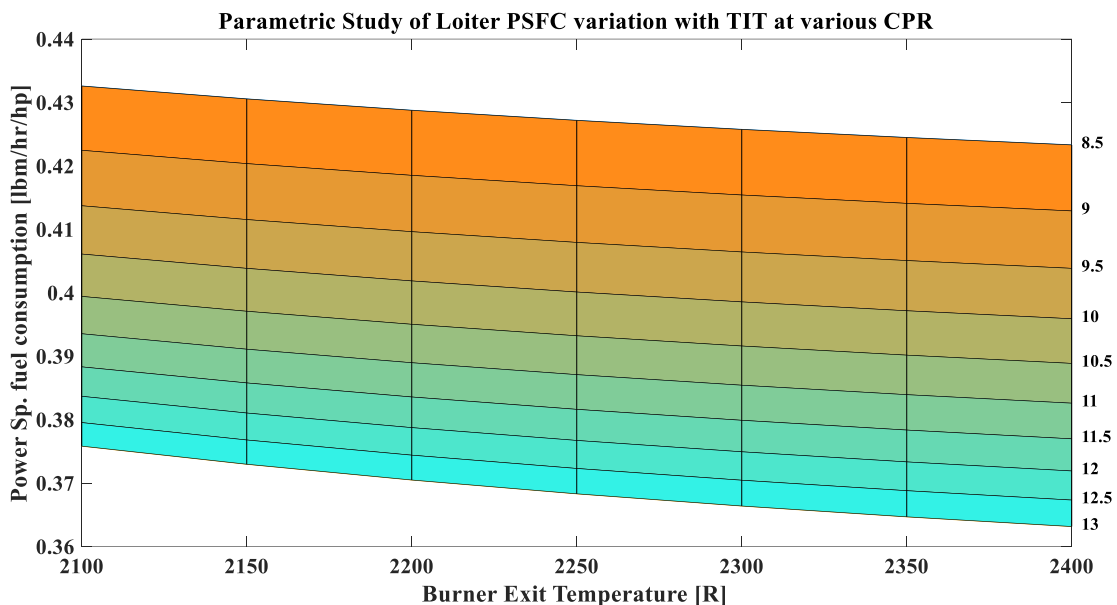


Figure 2.6: Carpet Plot of PSFC vs. TIT on CPR Constant Lines

### 2.6.1 Design Area

To determine the allowable design area, it is crucial to check constraints at the beginning. As stated in section 2.5, design point of the candidate engine is at loiter phase. Hence, the design area should satisfy TIT and CPR for both loiter and take-off conditions. It should be considered that TIT and CPR at take-off are higher than at loiter and as a result, the optimum and efficient design area should be feasible regarding the technology. Consequently, Figure 2.7 proposes the colored area as the design area.



Figure 2.7: Allowable Design Area at Loiter

In Figure 2.7, the output power is plotted as a function of TIT. Vertical blue lines suggest the optimum compressor pressure ratio for each TIT. Also, the green lines represent constant  $\dot{m}_a$  and the red lines show constant  $\dot{m}_f$ . In the colored area, all RFP requirements are met.

In this figure, the highest green line corresponds to TPE’s inlet mass flow rate and the other lines are related to lower flow rates. Also, it is stated in the RFP that the candidate engine fuel consumption at loiter should be 75% of the baseline. Based on GSP11 simulation and considering 25% saving, this amount should be 0.0747 [lb/s] utmost. Hence, the highest red line in the figure is for this limitation of RFP and other lines represent additional reduction in fuel consumption at loiter. Further, CPR constraints should be considered regarding the technology trends. The final restriction that should be taken into account is the required cycle power which is equal to 603 [hp]. In the colored area, the lowest horizontal line is related to this power.

In Figure 2.8 the numerical values of the allowable design area are summarized. It can be observed that by moving from point 1 to 2 on constant CPR line, power increases but this power increment will result in fuel consumption and mass flow increment as well, and consequently, inlet mass flow rate and diameter will increase which is not desirable. By moving from point 2 to 3 on constant  $\dot{m}_f$  line, power increases which is accompanied by TIT increase that causes CPR increment. Also, moving in this direction decreases the inlet mass flow rate. Moving from point 3 to 4 has opposite effect compared to moving from point 1 to 2.

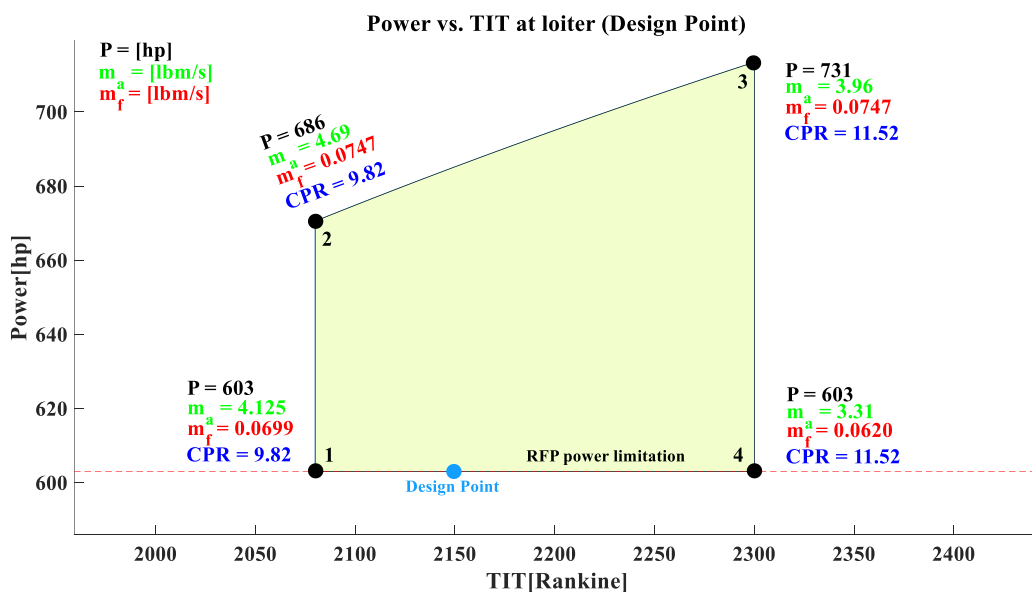


Figure 2.8: Allowable Design Area at Loiter with Specified Values in Boundary Conditions

Furthermore, by traveling from point 1 to 4 on a constant power line, while TIT and CPR increase,  $\dot{m}_f$  and  $\dot{m}_a$  decrease. Finally, to determine the optimum design point, the condition with least fuel consumption and mass flow rate is selected. The conditions of the design point are shown in Table 2.8. The candidate engine will be referred to Sharif TurboShaft 1000 “STS-1000”.

**Table 2.8: Design Point Specifications**

Parameter	Power [hp]	TIT [°R]	CPR	$\dot{m}_a$ [lb/s]	$\dot{m}_f$ [lb/s]	PSFC [lb/hp.hr]
Value	603	2150	10.2	3.953	0.0674	0.402

## 2.7 STS-1000 Final Cycle Design and Analysis

After analysis and validation of TPE331-10 cycle, in order to meet the RFP requirements, the STS-1000 cycle design point is finalized.

One important issue is to use turbine

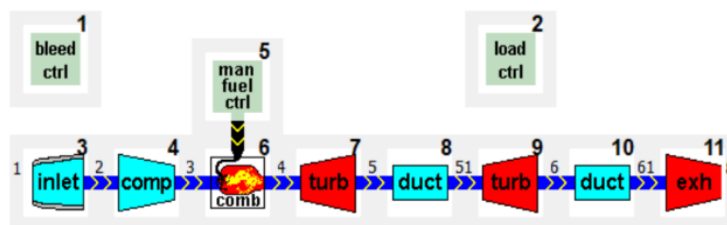


**Figure 2.9: Target Engine Architecture in GSP11**

blade cooling or not. In general, the cooling system in any gas turbine engine will decrease the blade life and the complexity of manufacturing. Hence, choosing a material which eliminates the necessity of cooling is of importance. According to cycle analysis, the maximum turbine inlet temperature occurs at the take-off and is 2535.6 [°R]. CMC with temperature threshold of 3200 [°R] can be selected as an appropriate material which satisfies this criterion. As a result, an uncooled configuration of STS-1000 is selected. Considering engines that are manufactured by GE [5], a TRL of 8 is estimated.

Although the RFP has not required power offtake, an amount of 30 [hp] power offtake is considered for accessories of the engine. It should be pointed out that the engine’s performance would be obviously better without the power offtake. Table 2.7 is used for the engine components efficiency and total pressure losses to model STS-1000 in GSP11. It should be noted that the components Mach number and static conditions are calculated from components preliminary design and matching requirements. Consequently, the following results are for the final STS-1000 cycle.

## 2.7.1 On-Design Analysis

**Table 2.9: STS-1000: Flight & Basic Data at On-Design (Loiter)**

Flight & Ambient Condition			
Altitude [ft]	7000	$\Delta T$ from ISA	0
Static Pressure [psi]	11.3	Mach	0.294
Static Temperature [ $^{\circ}$ R]	493.8	Velocity [ft/s]	320.3
Engine Performance Information			
Output Power [hp]	603	Specific Power [hp/lb]	152.54
PSFC [lb/hp.hr]	0.402	CPR	10.2
Mass Flow [lb/s]	3.953	TIT [ $^{\circ}$ R]	2150
Fuel Flow [lb/s]	0.0674	Power offtake [hp]	30
HGG Rotor Speed [RPM]	40000	Thermal Efficiency [%]	34.15
Power Turbine Rotor Speed [RPM]	22000		

**Table 2.10: STS-1000: On-Design Cycle Summary**

Station	W [lb/s]	T <sub>t</sub> [ $^{\circ}$ R]	T <sub>s</sub> [ $^{\circ}$ R]	P <sub>t</sub> [psi]	P <sub>s</sub> [psi]	Mach
1	3.95	502.2	495.3	12.1	11.4	0.26
2	3.95	502.2	482.6	11.9	10.3	0.45
3	3.95	1030.8	1018.7	121.5	116.4	0.25
4	4.02	2150.0	2109.6	115.5	106.6	0.35
5	4.02	1683.8	1642.4	38.6	34.9	0.39
51	4.02	1683.8	1642.4	38.6	34.9	0.39
6	4.02	1290.1	1245.5	12.26	10.7	0.45
61	4.02	1290.1	1245.5	12.2	10.7	0.45
8	4.02	1290.1	1267.3	12.1	11.3	0.32

## 2.7.2 Off-Design Cycle Analysis

Using general scaled maps for centrifugal compressor and axial turbine, the final results are as follows:

- **Cruise**

**Table 2.11: STS-1000: Flight & Basic Data at Cruise**

Flight & Ambient Condition			
Altitude [ft]	12500	$\Delta T$ from ISA	0
Static Pressure [psi]	91.6	Mach	0.34
Static Temperature [ $^{\circ}$ R]	474.1	Velocity [ft/s]	371.3
Engine Performance Information			
Output Power [hp]	690	Specific Power [hp/lb]	184.24
PSFC [lb/hp.hr]	0.40	Thermal Efficiency [%]	34.3
Mass Flow [lb/s]	3.745	CPR	12.3
Fuel Flow [lb/s]	0.0768	TIT [ $^{\circ}$ R]	2385.2
HGG Rotor Speed [RPM]	42260		

- **Hot take-off**

**Table 2.12: STS-1000: Flight & Basic Data at Hot Take-off**

Flight & Ambient Condition			
Altitude [ft]	0	$\Delta T$ from ISA	27
Static Pressure [psi]	14.6	Mach	0
Static Temperature [ $^{\circ}R$ ]	545.6	Velocity [ft/s]	0
Engine Performance Information			
Output Power [hp]	953	Specific Power [hp/lb]	185.4
PSFC [lb/hp.hr]	0.4179	Thermal Efficiency [%]	32.8
Mass Flow [lb/s]	5.14	CPR	11.9
Fuel Flow [lb/s]	0.11053	TIT [ $^{\circ}R$ ]	2535.6
HGG Rotor Speed [RPM]	44210		

- **Normal take-off**

**Table 2.13: STS-1000: Flight & Basic Data at Normal Take-off**

Flight & Ambient Condition			
Altitude [ft]	0	$\Delta T$ from ISA	0
Static Pressure [psi]	14.6	Mach	0
Static Temperature [ $^{\circ}R$ ]	518.6	Velocity [ft/s]	0
Engine Performance Information			
Output Power [hp]	1050	Specific Power [hp/lb]	190.9
PSFC [lb/hp.hr]	0.4123	Thermal Efficiency [%]	33.2
Mass Flow [lb/s]	5.5	CPR	12.6
Fuel Flow [lb/s]	0.12	TIT [ $^{\circ}R$ ]	2535.6
HGG Rotor Speed [RPM]	44600		

## 2.8 UAV Performance Analysis

Considering the RFP requirements which are +1000 [nm] range and +20 [hr] loiter, the expected target UAV mission profile is presented in Figure 2.10. Recalling the cruise speed and the covered distance, it spends 4 [hr] and 33 [min], the target UAV descends

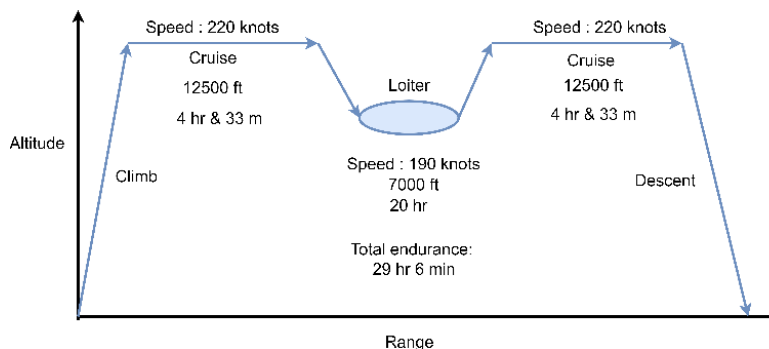


**Figure 2.10: UAV Mission Profile**

to 7000 [ft] and loiters for at least 20 [hr] at this altitude with the speed of 190 [knots]. Finally, it climbs to 12500 [ft]

and cruises 1000 [nm] with the speed of 220 [knots]. The target UAV is not clearly mentioned in the RFP, but its geometrical and performance characteristics are mentioned. More investigation reveals that General Atomics MQ-9 Reaper (Predator B) UAV uses TPE331-10 and its characteristics are analogous to the RFP's UAV. The performance and geometrical characteristics of MQ-9 and target UAV are compared in Table 2.14.

**Table 2.14: Comparison of General Characteristics Between Target UAV and MQ-9**

UAV Parameter	Length [ft]	Wing Span [ft]	Height [ft]	MTOW [lb]	Service ceiling [ft]	Fuel Tank [gal]
RFP UAV	36	65.5	12.5	10500	50000	602
MQ-9 Predator B	36.1	65.7	12.6	10494	50000	602

MQ-9 is a UAV of a class of MALE which is developed by General Atomic. The aircraft possesses a turboprop engine TPE331-10 with an output power of approximately 900 [hp]. The endurance of MQ-9 is 27 [hr] [6] with an assumed speed of 200 knots and a range of 1000 [nm]. Thus, for this mission 10 [hr] of endurance is devoted for cruise to mission point and return to the military base. Consequently, this drone may loiter for 17 [hr] at the mission point.

It is worth mentioning that accurate calculation of range and endurance of a hybrid UAV requires the knowledge of the aircraft geometry, drag polar equation, characteristics, and positioning of electric motors and batteries. Since the RFP does not provide these information, simple approximations are used.

Since STS-1000 consumes 30.5 % less fuel than TPE331-10 at loiter and 28.7% at cruise, and also the similarity of target UAV characteristics to MQ-9, one may conclude that the target UAV with STS-1000 engine could fly farther 1000 [nm], loiter for 20 [hr], and fly back to the base of 1000 [nm] successfully.

## 2.9 Overall Performance Comparison

After analyzing STS-1000 and TPE331-10 cycle in different flight phases, Table 2.15 shows the overall engine performance improvement of STS-1000 in comparison to TPE331-10.

**Table 2.15: Performance Comparison of STS-1000 to TPE331-10**

	TPE331-10	STS-1000	RFP Requirement %	Difference %
<b>SLS Power Output [hp]</b>	953	1050	+5	+10.1☑
<b>Fuel flow @ Loiter [lb/s]</b>	0.097	0.0674	-25	-30.5☑
<b>Fuel flow @ Cruise [lb/s]</b>	0.1077	0.0768		-28.7☑
<b>Dry Weight [lb]</b>	385	253.42	-4.5	-35☑
<b>Power to Weight Ratio</b>	2.47	4.14	+10	+67☑

## Chapter 3 Centrifugal Compressor Design

This chapter presents the method for designing a centrifugal compressor based on the cycle design requirements from previous chapter. In order to satisfy the cycle requirements at both on-design and off-design conditions, the compressor should be able to provide the pressure ratio of 10.2:1 at loiter and 12.6:1 ratio at normal take-off. According to off-design studies and technology trade study, it can be concluded that a state-of-the-art single stage radial compressor with the total pressure ratio of about 13 and total polytropic efficiency around 91% can be designed for the mass flow range of the target engine design area. Some examples of already commercial or tested high-pressure single stage centrifugal compressors are Arrius (8:1) [8], NASA (8:1) [10], and US Army Air Mobility Research (10:1) [9].

### 3.1 Components Overview

The schematic view of a centrifugal compressor with station numbering is illustrated in Figure 3.1.

#### IGV

Recalling the cycle design calculations, it is determined that the engine CPR corresponding to the design point varies up to 25%. This variation is relatively high and can cause stall and surge. Further, since the compressor pressure ratio is high, it is highly possible that it works in the transonic regime. Therefore, impeller inlet tip relative Mach number would be higher than one. This transonic region increases losses and makes shock waves which are detrimental for the performance of the compressor and consequently attenuate compressor surge margin. A possible solution, which different references have proposed it, will be by using IGV. In this case, a positive angle (positive pre-whirl) is applied to reduce the impeller inlet tip relative Mach number, increase stability, and eliminate the shock losses. In other words, IGV acts as a controller. Figure 3.2 shows

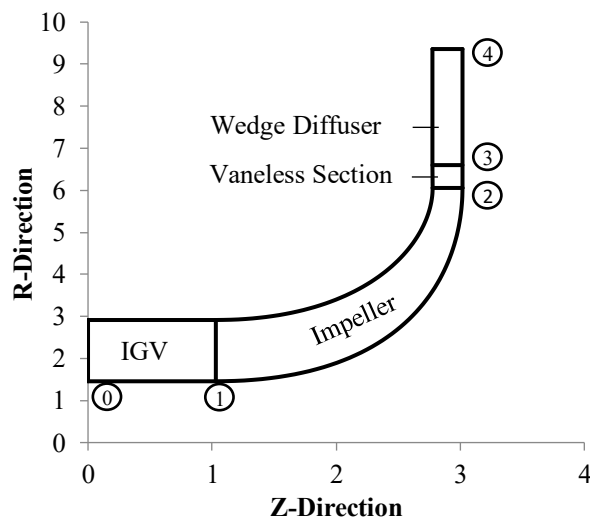


Figure 3.1: Compressor Schematic Illustration and Station Numbering

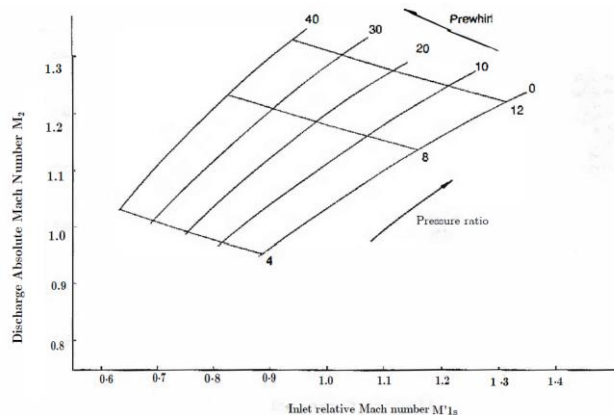


Figure 3.2: Effect of Prewhirl on Impeller Inlet and Discharge Mach Numbers [7]

the effect of positive pre-whirl on impeller inlet relative Mach number and exit absolute Mach number [7]. The relative Mach number at the tip ( $M_{rel_{tip}}$ ) can be between 0.8 and 0.9 at the maximum level based on [4]. To be on the safe side, in this report, the Mach number is considered as 0.8.

It is worth mentioning that NACA 6-series airfoil is used as IGV's blade profile.

## Impeller and Splitter

For determining number and type of the blades, it would be:

**Blade Numbers:** According to slip factor definition by Stantiz [11].

$$\mu = 1 - \frac{0.63\pi}{Z_I} \quad (3.1)$$

Where  $Z_I$  is the impeller blade number. Slip Factor, in fact, is the deviation of actual tangential velocity from the ideal condition. This deviation would result in swirl velocity reduction which causes pressure ratio decrease and enthalpy rise. Considering Eq. (3.1), by increasing the blade numbers of the impeller, the slip factor would converge to one. However, it should be considered that a high number of blades leads to increase in stress level, weight, and cost. Furthermore, the typical value of the slip factor lies in the range of 0.85 and 0.9. Hence, an iteration is performed and finally the value of 0.9 is selected. Based on suggestions in various references for reducing the impact of slip factor and increasing the pressure ratio, using splitter is customary for each impeller. The optimum length of splitter for best efficiency is half of the main blade, based on Nagpuwala [11].

**Blade Type:** Generally, three types of blades are suitable for impeller which are mentioned in Table 3.1.

**Table 3.1: Impeller Type Comparison**

	Stability	Operating Range	Efficiency	Size	Manufacturing	Pressure Rise with Same RPM
<b>Forward Swept</b>				Better☑		Better☑
<b>Radial Swept</b>					Better☑	
<b>Backward Swept</b>	Better☑	Better☑	Better☑			

According to the RFP, the target UAV is a long endurance aircraft, so stability is the highest priority for the engine compressor. As a result, the backward swept type is chosen. Based on Whitfield [7], increasing the negative swept angle has two effects. First, it reduces the impeller exit Mach number which is desirable, and second, increases the tip relative Mach number which is undesirable but can be controlled by IGV. So, according to the above reasons and Table 3.1, a swept angle of  $-40^\circ$  is chosen for the impeller.

## Diffuser

Diffusers in centrifugal compressors consist of two parts: vaneless and vaned sections. Although the vaneless section reduces the efficiency, it helps the compressor stability because it reduces impeller exit Mach number. Additionally, this region rises the static pressure. The vaned section can also have different types (wedge, airfoil, blade with same thickness). The wedge type is better than airfoil in terms of manufacturing cost and simple structure. So, wedge type is selected.

## Collector

Since the combustor type is reverse flow, one collector is required to accumulate outlet radial flow and guide it through a duct to the combustor.

## 3.2 Characteristics

This section describes overall compressor characteristics.

### 3.2.1 General Design Parameters

Design and geometry requirements are shown in Table 3.2. Also, Table 3.3 is used for choosing the best value of important geometry and aerothermodynamics parameters. These ranges are from Aungier [12] and Whitfield [7]. In centrifugal compressor design, some losses such as inlet duct, skin friction, blade loading, clearance, disk friction, and impeller total loss can affect the compressor performance. In the design procedure, these losses are also considered.

**Table 3.2: Design Parameters**

Parameters	Value	Parameters	Value
Compressor Inlet $T_t$ [R]	502.24	$\pi_c$	10.2
Compressor Inlet $P_t$ [Psi]	11.92	$\tau_c$	2.07
Compressor Exit $T_t$ [R]	1030.84	$\omega$ [RPM]	40000
Compressor Exit $P_t$ [Psi]	121.58	$\eta$ %	88
Compressor Power [hp]	720	$e$ %	91

**Table 3.3: Design Constraints and Guidelines**

Parameters	Design Value	Typical Values or Limitations
Compressor Inlet Mach Number	0.45	$0.4 \leq M \leq 0.55$
Stage Total Pressure Ratio	10.2	Up to 13:1
Rotational Speed [RPM]	40000	Limited by Mach, dimension, and mass flow
$e$ %	91	Up to 91
$\mu$	0.9	$0.85 \leq \mu \leq 0.9$
$Z_{\text{Splitter}}$	20	Same as $Z_{\text{Impeller}}$
Impeller hub to tip Ratio	0.5	$0.4 \leq H/T \leq 0.6$
Inducer Shroud to Tip Radius Ratio	0.5	$0.5 \leq r_1/r_2 \leq 0.7$
Impeller Swept Angle	-40	$-40 \leq \beta'_2 < 0$
Blade Loading	0.838	$BL \leq 0.9$
Diffusion Factor	1.51	$DF \leq 2$
Diffusion Ratio	1.47	$DF \leq 1.7$
Diffuser Pressure Recovery Coefficient	0.78	$C_p \leq 0.85$
Vaneless Radius Ratio ( $r_3/r_2$ )	1.125	$1.05 \leq r_3/r_2 \leq 1.125$
Wedge Diffuser Radius Ratio ( $r_4/r_3$ )	1.4	$1.3 \leq r_4/r_3 \leq 1.6$
Diffuser Area Ratio	2.41	$2.2 \leq AR \leq 3.3$
$Z_D$	29	$ Z_D - Z_I  \geq 8$
Total Divergence Angle	8	$2\theta \leq 11$
Diffuser Blade Angle	16	$16 \leq \beta_3 \leq 23$
IGV Blade Number	20	Same as $Z_{\text{Impeller}}$
Diffuser Passage Width [in]	0.2556	Same as Impeller Axial Width

### 3.2.2 Geometry and Aerothermodynamics Calculations

A MATLAB® Code is developed for calculating all parameters in the compressor.

#### Shaft RPM

Shaft rotational speed is limited by the mass flow, compressor inlet Mach number, and dimension. Increasing shaft speed results in the increment of the compressor inlet Mach number and it can reduce the compressor inlet diameter. Thus, based on these reasons, cycle mass flow at the design point, and compressor inlet Mach number, a shaft rotational speed of 40000 [RPM] is selected.

#### Impeller

Using cycle information and intake design, compressor inlet total and static thermodynamics properties, mass flow, inlet area, and axial Mach number are given in GSP11 [2]. This information is presented in Table 3.4.

**Table 3.4: Compressor Inlet Flow Parameters**

Parameter	Mass Flow [lb/s]	$A_1$ [in <sup>2</sup> ]	Mach number	$P_{t1}$ [psi]	$T_{t1}$ [°R]	$P_{s1}$ [psi]	$T_{s1}$ [°R]	$\rho_{s1}$ [slug/ft <sup>3</sup> ]
<b>Value</b>	10.2	20.24	0.45	11.92	502.2	10.37	482.6	0.0018

Using the continuity equation and Table 3.4 the compressor inlet axial velocity ( $C_{ax1}$ ) is calculated as 484.65 [ft/s].

For calculating impeller inlet tip radius, the hub to tip ratio is chosen as 0.5. Eq. (3.2) is used to calculate  $r_{tip1}$  and turns out to be 2.931 [in].

$$r_{tip1} = \sqrt{\frac{A_1}{\pi \left( 1 - \left( \frac{r_{hub1}}{r_{tip1}} \right)^2 \right)}} \quad (3.2)$$

Table 3.5 shows impeller inlet dimensions.

**Table 3.5: Impeller Inlet Dimensions**

Parameter	Hub Radius [in]	Mid Radius [in]	Tip Radius [in]
Value	1.465	2.198	2.931

According to Eq.(3.3), the pre-whirl angle ( $\theta$ ) is  $32.68^\circ$ .

With having inlet geometry and IGV pre-whirl angle and assuming free vortex design, the inlet absolute and relative velocities are calculated. Detailed information is presented in the velocity triangle section. For calculating impeller exit tip radius, impeller shroud to tip ratio ( $r_{1s}/r_2$ ) is chosen as 0.5. According to Whitfield [7], as the  $r_{1s}/r_2$  decreases, the impeller inlet relative tip Mach number would decrease. Figure 3.3 shows the effect of the shroud to tip radius ratio on the inlet tip relative Mach number.

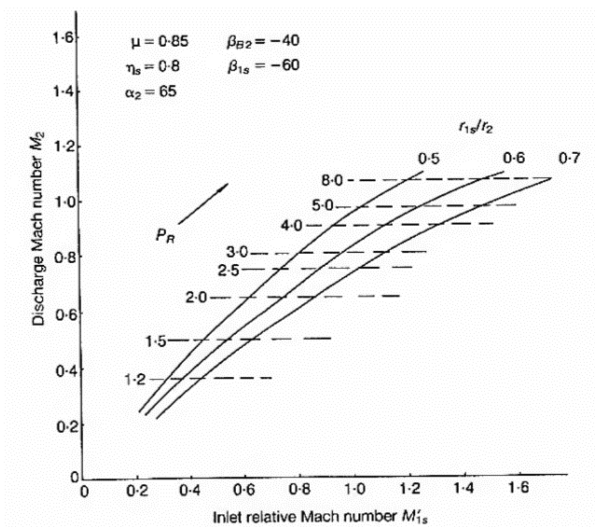


**Figure 3.3: Effect of Reducing Radius Ratio on Inlet Relative Mach Number [7]**

$$M_{1rel\ tip} = \frac{W_1}{a_1} = \sqrt{\frac{Cax_1^2 + \left( U_{1tip} - Cax_1 \tan\theta \right)^2}{\gamma.R.T_1}} \quad (3.3)$$

For calculating the impeller exit axial width and velocities, the impeller exit flow coefficient ( $\varphi_2$ ) should be known.

According to Ahmad El Sayed [4] and Eq.(3.4), the impeller exit flow coefficient is 0.17.

$$\varphi_2 = \left( 1 - \frac{\pi_c^{(\gamma-1)/\gamma} - 1}{(\gamma-1)\eta_c \left( \frac{U_2}{a_{t1}} \right)^2 \cdot \sigma} \right) / \tan(\beta'_2) \quad (3.4)$$

$$C_{r2} = U_2 \cdot \varphi_2 \quad (3.5)$$

At the impeller exit, axial velocity term vanishes, and hence the radial velocity ( $C_{r2}$ ) from Eq. (3.5) is used for the continuity equation. For calculating the impeller exit axial width, it is assumed that losses caused by the diffuser and impeller are equal ( $\xi = 0.5$ ). From Eq.(3.6) the impeller adiabatic efficiency ( $\eta_{\text{impeller}}$ ) calculated to be equal 94%.

$$\eta_{\text{impeller}} = 1 - \xi + \xi \cdot \eta_c \quad (3.6)$$

For the impeller exit static density, Eq.(3.7) to (3.10) are used as:

$$\sigma = \frac{C_{\theta, \text{actual}}}{C_{\theta, \text{ideal}}} = \frac{U_2 - C_{r2} \cdot \tan(\beta_2)}{U_2 - C_{r2} \cdot \tan(\beta_2')} \quad (3.7) \quad T_t = T_s - \frac{C^2}{2 \cdot C_p} \quad (3.8)$$

$$C = \sqrt{C_{ax}^2 + C_{\theta}^2 + C_r^2} \quad (3.9) \quad \frac{P_{t2}}{P_{t1}} = \left( 1 + \eta_{\text{impeller}} \cdot \left( \frac{T_{t2} - T_{t1}}{T_{t1}} \right) \right)^{\gamma/\gamma-1} \quad (3.10)$$

Finally, using the continuity equation and assuming a blockage factor of 0.95, the impeller exit axial width ( $b_2$ ) becomes equal to 0.2560 [in]. According to Aungier [12], from Eq. (3.11) and (3.12) the impeller axial length becomes 1.98 [in] with the stage flow coefficient

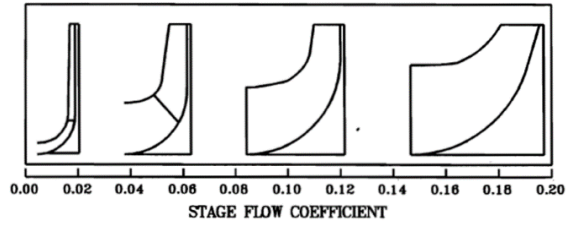


Figure 3.4: Typical Impeller Style [5]

equal to 0.04. Further, according to Figure 3.4, in order to achieve high efficiency and pressure ratio for the impeller, the tip radius to axial length ratio should be high—that is, a low stage flow coefficient.

$$\frac{\Delta Z}{2r_2} = 0.014 + 0.023 \frac{r_2}{r_{1\text{hub}}} + 1.58\varphi \quad (3.11) \quad \varphi = \frac{\dot{m}}{\rho_{t0} \cdot \pi \cdot r_2^2 \cdot U_2} \quad (3.12)$$

Table 3.6 shows the impeller exit dimensions.

Table 3.6: Impeller Exit Dimensions

Parameter	Tip Radius [in]	Axial Width [in]	Axial Length [in]	Mean Camberline Length ( $L_B$ ) [in]
Value	5.86	0.2596	1.98	6.84

For proper impeller aerodynamics, the diffusion factor and the blade loading should be evaluated. According to Aungier[12], for preventing impeller stall, the diffusion factor should be lower than 2 and the blade loading lower than 0.9. Using Eq.(3.13)to (3.18), the diffusion factor and blade loading are determined as 1.51 and 0.83, respectively.

$$Z_{\text{effective}} = Z_{\text{impeller}} + \frac{L_{\text{splitter}}}{L_{\text{impeller}}} \cdot Z_{\text{splitter}} \quad (3.13) \quad W_{\text{max}} = \frac{(W_1 + W_2 + \Delta W)}{2} \quad (3.14)$$

$$\Delta W = \frac{4 \cdot \pi \cdot r_2 \cdot U_2 \cdot J_B}{Z_{\text{effective}} \cdot L_B} \quad (3.15) \quad DF = \frac{W_{\text{max}}}{W_2} \quad (3.16)$$

$$I_B = \frac{C_{\theta 2}}{U_2} - \frac{U_1 C_{\theta 1}}{U_2^2} \quad (3.17)$$

$$BL = \frac{2\Delta W}{W_1 + W_2} \quad (3.18)$$

In addition, using inlet and exit flow properties Eq. (3.19) and (3.20), the degree of reaction and the diffusion ratio are calculated 0.64 and 1.47, respectively. According to Aungier [12] if diffusion ratio is greater than 1.7 it would increase the losses and the compressor becomes unstable.

$$DR = \frac{W_{ip1}}{W_2} \quad (3.19)$$

$$\circ R = \frac{h_2 - h_1}{h_{t2} - h_{t1}} \quad (3.20)$$

### 3.2.3 Velocity Triangles (with hand calculations)

#### Impeller Inlet

Using IGV pre-whirl and Eq.(3.21) to (3.24), the remaining parameters are calculated as follows:

$$W_i = \sqrt{(U_i - C_{\theta i})^2 + C_a^2} \quad (3.21)$$

$$C_{\theta i} = C_a \cdot \tan(\theta) \quad (3.22)$$

$$C_i = \frac{C_a}{\cos(\theta)} \quad (3.23)$$

$$\beta_i = \cos^{-1}\left(\frac{C_a}{W_i}\right) \quad (3.24)$$

Where “i” is any impeller inlet radial location like hub, mid and tip. The velocities and angles are summarized in Table 3.7. Further, the impeller inlet velocity triangles are shown in Figure 3.5.

**Table 3.7: Impeller Inlet Velocities and Angles at Hub, Mid and Tip**

Parameters	C [ft/s]	C <sub>ax</sub> [ft/s]	C <sub>0</sub> [ft/s]	U [ft/s]	W [ft/s]	β [deg]	α [deg]
<b>Hub</b>	575.80	484.65	310.9	511.64	524.58	22.49	32.68
<b>Mid</b>	575.80	484.65	310.9	767.46	665.83	43.29	32.68
<b>Tip</b>	575.80	484.65	310.9	1023.3	861.6	55.77	32.68

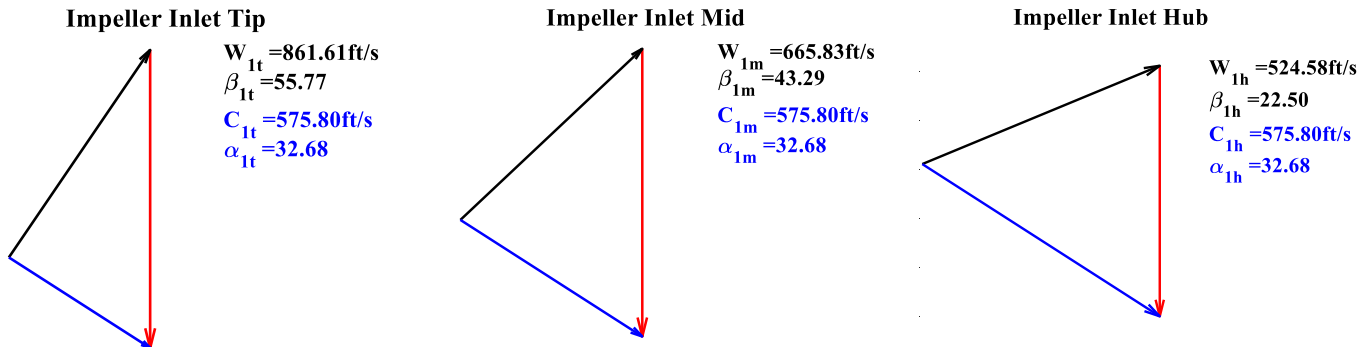


**Figure 3.5: Impeller Inlet Velocity Triangles at Hub, Mid and Tip**

#### Impeller Exit

Using Eq.(3.25) to (3.38), all velocities and angles are calculated as follows:

$$W_2 = \sqrt{(U_2 - C_{\theta 2})^2 + C_{r2}^2} \quad (3.25) \quad \beta_2 = \cos^{-1}\left(\frac{C_{r2}}{W_2}\right) \quad (3.26)$$

$$C_{\theta 2} = C_{r2} \tan(\alpha_2) \quad (3.27) \quad \alpha_2 = \cos^{-1}\left(\frac{C_{r2}}{C_2}\right) \quad (3.28)$$

The results are summarized in Table 3.8. In addition, Figure 3.6 shows the impeller exit velocity triangle.

**Table 3.8: Impeller Exit Velocities and Angles**

Parameter	$C_2$ [ft/s]	$C_{r2}$ [ft/s]	$C_{\theta 2}$ [ft/s]	$U_2$ [ft/s]	$W_2$ [ft/s]	$\alpha_2$ [deg]	$\beta_2$ [deg]
<b>Value</b>	1616	349.95	1577.6	2046.6	585.12	77.49	53.27

### Impeller Exit

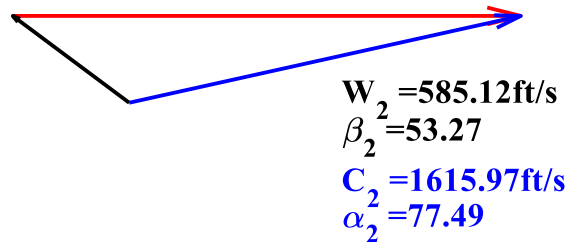


**Figure 3.6: Impeller Exit Velocity Triangle**

## Diffuser

### Vaneless Section

Considering the momentum and mass conservation gives by Eq.(3.29) and (3.30):

$$r \cdot C_{\theta} = \text{Cte} \rightarrow r_3 \cdot C_{\theta 3} = r_2 \cdot C_{\theta 2} \quad (3.29)$$

$$\rho_2 \cdot r_2 \cdot C_{r2} \cdot b_2 = \rho_3 \cdot r_3 \cdot C_{r3} \cdot b_3 \quad (3.30)$$

And assuming that the total pressure and temperature are conserved, it is recommended by Aungier[12] that  $b_2/b_3$  should be less than or equal to one due to avoidance of higher losses caused by flow separation. Considering Table 3.3, the exit radius of the vaneless diffuser becomes 6.6 [in].

### Wedge Diffuser

In this section, all the dimensions of the diffuser are determined. It should be noted that the diffuser should not operate in the stall region. Therefore, the divergence angle

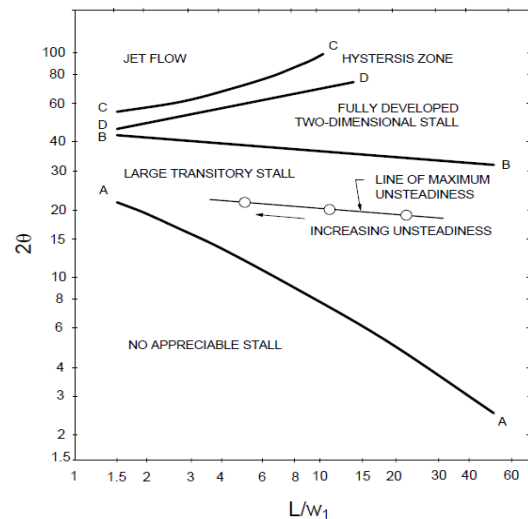


**Figure 3.7: Flow Regime Chart for Wedge [12]**

$(2\theta)$  and the length to width ratio ( $L/W$ ) are selected from Figure 3.7 as  $8^\circ$  for an  $L/W$  equals to 10. Using Table 3.3

and Eq.(3.31) to (3.34), the remaining parameters are calculated. Table 3.9 summarizes the wedge diffuser geometry parameters.

$$W_{throat} = \frac{2 \cdot \pi \cdot r_3 \cdot \sin(\beta_3)}{Z_d} \quad (3.31) \quad \tan \theta = \frac{AR - 1}{2L / W_{th}} \quad (3.32)$$

$$AR = \frac{W_{exit}}{W_{throat}} \quad (3.33) \quad AS = \frac{b_{throat}}{W_{throat}} \quad (3.34)$$

**Table 3.9: Wedge Diffuser Geometry Parameters**

Parameter	AR	AS	L [in]	W <sub>throat</sub> [in]	W <sub>exit</sub> [in]	R <sub>4</sub> [in]	b <sub>4</sub> [in]
Value	2.41	0.6496	3.94	0.393	0.949	9.3	0.2596

Using Eq. (3.35), the compressor exit Mach number is calculated as 0.25 which is suitable for the combustion chamber.

According to Eq. (3.36), the diffuser pressure recovery coefficient becomes 0.78.

$$\frac{A}{A^*} = \frac{1}{M} \times \left( \frac{2}{\gamma + 1} \times \left( 1 + \frac{\gamma - 1}{2} M^2 \right) \right)^{\frac{\gamma + 1}{2(\gamma - 1)}} \quad (3.35) \quad C_P = \frac{P_4 - P_2}{P_{t2} - P_2} \quad (3.36)$$

### 3.2.4 Thermodynamic Properties

Table 3.10 summarizes of all thermodynamics properties across the centrifugal compressor.

**Table 3.10: Compressor Thermodynamics Properties**

	Thermodynamic Properties				
	P <sub>t</sub> [psi]	P <sub>s</sub> [psi]	T <sub>t</sub> [°R]	T <sub>s</sub> [°R]	Mach
<b>Compressor Inlet</b>	11.92	10.37	502.2	482.6	0.45
<b>Impeller Inlet</b>	11.91	9.78	502.2	474.6	0.53
<b>Impeller Exit</b>	132.35	57.78	1030.8	813.5	1.15
<b>Vaneless Diffuser Exit</b>	132.35	70.84	1030.8	862.2	0.98
<b>Compressor Exit</b>	121.58	116.40	1030.8	1018.1	0.25

### 3.2.5 Stress Calculation and Material Selection

According to reference [10], for preliminary stress calculation of centrifugal compressors, two parameters should be taken into account: the disk stress and the blade stress. Eq.(3.37) and (3.38) are used to calculate these stresses.

$$\sigma_{disk} = \frac{3}{4} \rho_{material} U_2^2 \cdot \frac{3 + \nu}{8} \quad (3.37) \quad \sigma_{blade} = \frac{0.5 \cdot b_2^2 \cdot 6 \rho_{material} \cdot r_{tip} \cdot \omega^2 \cdot \sin(\beta_{blade})}{t_{tip}} \quad (3.38)$$

The highest RPM is considered as the critical condition. Based on technology studies [13], for modern aero engines, titanium is used in centrifugal compressors. Further, the maximum compressor temperature is 1183 [°R].

Considering Figure 3.8, Ti-6Al-4V is chosen as the compressor material, and the disk and blade stresses are calculated and shown in Table 3.11.

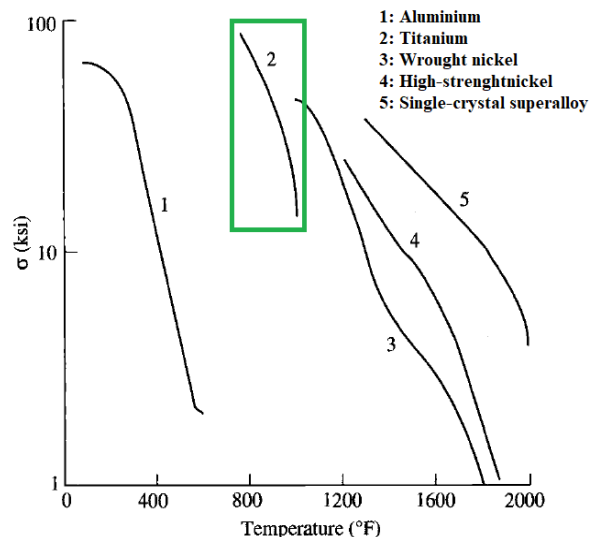


Figure 3.8: Allowable Stress vs. Temperature for Typical Engine Materials [4]

Table 3.11: Disk and Blade Stress

Parameters	$\sigma_{\text{disk}}$ [ksi]	$\sigma_{\text{blade}}$ [ksi]	Disk Safety Factor	Blade Safety Factor
<b>Value</b>	93.83	4.53	1.42	29.36

### 3.3 Geometry Construction

Determining the geometry of the impeller is done by an iterative method, according to Aungier [12]. The purpose of this iteration is the convergence of solutions to the designed impeller numbers. First, the impeller length is determined by Eq. (3.11). Second, for determining the hub contour a circular arc is recommended, Figure 3.9.

Also, shroud contour of the impeller is generated with the aid of a three-point cubic spline curve, Figure 3.9. In this method, the starting and end points are known but the middle point of this spline should be selected and as an initial assumption, the mid-passage point is selected. Designing procedure will continue until the solutions would converge to the design blade numbers.

Parametric calculations for determining hub and shroud contours can be seen in Aungier [12].

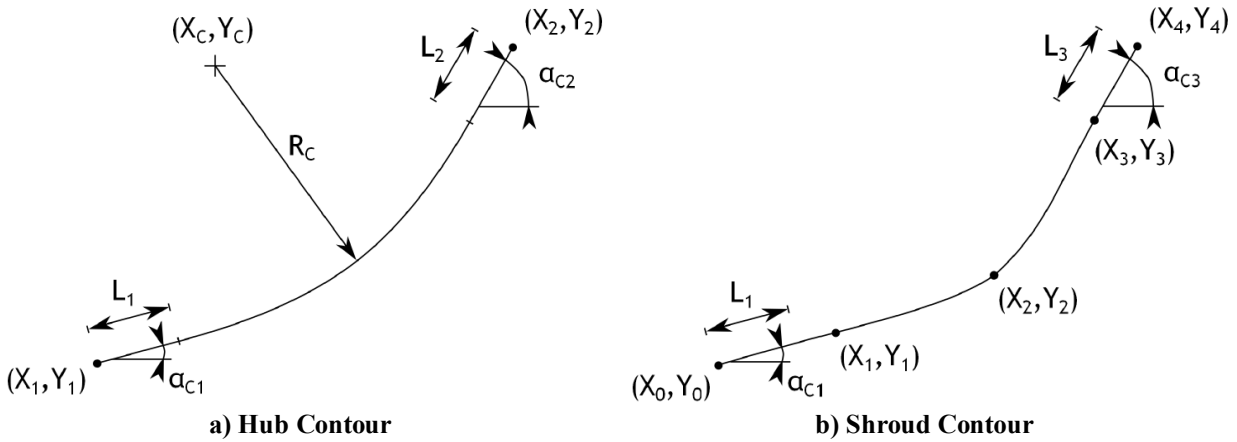


Figure 3.9: Impeller Geometrical Construction Method

### 3.4 Compressor Inflow Data

Table 3.12: Compressor Inflow Data

Flow Station Data at Compressor	
Inflow Mass Flow Rate [lb/s]	3.95
Corrected Inflow Mass Flow Rate[lb/s]	4.79
Inflow Total Pressure [psi]	11.92
Inflow Total Temperature [°R]	502.24
Inflow Fuel-air Ratio	0
Inflow Mach #	0.45
Inflow Area [in <sup>2</sup> ]	20.16
Stage Total Pressure Ratio	10.2

Finally, the compressor design approach can be summarized in Figure 3.10.

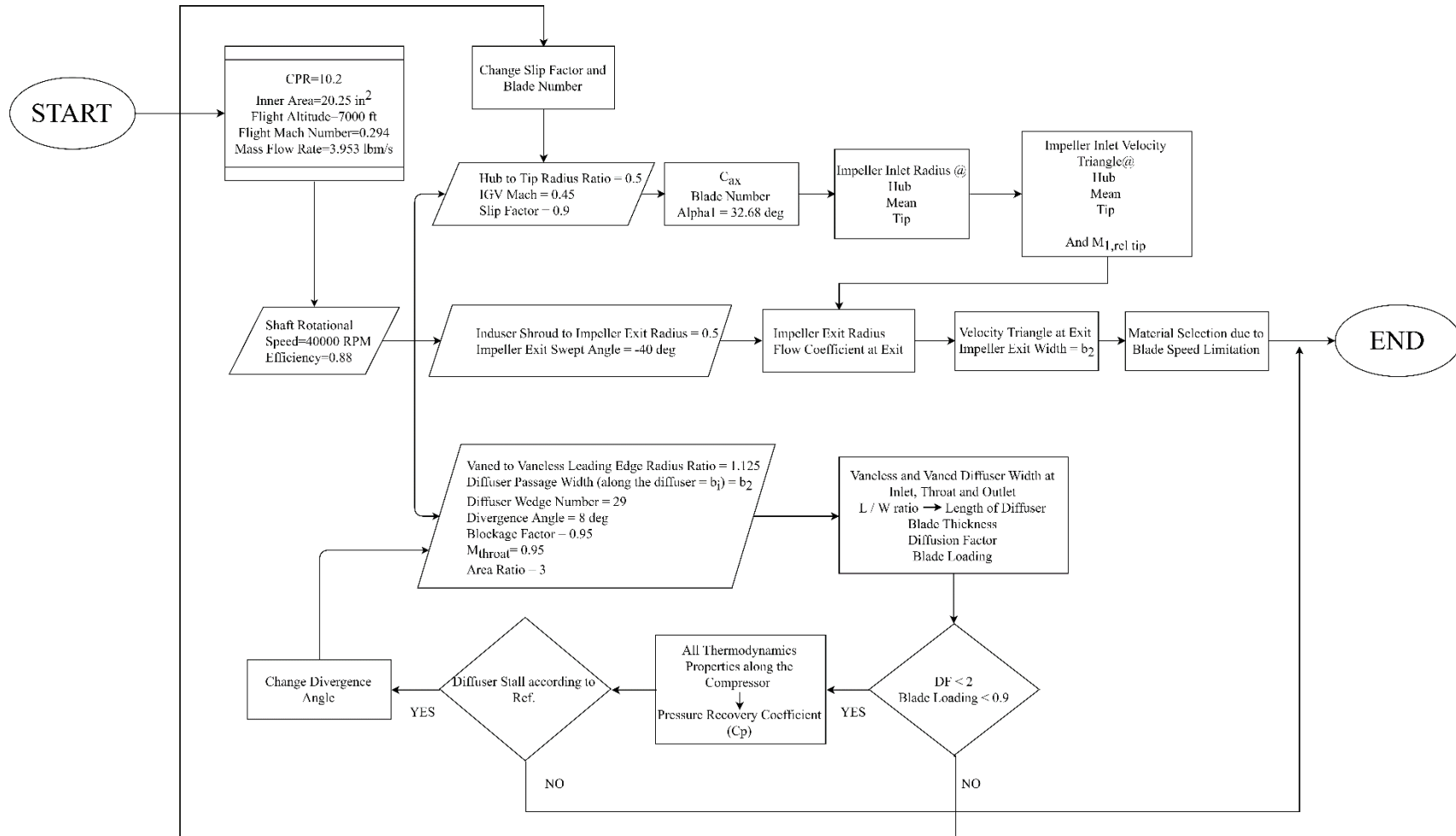


Figure 3.10: Compressor Design Flow Chart

## Chapter 4 Axial Turbine Design

In this chapter, the design and analysis of the axial turbines are presented. Design methodology, material selection, cooling type, and design point are determined. Further, types and value of losses, flow path calculation, and aerothermodynamic calculations, including hand calculations are discussed. Finally, blade and annulus sizing, the study of design point in the Smith diagram, airfoil design, and turbine mechanical analysis are covered. It should be noted that the developed code calculate all the design parameters. The code is written in MATLAB® and no commercial or industrial software is used.

### 4.1 Configuration

As shown in Figure 4.1, STS-1000 turboshaft engine consists of a single stage compressor turbine (CT) which is connected to the centrifugal compressor by a hollow shaft (high-pressure shaft) and rotates at the speed of 40000[RPM]. Also, the engine has a two-stage axial power turbine (PT) which is linked to the generator of the candidate aircraft by PT shaft (low-pressure shaft) to feed the electric motors. According to cycle design outputs (Table 2.10), the desired design of CT and PT is to generate shaft power of 750[hp] (including 30[hp] off-take power) and 603[hp] at the design point (loiter), respectively.

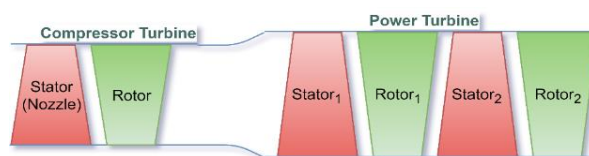


Figure 4.1: Overall Configuration of the CT&PT

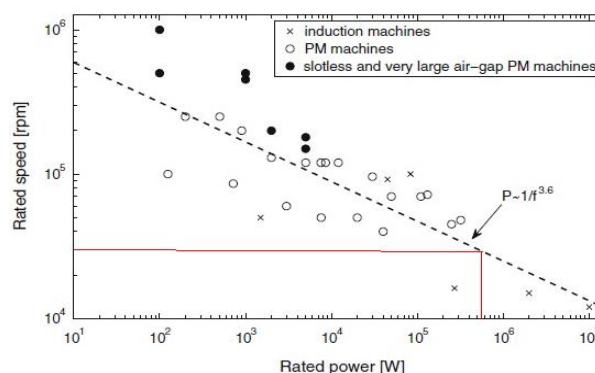


Figure 4.2: Rated Speeds of Existing High-Speed Machines [14]

Considering the required power of the air compressor, turbine inlet condition, and high speed of the shaft, the CT is determined to be a single stage. Based on Figure 4.2, the optimum rotational speed of the generator for producing a shaft power of 603 [hp] is approximately 22000 [RPM]. Further, in order to reduce the weight and increase the efficiency of the engine, a gearbox is avoided. Furthermore, the low-pressure shaft, which is linked to the PT, works at an optimum constant rotational speed, because of the sensitivity of the generator, battery working frequency, and the power intake. Thus, PT shaft speed would be 22000 [RPM]. As starting point, based on database engines and similar to MTR390-2c engine [15], PT is considered as a two-stage machine. After the initial calculations, and

considering dimensions and required power of the turbine, stage loading would be.  $\psi = 2.4 - 2.6$  According to Mattingly [3], for  $\psi > 2$ , the turbine should not be single stage to have a positive degree of reaction. Hence two stage assumption is valid for PT.

## 4.2 Design Methodology

To design the axial turbine, a code is developed to compute isentropic efficiency, number of blades, flow coefficient, velocity triangles, and other turbine parameters. CT and PT design flow chart are approximately similar to each other. In the following section, assumptions and inputs are discussed. One of the vital assumptions, is the axial entrance and exit flow velocity which is assumed constant with no swirl condition. No swirl condition will provide repeating stage design. Eq.(4.1) and Eq. (4.2) are used to calculate degree of reaction which should be equal to  $1 - \psi/2$ .

$$\alpha_0 = \alpha_2 = 0 \quad (4.1) \quad \alpha_2 = \tan^{-1} \left( -\frac{1}{2\varphi} (\psi + 2R) + \frac{1}{\varphi} \right) \quad (4.2)$$

### 4.2.1 Compressor Turbine

The input radii  $R_m$  and  $\psi$  are indirectly given through the knowledge of the required power and shaft speed.  $R_m$  varies from 3.5 to 5 [in]. This is similar to the turbine of MTR-2C390 engine [15]. Also, according to the Baskharone [17],  $\psi$  lays between 1.2-1.5. It should be mentioned that  $R_m$  is assumed constant for the CT design.

To have independent turbine operating conditions from upstream, the nozzle exit of the first stage should be choked. Thus, the Mach number at the throat is equal to one, and larger than one at the exit, and along the blade. Consequently, the nozzle exit Mach number at the mid has to be greater than one to assure the choked flow at the hub and tip. According to Mattingly [3], this amount is considered 1.09. Eq.(4.3) (Mattingly [3]) is used to calculate the exit flow angle at the nozzle exit.

$$\sin \alpha_2 = \frac{\left( \psi \frac{\omega r}{C_{1,m}} \right) - \left( \frac{C_{ax,3}}{C_{ax,2}} \tan \alpha_3 \right) \sqrt{1 + \left( \frac{C_{ax,3}}{C_{ax,2}} \tan \alpha_3 \right)^2 - \left( \psi \frac{\omega r}{C_{1,m}} \right)^2}}{1 + \left( \frac{C_{ax,3}}{C_{ax,2}} \tan \alpha_3 \right)^2} \quad (4.3)$$

### 4.2.2 Power Turbine

Although the design approach of PT is very similar to CT; however, it is not necessary for the exit flow of the first stage nozzle to be choked. The inlet velocity of the first stage of PT is known from the CT exit velocity. Again, by

calculating the exit flow angle of the nozzle, and assuming constant axial flow velocity through the turbine, the rotor entrance absolute velocity is computed. The design approach is illustrated in Figure 4.13. This procedure is repeated for the ranges of  $R_m$  and  $\psi$  of interest. In conclusion, considering the design criteria and the RFP requirements, the final design point is identified among different candidate design points.

### 4.3 Material Selection

As mentioned in Chapter 2, uncooled configuration is selected for the turbine. The maximum turbine inlet temperature is 2535.65 [°R]. Based on Figure 4.3, the temperature threshold of SiC/SiC CMC will reach 3200 [°R] by 2025. Considering that the maximum temperature which the turbine blades at CT nozzle faces is less than CMC cooling threshold, the assumption of no cooling technique for CT and PT in valid.

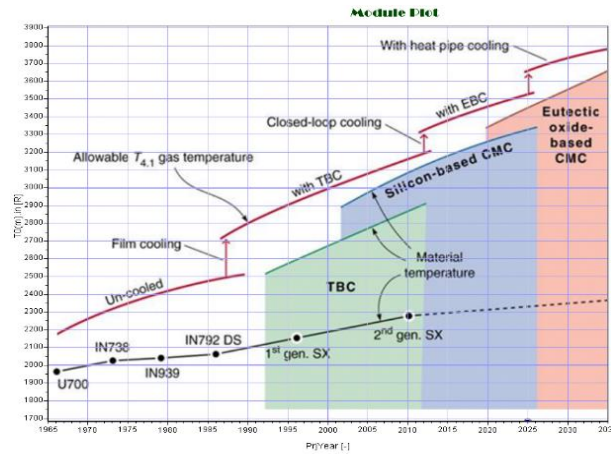


Figure 4.3: Cooling Technology Trend

### 4.4 Design Point Selection

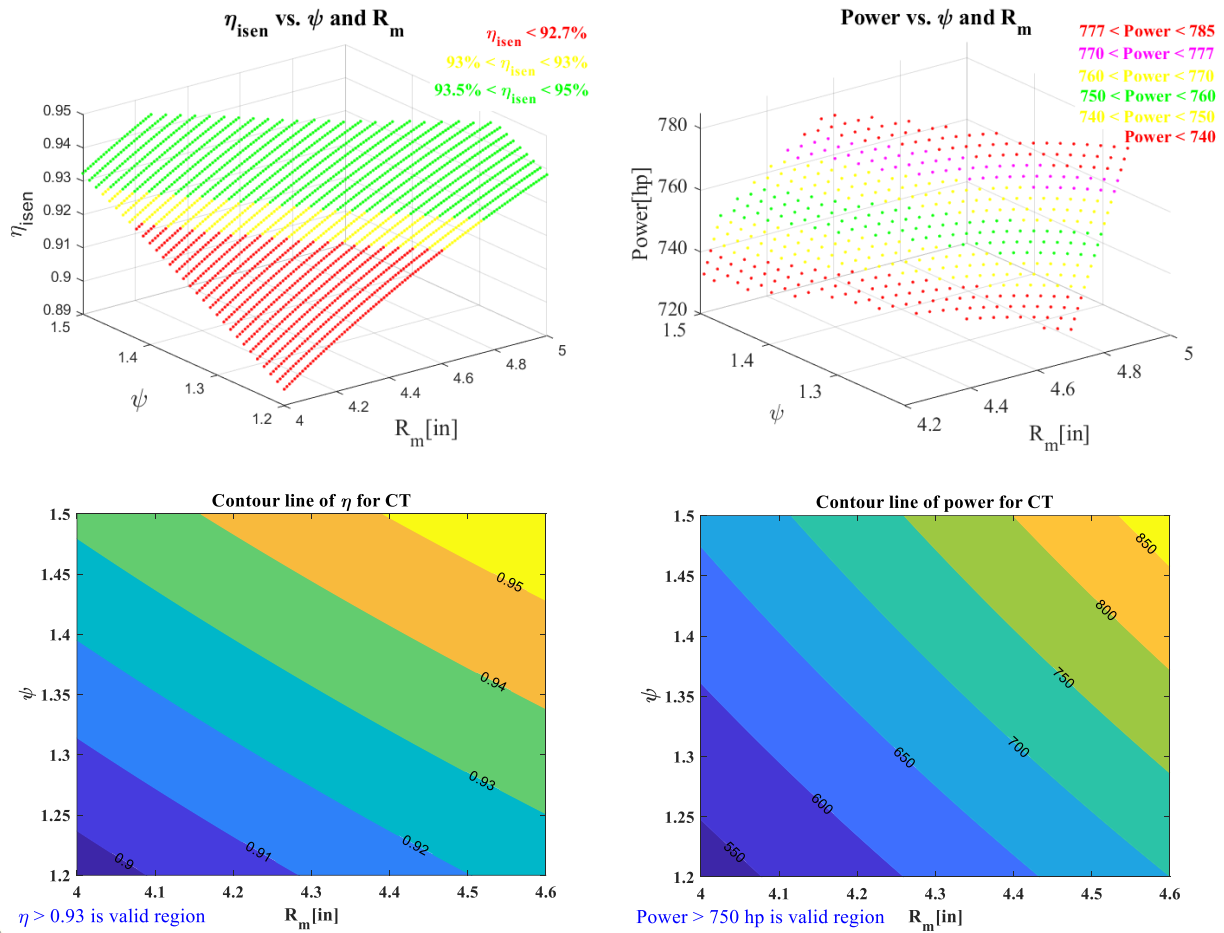
In this section, a parametric study is made for various  $R_m$  and  $\psi$  by considering selection criteria as given in Table 4.1. (With the difference that the required power for PT is 603 [hp]). Further the results are illustrated in Table 4.2 where the design point of CT lays between the colored rows.

Table 4.1: Design Point Selection Criteria

Parameter	$\eta$	Power	$\alpha_{1m}$	Smith chart
Value range	More than 93%	More than 750[hp]	Less than 70°	Appropriate location
Reference	Table 2.7	Table 3.2	Mattingly [3]	Lewis [18]

**Table 4.2: Candidate Design Points of CT**

$R_m$ [in]	$\psi$	$\varphi$	$\eta$	Power[hp]	$T_{t,2}$	$\alpha_{1,m}$	$M_{2,rel}$
4.3	1.2	0.88	0.91	611.39	1797.44	53.76	1.02
4.3	1.4	0.5	0.93	713.29	1738.68	70.21	0.85
4.4	1.3	0.65	0.93	693.5	1750.09	63.39	0.93
4.4	1.4	0.39	0.94	746.85	1719.32	74.33	0.84
4.5	1.2	0.76	0.92	669.59	1763.88	57.57	1.01
4.5	1.3	0.58	0.93	740.38	1731.7	66.12	0.92
4.6	1.3	0.49	0.94	757.98	1712.9	69.18	0.91
4.7	1.2	0.64	0.93	730.43	1728.79	61.83	1
4.7	1.3	0.4	0.94	791.3	1693.69	72.75	0.9
4.8	1.3	0.29	0.94	825.33	1674.07	77.25	0.89
4.9	1.3	0.12	0.95	860.07	1654.03	84.65	0.88
5	1.2	0.44	0.94	826.65	1673.31	69.69	0.98



**Figure 4.4: Contour of CT Candidate Design Points**

Similar to CT, calculations are repeated for PT design with the difference that the required power is known 603[hp].

The results are shown in Table 4.3.

**Table 4.3: Candidate Design Points of PT**

$R_m$ [in]	$\psi$	$\varphi_{s1}$	$\varphi_{s1}$	$\eta_{tot}$	$\eta_1$	$\eta_2$	Power	$\alpha_{1,m}$
5	1.2	0.811	0.811	92.04%	91.57%	91.66%	500.1	55.94
5.1	1.2	0.795	0.795	92.21%	91.73%	91.82%	520.3	56.47
5.2	1.3	0.78	0.78	92.79%	92.27%	92.39%	586	59.04
5.3	1.3	0.765	0.765	92.95%	92.41%	92.54%	608.8	59.52
5.3	1.4	0.765	0.765	93.31%	92.74%	92.89%	655.6	61.34
5.4	1.4	0.751	0.751	93.45%	92.86%	93.03%	680.6	61.79
5.5	1.2	0.737	0.737	92.84%	92.29%	92.43%	605.1	58.43
5.6	1.2	0.724	0.724	92.98%	92.42%	92.57%	627.4	58.89
5.7	1.3	0.712	0.712	93.52%	92.91%	93.09%	704.1	61.31
5.8	1.3	0.699	0.699	93.66%	93.02%	93.22%	729	61.72
5.9	1.4	0.687	0.687	94.13%	93.44%	93.69%	812.4	63.85
5	1.2	0.811	0.811	92.04%	91.57%	91.66%	500.1	55.94

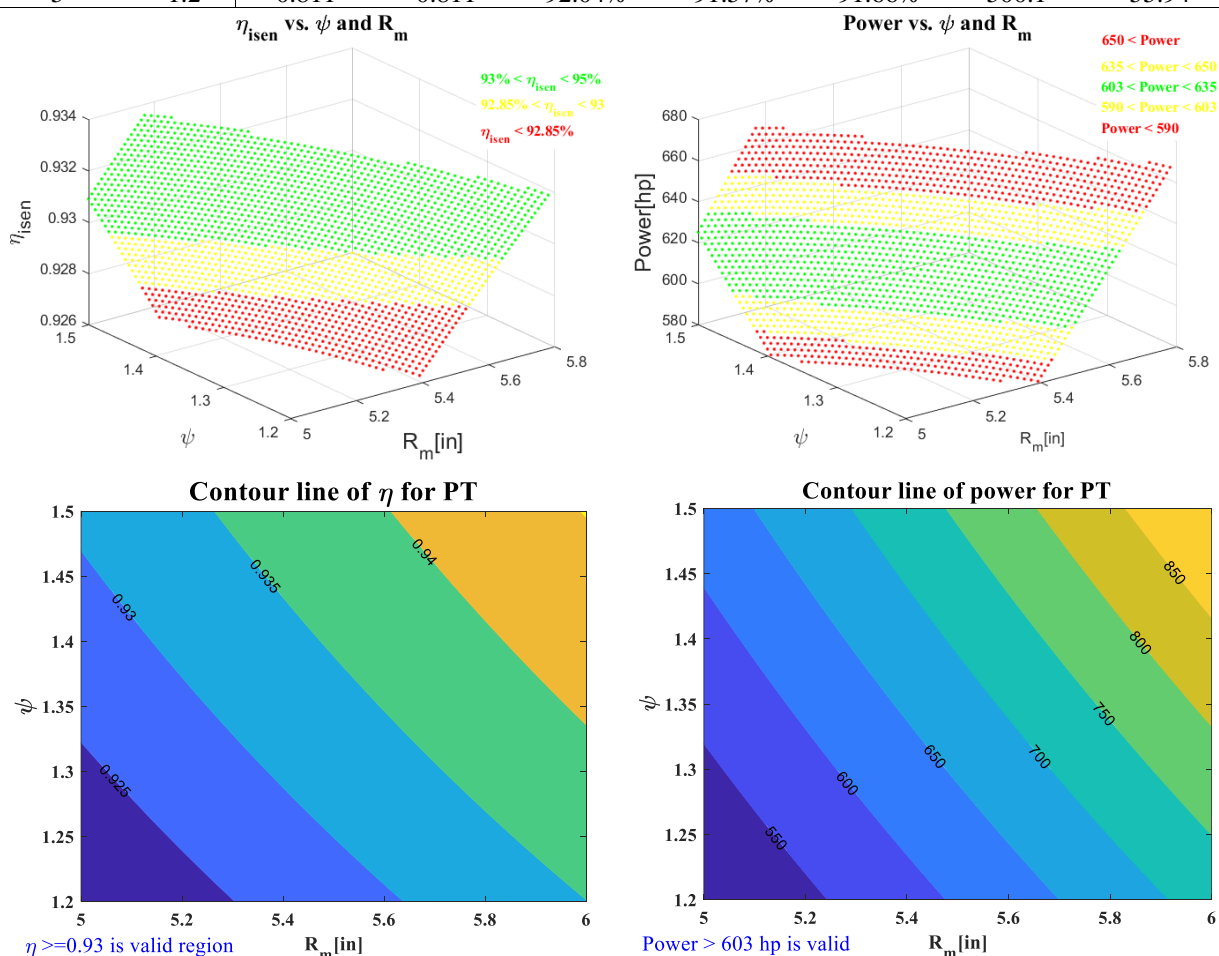


**Figure 4.5: Contour Candidate Design Points of PT**

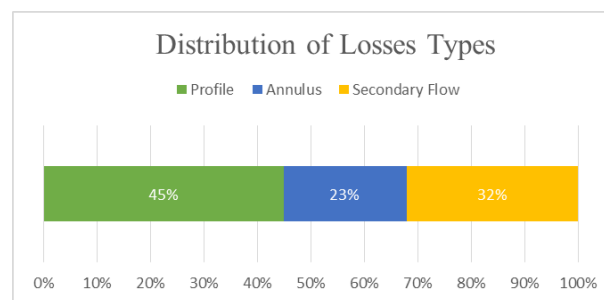
The final design point for CT and PT are summarized in Table 4.4.

**Table 4.4: Overall Specifications of Turbines**

Parameter	Power[hp]	$\eta$	$\omega$	$\psi$	$\varphi$	$^\circ R$
CT	753.45	93.65%	40000	1.315	0.4891	0.3425
PT	632.18	93.13%	22000	1.35	0.7625	0.3250

## 4.5 Losses

Considering the proposed engine configuration and the flight Mach number, according to [19] losses which are involved with a turbine blade, are the profile, secondary flow, and annulus (tip clearance, seal leakage, corner vortex, and so forth). The average distribution of loss types for both CT and PT is shown in Figure 4.6. The

**Figure 4.6: Distribution of Loss Types**

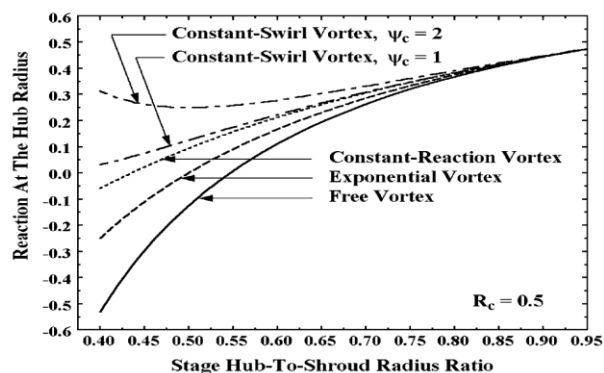
obvious point is that since this procedure is iterative, the loss calculation would be more accurate. Therefore, according to Aungier [20] and Mattingly [3], total losses of CT and PT can be calculated. For example, based on mentioned references profile loss of CT and PT are as follows:

**Table 4.5: Profile Loss Coefficient of Each Component**

Component	CT Stator	CT Rotor	PT Stage 1 Stator	PT Stage 1 Rotor	PT Stage 2 Stator	PT Stage 2 Rotor
Profile Loss Coefficient	0.058	0.122	0.032	0.075	0.031	0.079

## 4.6 Gas Path Calculation

In this section, gas path calculation is discussed. Assuming no swirl, the angles and values of the velocity at each point are calculated and also considering free vortex distribution, the velocity triangles at the tip and hub are obtained. Since  $R_h/R_t$  is near one, free vortex distribution is selected. According to Figure 4.7, this type of distribution is similar to other distribution types when  $R_h/R_t$  converges to one. Further, due to simplicity and avoiding an adverse degree of reaction, free vortex distribution is selected. Table 4.10 and Table 4.11 present velocity magnitude at each point.

**Figure 4.7: Stage Hub to Shroud Radius Ratio[20]**

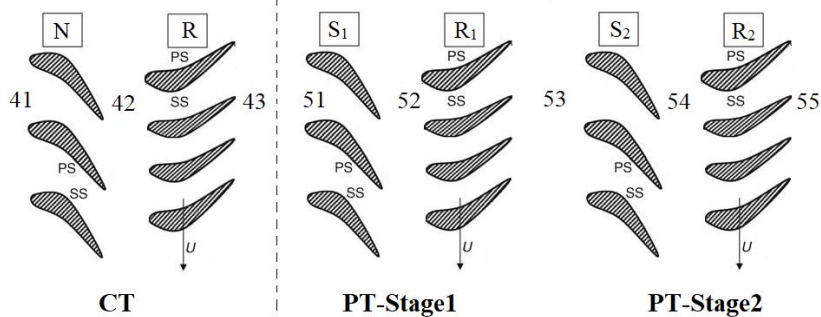


Figure 4.8: Stators And Rotors of STS-100 Turbines Pattern [19]

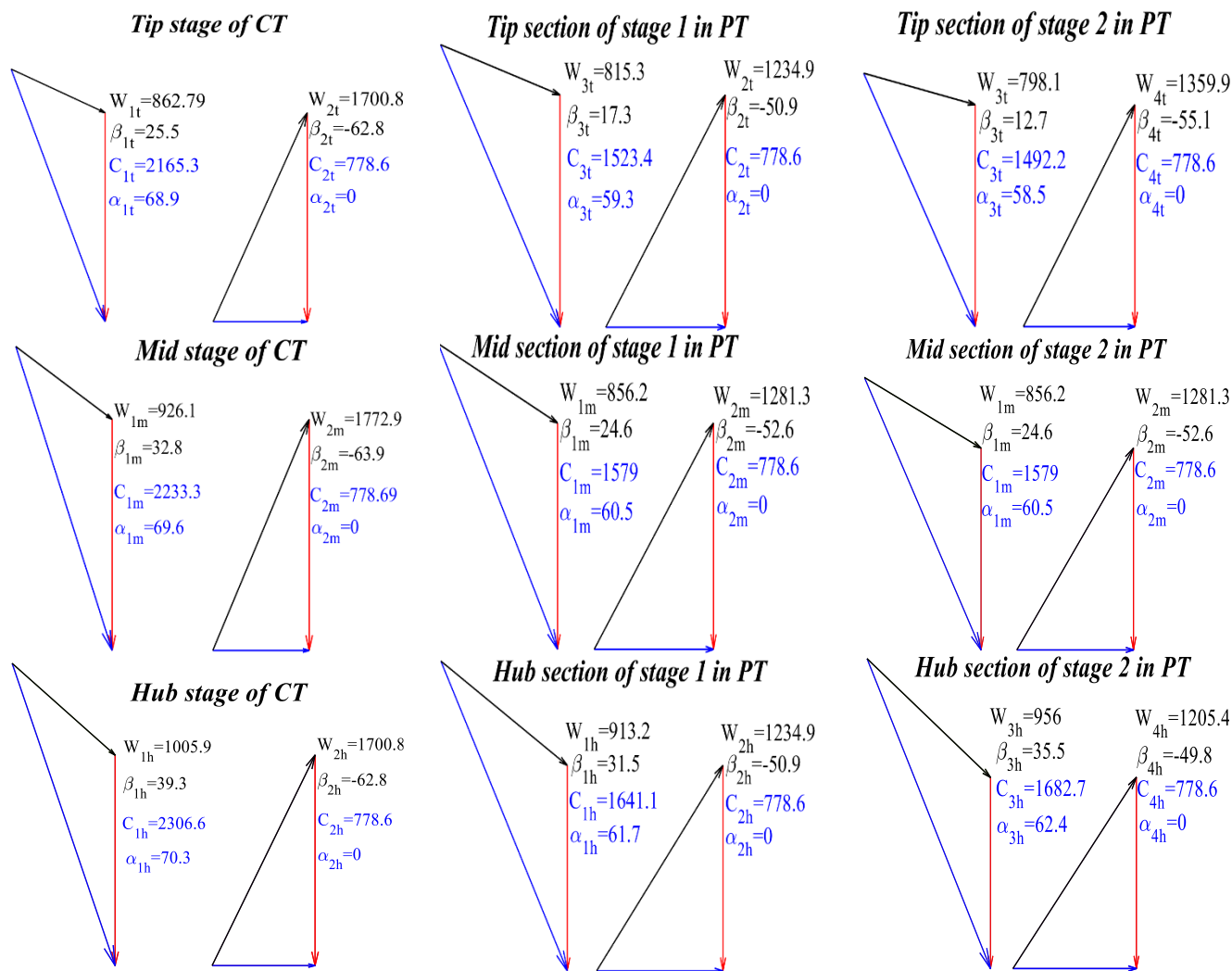


Figure 4.9: Velocity Triangles Across the Turbines

## 4.7 Aerothermodynamics

Using the velocity triangles in combination with the Bernoulli and energy conservation equations, flow thermodynamic properties are calculated.

From Table 2.10, CT inlet thermodynamic properties are  $T_{t,4}=2150[^\circ R]$ , and  $P_{t,4}=115.51 [psi]$  at loiter. Assuming constant total temperature through the nozzle and also using velocity triangles, all of the total and static

thermodynamic properties at rotor inlet are obtained. Moreover, supposing  $T_{t, \text{rel}43} = T_{t, \text{rel}42}$  across the rotor and using velocity triangles, all absolute and relative thermodynamic properties are computed at station 43. In the same way, this procedure is repeated for PT. Along the blade, the total temperature and pressure are constant, and by using the free vortex assumption and velocity triangles in each section, thermodynamic properties are computed. Table 4.8 and Table 4.9 represent all thermodynamic properties.

## 4.8 Blade Design and Annulus

Blade geometrical dimensions and the blade spacing are computed by using the Zweifel coefficient method presented in [3]. According to Mattingly [3], the appropriate efficiency range for Zweifel number lies between 0.8 to 1. The amount of 0.95 is chosen. Eq.(4.5) shows the relationship between the Zweifel number and the axial solidity. Hence, the axial solidity of rotors and stators are calculated.

$$H_{blade} = \frac{\dot{m}_{tot}}{2\pi R_m \rho_{s,0} C_{ax,1}} \quad (4.4) \quad \left( \frac{S}{C_{ax}} \right) = \frac{0.5Zw}{\cos(\beta_2)^2 (\tan(\beta_1) - \tan(\beta_2))} \quad (4.5)$$

Table 4.6: Blade Dimensions of CT

Parameter	Stator		Rotor	
Zw	0.95		0.95	
Solidity <sub>ax</sub>	0.688		1.093	
Throat	0.336		0.162	
R <sub>m</sub>	4.56		4.56	
R <sub>h</sub>	i:4.462	o:4.396	i:4.396	o:4.332
R <sub>t</sub>	i:4.658	o:4.724	i:4.724	o:4.788
Blade Length	i:0.197	o:0.328	i:0.328	o:0.457
Annulus	i:5.629	o:9.40	i:9.40	o:13.08
Pitch	0.3812		0.3590	
H/Chord <sub>ax</sub>	1		1	
Axial Chord	0.2623		0.3923	
Stagger angle	40.08		-30.45	
Chord	0.3428		0.4551	
Blade No.	76		80	
Solidity	0.899		1.268	

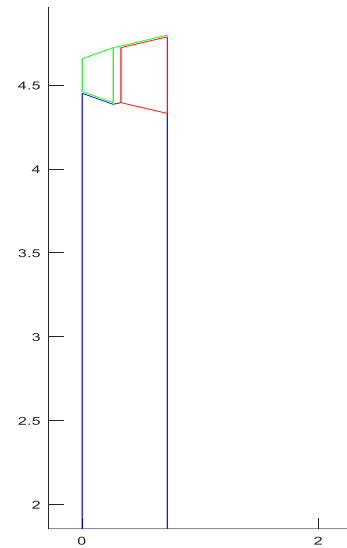


Figure 4.10: Side View of CT

Considering the continuity equation and using the density and velocity at each point, the required blade length and area are calculated (Eq.(4.4)). One of the essential parameters is  $H/\text{Chord}_{ax}$  which should be at least one [16]. If the amount of this parameter is less than one, tip clearance losses will increase. This coefficient is considered one for a purpose of an appropriate blade number. As a result, the value of  $\text{Chord}_{ax}$  is obtained.

The proper stagger angle is calculated using the blade inlet and exit angles. Other dimensions of CT are reported in Table 4.6. In the similar approach, PT blade dimensions are calculated and reported in Table 4.7. The  $H/\text{Chord}_{\text{ax}}$  coefficient for the first and second stages is selected 1 and 1.3 respectively. Table 4.7 summarizes the dimensions. Also, number of blades calculated by  $R_m$  and pitch. In Figure 4.13 the procedure logic of these calculations is demonstrated. The side view of CT and PT are shown in Figure 4.10 and Figure 4.11, respectively.

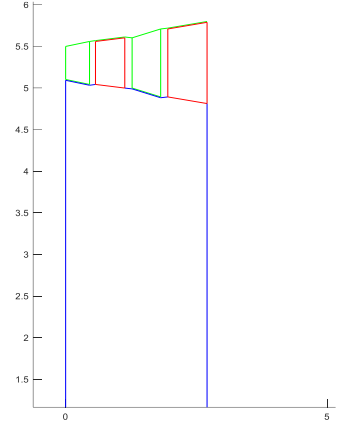


Figure 4.11: Side View of PT

Table 4.7: Blade Dimensions of PT

Parameter	Stator1		Rotor1		Stator2		Rotor2	
<b>Zw</b>	0.95		0.95		0.95		0.95	
<b>Solidity<sub>ax</sub></b>	0.867		1.316		0.867		1.316	
<b>Throat [in]</b>	0.381		0.287		0.455		0.384	
<b>R<sub>m</sub> [in]</b>	5.3		5.3		5.3		5.3	
<b>R<sub>h</sub> [in]</b>	i:5.106	o:5.042	i:5.042	o:4.998	i:4.998	o:4.892	i:4.892	o:4.812
<b>R<sub>t</sub> [in]</b>	i:5.498	o:5.558	i:5.558	o:5.602	i:5.602	o:5.708	i:5.708	o:5.788
<b>Blade Length [in]</b>	i:0.397	o:0.517	i:0.517	o:0.604	i:0.603	o:0.816	i:0.816	o:0.976
<b>Annulus [in<sup>2</sup>]</b>	i:13.22	o:17.20	i:17.2	o:20.10	i:20.09	o:27.19	i:27.19	o:32.50
<b>Pitch [in]</b>	0.5269		0.4255		0.6300		0.5703	
<b>Axial Chord [in]</b>	0.4567		0.56		0.5460		0.7506	
<b>H/Chord<sub>ax</sub></b>	1		1		1.3		1.3	
<b>Stagger angle</b>	34.42		-26.76		34.42		-26.76	
<b>Chord [in]</b>	0.5536		0.6272		0.6619		0.8406	
<b>n</b>	64		79		53		59	
<b>Solidity</b>	1.0507		1.4741		1.0507		1.4741	

## 4.9 Throat Design

To determine the size of the throat (O), method of [19] is used. Nozzle outlet of CT is the only throat that its Mach number would be more than one. Thus, for calculating O in this section Eq.(4.6) and in other throats Eq.(4.7) are used. The results are presented in Table 4.6 and Table 4.7.

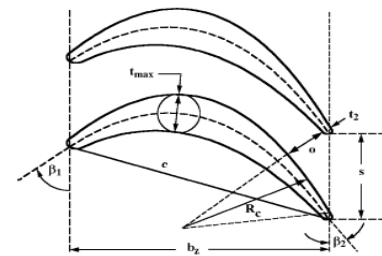


Figure 4.12: Throat of Blades [19]

$$O = \frac{S \times \cos(\alpha_e)}{A / A^*} \quad (4.6)$$

$$O = S \times \cos(\alpha_e) \quad (4.7)$$

**Table 4.8: Compressor Turbine Aerothermodynamics Result**

CT	T <sub>t</sub> [°R],			T <sub>s</sub> [°R],			P <sub>t</sub> [psi]			P <sub>s</sub> [psi]			M		
	Engine station	Tip	Mid	Hub	Tip	Mid	Hub	Tip	Mid	Hub	Tip	Mid	Hub	Tip	Mid
<b>41</b>	2150	2150	2150	2070.93	2070.93	2070.93	115.51	115.51	115.51	106.42	106.42	106.42	0.36	0.36	0.36
<b>42</b>	2150	2150	2150	1803.08	1824.79	1844.29	112.2	112.2	112.2				1.05	1.09	1.13
<b>42rel</b>	1892.8	1880.7	1869				59.24	62.83	54.25	57.72	55.13	52.34	0.42	0.45	0.49
<b>43</b>	1715.5	1715.5	1715.5	1675.98	1676.98	1677.98	40.25	40.25	40.25				0.4	0.4	0.4
<b>43rel</b>	1892.8	1880.7	1869				56.42	59.95	51.87	32.34	36.38	33.3	0.87	0.9	0.87

**Table 4.9: Power Turbine Aerothermodynamics Result**

PT	T <sub>t</sub> [°R],			T <sub>s</sub> [°R],			P <sub>t</sub> [psi]			P <sub>s</sub> [psi]			M		
	Engine station	Tip	Mid	Hub	Tip	Mid	Hub	Tip	Mid	Hub	Tip	Mid	Hub	Tip	Mid
<b>51</b>	1711	1711	1711	1625.98	1625.98	1625.98	39.76	39.76	39.76	35.83	35.83	35.83	0.4	0.4	0.4
<b>52</b>	1711	1711	1711	1548.2	1536.2	1522.3	39.22	39.22	39.22	26.21	25.4	24.49	0.8	0.83	0.87
<b>52rel</b>	1594.8	1587.6	1580.7				27	29	25.43				0.43	0.45	0.48
<b>53</b>	1515	1515	1515	1472.5	1472.5	1472.5	23.35	23.35	23.35	20.82	20.82	20.82	0.42	0.42	0.42
<b>53R</b>	1579.6	1579.6	1579.6				26.2	28.2	24.8				0.7	0.7	0.7
<b>54</b>	1515	1515	1515	1358.5	1340.2	1317.2	23	23	23	14.8	14	13.1	0.8	0.9	1
<b>54rel</b>	1403.2	1391.6	1380.9				15.3	16.3	13.7				0.4	0.5	0.5
<b>55</b>	1319	1319	1319	1276.5	1276.5	1276.5	12.7	12.7	12.7				0.4	0.4	0.4
<b>55rel</b>	1405.6	1391.6	1378.9				14.8	15.8	13.3	11.2	11.2	11.2	0.8	0.7	0.7

**Table 4.10: Compressor Turbine Flow Path Results**

CT	C(ft/s), Absolute Velocity			W(ft/s), Relative Velocity			U(ft/s), Blade Velocity			
	Engine station	Hub	Mid	Tip	Hub	Mid	Tip	Hub	Mid	Tip
<b>41</b>	778.6	778.6	778.6	*	*	*	*	*	*	*
<b>42</b>	2306.6	2233.3	2165.3	1005.9	926.1	862.7	1534.5	1591.7	1649	
<b>43</b>	778.6	778.6	778.6	1700.8	1772.0	1700.8	1512.1	1591.7	1671.4	

**Table 4.11: Power Turbine Flow Path Results**

PT	C(ft/s), Absolute Velocity			W(ft/s), Relative Velocity			U(ft/s), Blade Velocity			
	Engine station	Hub	Mid	Tip	Hub	Mid	Tip	Hub	Mid	Tip
<b>51</b>	778.6	778.6	778.6	*	*	*	*	*	*	*
<b>52</b>	1640.6	1579.0	1523.8	912.6	856.23	815.61	967.9	1017.5	1067.1	
<b>53</b>	778.6	778.6	778.6	1235.8	1281.3	1235.8	959.6	1017.5	1075.5	
<b>54</b>	1679.7	1579.0	1494.3	952.8	856.2	799.1	939.2	1017.5	1095.9	
<b>55</b>	778.6	778.6	778.6	1208.2	1281.2	1356.8	923.9	1017.5	1111.2	

## 4.10 Hand Calculation

$$\text{Input: } \psi = 1.315 \parallel R_m = 4.56 \parallel T_{t,1} = 2150 [^\circ\text{R}]$$

Assumption: Constant axial Velocity

$$\alpha_{m,0} = \alpha_{m,2} = 0 \parallel \text{Free Vortex}$$

Design Parameter :  $M_{1,m} = 1.09$

$$T_{1,m} = \frac{T_{t,1}}{1 + \frac{\gamma-1}{2} M_{1,m}^2} = \frac{2150}{1 + 0.15 \times 1.09^2} = 1536.20$$

$$P_{t,1} = \frac{P_{t,0}}{1 + \phi_{\text{profile}} \left(1 - \frac{T_{1,m}}{T_{t,1}}\right)^{\frac{\gamma}{\gamma-1}}} = \frac{115.51}{1 + 0.12 \left(1 - \frac{1536.20}{2150}\right)^{\frac{1.3}{0.3}}} = 112.2$$

$$C_{1,m} = M_{1,m} \sqrt{\gamma R_{\text{comb}} T_{1,m}} = 26799.3 \left[ \frac{\text{in}}{\text{s}} \right]$$

$$\sin \alpha_{2,m} = \frac{\left( \psi \frac{\omega r}{C_{1,m}} \right) - \left( \frac{C_{ax,3} \tan \alpha_3}{C_{ax,2}} \right)}{1 + \left( \frac{C_{ax,3} \tan \alpha_3}{C_{ax,2}} \right)^2} \times \sqrt{1 + \left( \frac{C_{ax,3} \tan \alpha_3}{C_{ax,2}} \right)^2 - \left( \psi \frac{\omega r}{C_{1,m}} \right)^2} = 69.5948$$

$$\begin{cases} C_{ax,1} = C_{1,m} \sin \alpha_{2,m} = 9343.78 \\ W_{ax,1} = C_{ax,1} = 9343.78 \end{cases}$$

$$W_1 = \sqrt{W_{ax,1}^2 + W_{\theta,1}^2} = 1111.34$$

$$\beta_{m,1} = \tan^{-1} \left( \frac{W_{\theta,1}}{W_{ax,1}} \right) = 32.78$$

$$\bullet C_{\theta,1} = C_{1,m} \cos \alpha_{2,m} = 25117.66$$

$$\bullet W_{\theta,1} = C_{\theta,1} - U_m = 6016.78$$

$$\begin{cases} C_{ax,2} = C_{ax,1} = 9343.78 \\ W_{ax,1} = W_{ax,2} = 9343.78 \end{cases}$$

$$\beta_{2,m} = \tan^{-1} \left( \frac{W_{\theta,2}}{W_{ax,2}} \right) = -63.93$$

$$C_{ax,h} = C_{ax,t} = C_{ax,1} = 9343.78$$

$$W_{ax,h} = W_{ax,t} = C_{ax,1} = 9343.78$$

$$\begin{cases} C_{\theta,2H} = \frac{R_m}{R_{\text{hub}}} C_{\theta,2m} = 0 \end{cases}$$

$$\begin{cases} C_{\theta,2t} = \frac{R_m}{R_{\text{tip}}} C_{\theta,2m} = 0 \end{cases}$$

$$\begin{cases} W_{\theta,2t} = C_{\theta,2t} - U_t = -18144.75 \end{cases}$$

$$\begin{cases} W_{\theta,1t} = C_{\theta,1t} - U_t = 20409.26 \end{cases}$$

$$\alpha_{t,2} = \tan^{-1} \left( \frac{C_{\theta,2t}}{C_{ax,t}} \right) = 0$$

$$\alpha_{h,2} = \tan^{-1} \left( \frac{C_{\theta,2H}}{C_{ax,h}} \right) = 0$$

$$\beta_{t,2} = \tan^{-1} \left( \frac{W_{\theta,2t}}{W_{ax,t}} \right) = -62.75$$

$$\beta_{h,2} = \tan^{-1} \left( \frac{W_{\theta,2H}}{W_{ax,h}} \right) = -62.75$$

$$\bullet C_{\theta,2} = C_{ax,2} \tan \alpha_{2,m} = 0$$

$$\bullet W_{\theta,2} = -U_m = -19100.88$$

$$\parallel C_{\theta,1H} = \frac{R_m}{R_{\text{hub}}} C_{\theta,1m} = 26054.93$$

$$\parallel C_{\theta,1t} = \frac{R_m}{R_{\text{tip}}} C_{\theta,1m} = 24245.48$$

$$\parallel W_{\theta,2h} = C_{\theta,2h} - U_h = -18144.75$$

$$\parallel W_{\theta,2h} = C_{\theta,2h} - U_h = 7641.16$$

$$\parallel \alpha_{t,1} = \tan^{-1} \left( \frac{C_{\theta,1t}}{C_{ax,t}} \right) = 68.92$$

$$\parallel \alpha_{h,1} = \tan^{-1} \left( \frac{C_{\theta,1h}}{C_{ax,h}} \right) = 70.27$$

$$\parallel \beta_{t,1} = \tan^{-1} \left( \frac{W_{\theta,1t}}{C_{ax,t}} \right) = 25.50$$

$$\parallel \beta_{h,1} = \tan^{-1} \left( \frac{W_{\theta,1h}}{W_{ax,h}} \right) = 39.28$$

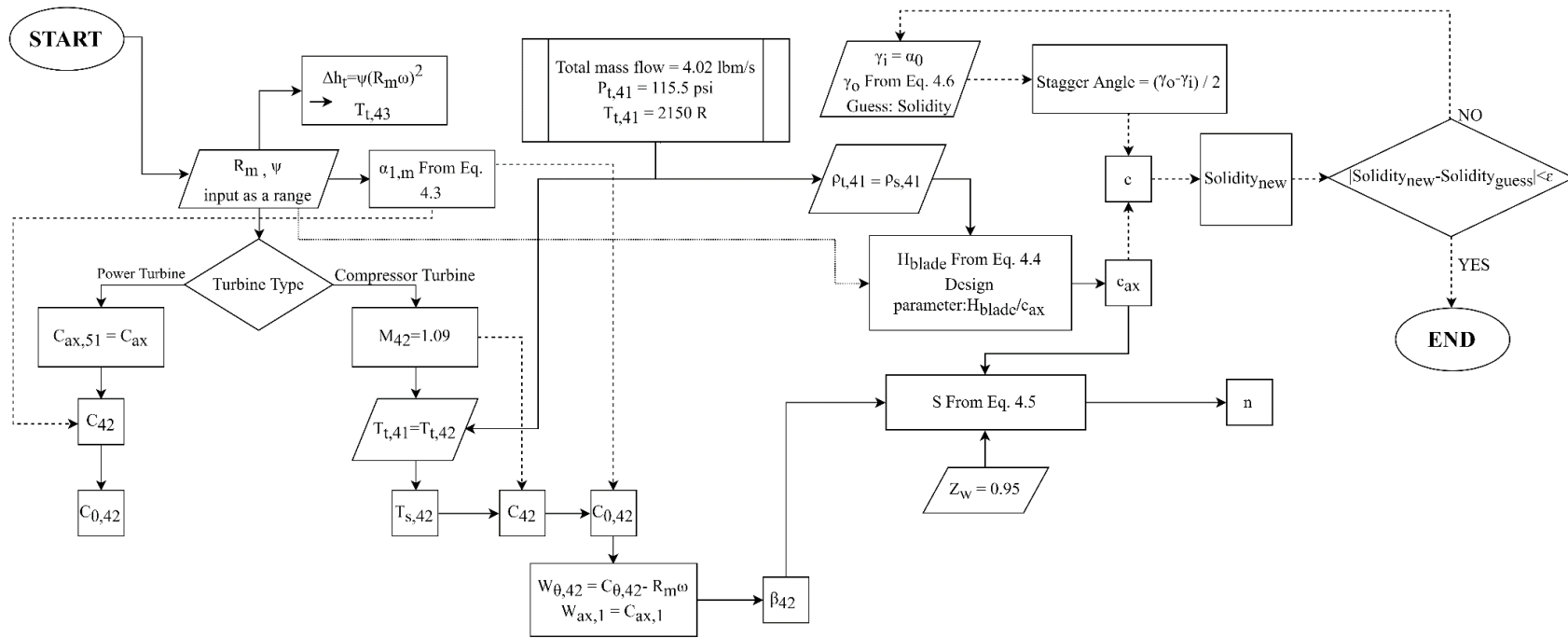


Figure 4.13: Turbine Design Approach

### 4.11 Smith Chart

Recalling the calculated values of  $\psi$  and  $\varphi$  for both CT and PT, the design considerations are shown in the Smith chart, Figure 4.14. The design point of CT is on the left side of the chart because its flow coefficient is low. High blade and shaft speed, and also the low axial velocity of flow (obtained from  $M_1=1.09$ ) results in a low flow coefficient. It should be emphasized that the high rotational speed of the shaft is stemmed from the compressor performance limitations. Also, PT design point located around the peak point which is good.

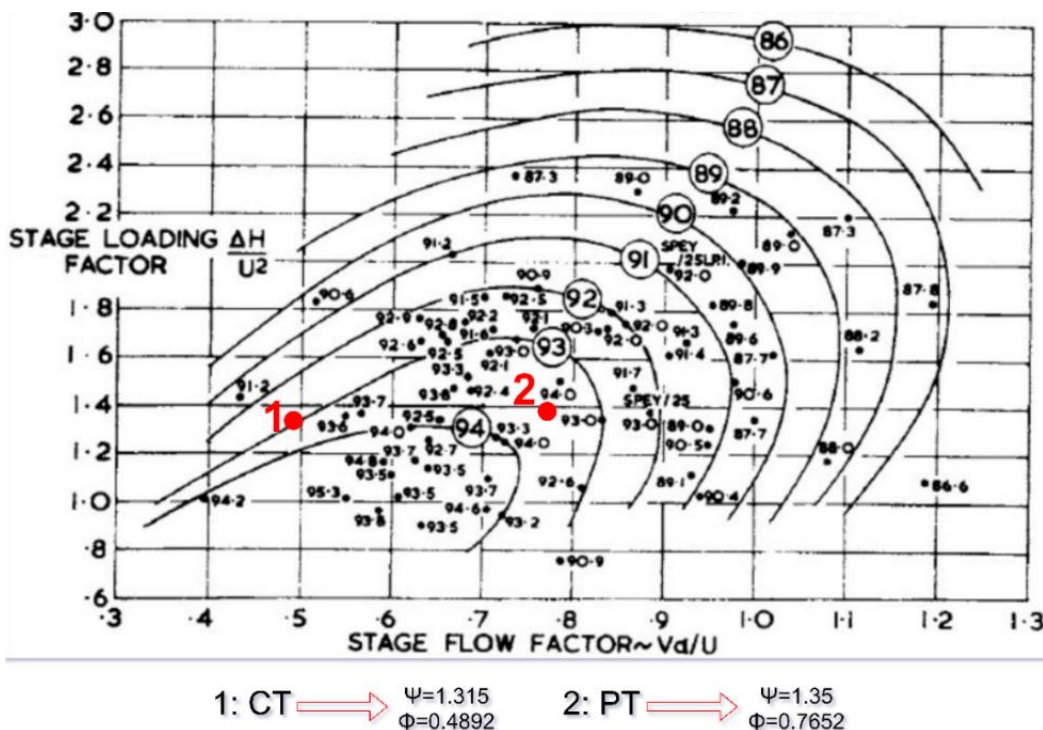


Figure 4.14: Smith Chart and Operating Point of CT and PT [18]

### 4.12 Airfoil Generation

Camber line coordination is obtained by the aid of superposition of Bèzier circles given by Schobeiri [21].

According to  $t/c_{max} = 0.15$ , the general airfoil surface coordinates are determined. The cross section of the turbine (in Figure 11.1) shows the airfoil shape.

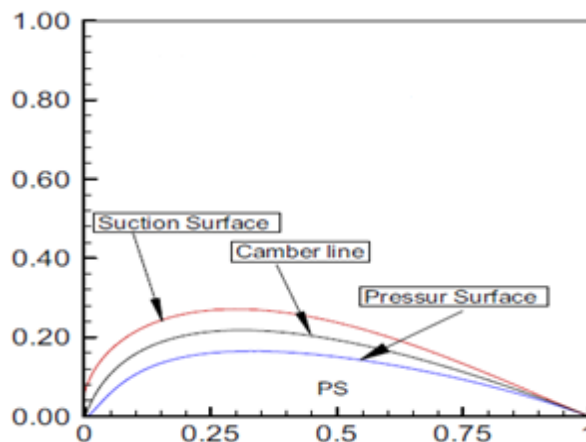


Figure 4.15: Turbine Blade Profile Schematic [21]

### 4.13 Turbine Mechanical Analysis

In this part, the mechanical analysis of the turbine blades of the STS-1000 is discussed in details. Stress analysis of each blade and vibration analysis of each turbine stage are demonstrated in Mechanical Analysis.

#### 4.13.1 Stress Analysis

Different types of turbine blade stresses are as follow.

##### Centrifugal Stress

One of the stresses which is applied to turbine blades is the centrifugal stress. It should be noted that this stress increases with the increase in blade twist and decreases with the decrease in taper ratio[4]. Thus, based on El-Sayed [4] the maximum centrifugal stress which occurs at the blade hub radius ( $r = r_h$ ) are:

$$\sigma_{r_{max}} = \rho_b \frac{U_t^2}{2} [1 - \zeta^2] = 2\rho_b \pi N^2 A \quad (4.8)$$

where  $\zeta = \frac{r_h}{r_t}$  is the hub-to-tip ratio, N is the rotational speed in rev/s, and A is the annulus area.

##### Gas Bending Stress

Another stress which is applied to turbine blades is the gas bending stress. Based on [4] the tangential

momentum is usually far greater than the axial momentum and the angle  $\phi$  is small, hence the gas bending moment is approximated as Eq.(4.9).

$$\left| \sigma_{gh_{max}} \right| \approx \left| -\frac{M_t y}{I_{xx}} \right| = \frac{\dot{m}(C_{\theta 1m} + C_{\theta 2m})}{n} \frac{h}{2} \frac{y}{I_{xx}} \quad (4.9)$$

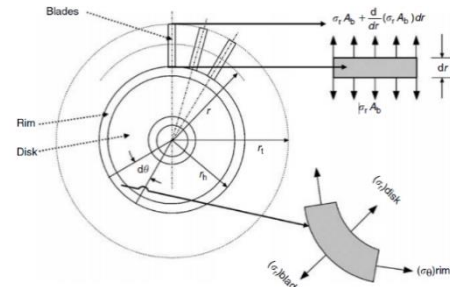


Figure 4.16: Centrifugal Stress of Disk and Blades [4]

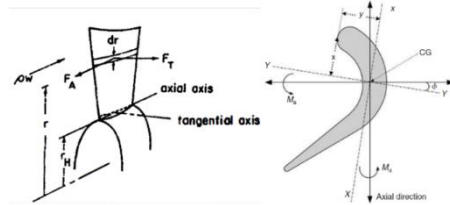


Figure 4.17: Gas bending Stress of Blades [4] and [35]

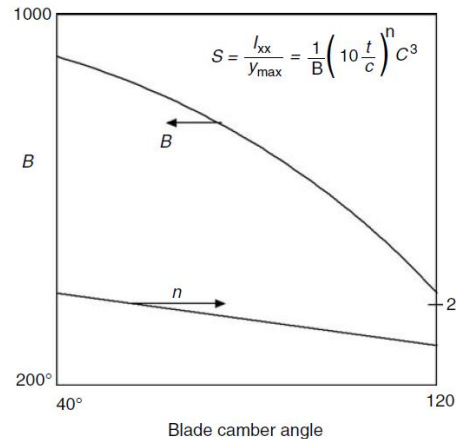


Figure 4.18: Approximate Rule for Section Module [22]

$$S = \frac{I_{xx}}{y_{Max}} = \frac{1}{B} \left( 10 \frac{t}{c} \right)^n C^3 \quad (4.10)$$

Where  $I_{xx} / y = S$  is the smallest value of section modulus. As reported in [22], the section modulus is expressed as Eq. (4.10). The variables (B, n) are plotted as a function of the blade camber angle in Figure 4.18.

### Thermal Stress

The thermal stress is caused by blade expansion which stems from the temperature augmentation. Thus, local thermal stress is developed, as:

$$\sigma_{thermal} = E\alpha\Delta T \quad (4.11)$$

where E is the modulus of elasticity of the blade material and  $\alpha$  is the coefficient of thermal expansion [4].

### STS-1000 Blade Stresses Results

The results of rotor blades stresses are shown in Table 4.12. It is worth mentioning that maximum total stress is the sum of absolute values of all stresses. The maximum stress on blades of each component (maximum between rotor and stator) are shown in Table 4.12.

**Table 4.12: Turbines Stress Analysis**

Component	Material	Yield Strength [ksi]	Centrifugal stress [ksi]	Gas bending stress [ksi]	Thermal stress [ksi]	Max. Total stress [ksi]	Margin of safety
CT	SiC/SiC CMC	363	13.18	3.0616	S: 52.69 R: 33.11	68.93	4.27
PT stage1	SiC/SiC CMC	363	4.93	1.1591	S: 17.72 R: 12.94	23.81	14.24
PT stage2	SiC/SiC CMC	363	7.96	1.0264	S: 26.54 R: 14.00	35.53	9.22

Therefore, all of the selected materials have reasonable yield strength and margin of safety. As a result, blades can tolerate the acted stresses on them.

## 4.14 Turbine Inflow Data

**Table 4.13: CT Inflow Data**

Flow Station Data at CT	
Inflow [lb/s]	4.0205
Corrected Inflow [lb/s]	1.0761
Inflow Total Pressure [psi]	115.51
Inflow Total Temperature [°R]	2150
Inflow Fuel-air Ratio	0.017
Inflow Mach #	0.36
Inflow Area [in <sup>2</sup> ]	5.629
Total Pressure Ratio	2.91

**Table 4.14: PT Inflow Data**

Flow Station Data at PT	
Inflow [lb/s]	4.0205
Corrected Inflow [lb/s]	2.8443
Inflow Total Pressure [psi]	39.76
Inflow Total Temperature [°R]	1711
Inflow Fuel-air Ratio	0.017
Inflow Mach #	0.4
Inflow Area [in <sup>2</sup> ]	13.22
Total Pressure Ratio	3.19

# Chapter 5 Combustion Chamber Design

The following section presents STS-1000 design and analysis of the combustion chamber. The STS-1000 employs a reverse-flow annular combustor same as TPE331-10. The reverse-flow combustor is best suited for application in small gas turbine engines that utilize centrifugal compressors. The compact design of this burner places the turbine inlet plane near the compressor

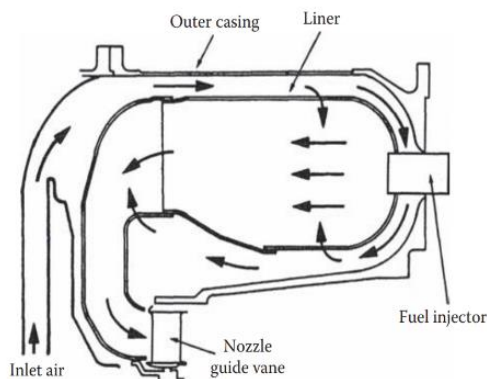


**Figure 5.1: Reverse Flow Annular Combustor [23]**

discharge plane and hence results in a shorter turbine–compressor shaft, although it suffers an added total pressure loss due to turning over a straight through flow burner [19]. Figure 5.1 shows a typical reverse-flow annular combustor. From the cycle design, combustor design point would be at  $T_{t3} = 1030.84$  [°R] and  $P_{t3} = 121.59$  [psi]. In the following subsections, combustor design details are elaborated.

## 5.1 Pre-Diffuser Design

The Mach number of the compressor’s exit flow is 0.25. To reduce the pressure loss and to have proper combustion, combustor inlet velocity has to be reduced. So, a flat wall pre-diffuser would be appropriate for the combustor. From the trade study, it can be concluded that the flat wall pre-diffuser would be apt for the combustor because its geometry is simple and tests can be carried out relatively easy [23]. Since the combustor inlet Mach number is not too large, a pre-diffuser would be sufficient to reduce the air flow velocity to a reasonable amount. Pre-diffuser sizing is done by Mattingly[3] method. Diffuser dimensions are related to its divergence angle and required efficiency. Thus, the first step is to determine the proper divergence angle which would result in appropriate  $L/H_1$ . According to the Figure 5.2 from Mattingly[3], it can be concluded that a divergence angle of  $\theta = 9^\circ$ , can avoid the flow going to stall region. Hence, the  $L/H_1$ .is selected to 1.55 and the respective area ratio would be  $AR = 1.5$ . The diffuser characteristics are shown in Table 5.1.

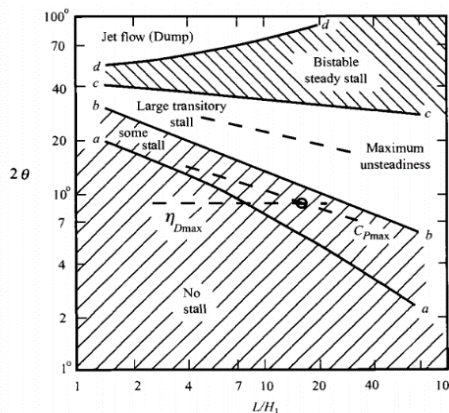


**Figure 5.2: Regimes of a Flat-Wall Diffuser [3]**

Pre-diffuser sizing is done by Mattingly[3] method. Diffuser dimensions are related to its divergence angle and required efficiency. Thus, the first step is to determine the proper divergence angle which would result in appropriate  $L/H_1$ . According to the Figure 5.2 from Mattingly[3], it can be concluded that a divergence angle of  $\theta = 9^\circ$ , can avoid the flow going to stall region. Hence, the  $L/H_1$ .is selected to 1.55 and the respective area ratio would be  $AR = 1.5$ . The diffuser characteristics are shown in Table 5.1.

**Table 5.1: Diffuser Specs**

Length [in]	Inlet area [in <sup>2</sup> ]	Outlet Area [in <sup>2</sup> ]	Aspect Ratio	Inlet Mach number	Outlet Mach number
1	26.75	40.13	1.5	0.25	0.16

## 5.2 Air Partitioning

Pre-diffuser airflow is partitioned into four parts: primary zone, secondary zone, dilution zone, and cooling flow. The table below shows the partitioning parameters which are determined by Mattingly[3] method.

**Table 5.2: Air Partitioning**

$\phi_{PZ}$	$\phi_{SZ}$	$\dot{m}_{PZ}$	$\dot{m}_{Cooling}$	$\dot{m}_{SZ}$	$\dot{m}_{Dilution}$	$\dot{m}_{Fuel}$	$\Phi$
0.6902	0.4858	1.4277	0.1456	0.6006	1.1786	0.0675	0.4794

### 5.2.1 Primary Zone

The first step to begin is to consider the primary zone maximum temperature. It should be noted that combustion emissions are a function of primary zone temperature ( $T_g$ ). Considering Figure 5.3, suitable temperature which would result in the minimum total emission is  $T_g = 3200$  °R. Mattingly [3] recommends that it is safe to assume combustion local efficiency ( $\epsilon_{PZ}$ ) about 0.7. It is worth mentioning that the assumed fuel is jet fuel  $C_{12}H_{23}$ , so the stoichiometric fuel/air ratio ( $f_{st}$ ) would be 0.0685

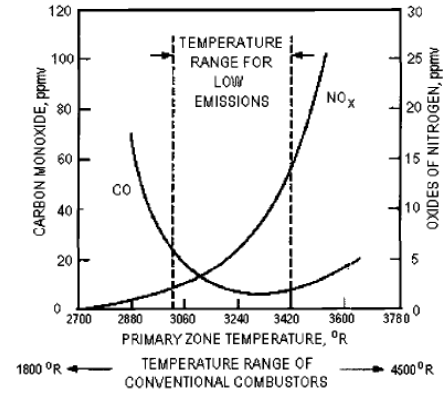
[lbmF/lbmA]. Therefore, the primary zone equivalence ratio ( $\Phi_{PZ}$ ) is calculated based on the above assumptions.

Finally, by using the Eq.(5.1) to Eq.(5.4), primary zone mass flow ( $\dot{m}_{PZ}$ ) is computed.

$$\Phi_{PZ} = \frac{T_g - T_{t3.1}}{\epsilon_{PZ} \Delta T_{MAX}} \quad (5.1) \quad \Delta T_{MAX} = \frac{T_{t4} - T_{t3}}{\phi_4} \quad (5.2) \quad \phi_4 = \frac{\dot{m}_{fMB}}{f_{st} \dot{m}_{3.1}} \quad (5.3) \quad \dot{m}_{PZ} = \frac{\dot{m}_{fMB}}{f_{st} \phi_4} \quad (5.4)$$

### 5.2.2 Liner Cooling

Combustion takes place in combustor liner where temperature rises to 3200°R in the primary zone whereas the liner wall needs to be kept near 2160°R. Therefore, it is necessary to devote a fraction of entering air for liner cooling. There are different types of cooling methods such as convective, impingement, film, transpiration, and etc. The transpiration holes on a surface and the cooling protection is akin to the film cooling technique, that is, by blanketing


**Figure 5.3: Influence of Primary Zone Temperature on CO and NOx[3]**

the surface with a coolant layer [19]. Moreover, this method of cooling needs less air flow than the other cooling techniques and can be considered as the utmost film cooling in the limit of infinitely many and continuously distributed film methods.  $T_m$  and  $T_c$  are the average wall material and cooling air temperature respectively. Also, it should be noted that  $T_c = T_{t3}$  which provided in cycle design. So, the cooling effectiveness ( $\Phi$ ) would be 0.4794 for  $T_m = 2160^\circ \text{R}$  and  $T_c = 1030.84^\circ \text{R}$ . Hence, based on these amounts, the cooling effectiveness can be determined. The Eq. (5.5) and (5.6) are used to determine the cooling mass flow and effectiveness.

$$\Phi = \frac{T_g - T_m}{T_g - T_c} \quad (5.5)$$

$$\dot{m}_{cooling} = \frac{\dot{m}_3}{25} \times \frac{T_g - T_m}{T_m - T_c} \quad (5.6)$$

### 5.2.3 Secondary Zone

It is desired that the combustion be completed at the secondary zone. Thus, its equivalence ratio and mass flow rate are calculated from Eq. (5.7) and (5.8).

$$\phi_{SZ} = \frac{T_g - T_{3.1}}{\Delta T_{MAX}} \quad (5.7)$$

$$\dot{m}_{SZ} = \dot{m}_{3.1} \left( \frac{\phi_4}{\phi_{SZ}} - \frac{\phi_4}{\phi_{PZ}} \right) \quad (5.8)$$

### 5.2.4 Dilution Zone

Dilution zone mass flow calculation is simple. The sum of the partitioned air should be equal to the entry flow.

$$\dot{m}_{DZ} = \dot{m}_{3.1} - \dot{m}_{PZ} + \dot{m}_{cooling} + \dot{m}_{SZ} \quad (5.9)$$

## 5.3 Combustor Sizing

Primary, secondary, and dilution zone dimensions are calculated. It should be noted that the sizing approach is based on Mattingly[3] and Lefebvre [23] and Melconian[24].

### 5.3.1 Casing Dimensions

In order to compute combustor dimensions, first casing area, liner area, and annulus area should be determined. Table 5.3 shows the casing dimensions.

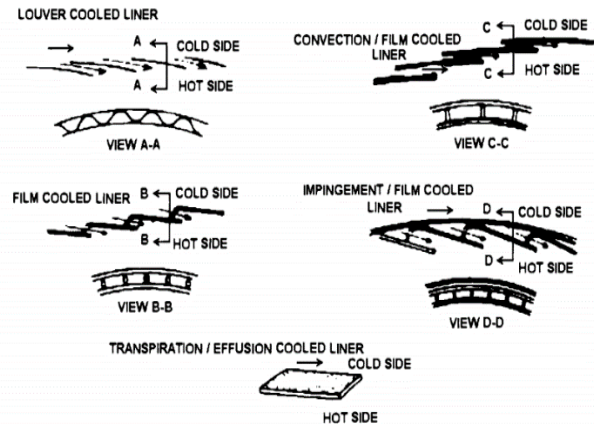


Figure 5.4: Liner Cooling Techniques[3]

**Table 5.3: Casing Dimensions**

$A_{\text{ref}} [\text{in}^2]$	$A_L [\text{in}^2]$	$D_{\text{ref}} [\text{in}]$	$D_L [\text{in}]$
111.8864	81.109	2.6981	2.1002

### 5.3.2 Primary Zone

Primary zone sizing is important because the main combustion occurs here. It is necessary to know the characteristics of the air swirler that are used to calculate the length of the primary zone. Radial air swirlers are considered for the combustor of the STS-1000 engine for two main reasons. First, they would reduce the emissions and second, they are relatively low in manufacturing cost. The length of the primary zone ( $L_{PZ}$ ) is 0.75 of the liner diameter ( $D_L$ ) [24]. The parameters  $S'$  and  $r_{\text{tip}}$ , that are the swirl number and the tip radius of the annular swirler, respectively, are calculated by using the method given by Mattingly [3] method. Hence, the following characteristics are obtained for the primary zone as shown in Table 5.4.

**Table 5.4: Primary Zone Specs**

$L_{PZ} [\text{in}]$	$N_{\text{noz}}$	$S'$	$r_{\text{tip}} [\text{in}]$	$r_{\text{hub}} [\text{in}]$	$\alpha_{\text{sw}} [^\circ]$
1.6196	8	0.7778	1.0797	0.5399	45

### 5.3.3 Secondary Zone

Secondary zone is responsible for the maximum amount of cooling in the main burner. The length of the secondary zone ( $L_{SZ}$ ) is 0.5 of the liner diameter [24]. The secondary zone air holes, their size, numbers, and positions are performed as mentioned by Mattingly [3]. The suggested depth of secondary air jet for having good penetration target is about 0.25 of the liner height for a target value of  $Y_{\text{max}}$ . A summary of the secondary zone characteristics is given in Table 5.5.

**Table 5.5: Secondary Zone Specs**

$L_{SZ} [\text{in}]$	$Y_{\text{max}}/d_j$	$d_j [\text{in}]$	$V_j [\text{ft/s}]$	$N_{h_{SZ}}$
1.0797	2.8485	0.1765	203.3806	242

### 5.3.4 Dilution Zone

The dilution zone is similar to the secondary zone except for the fact that it experiences a lower air entrance. The length of the dilution zone is calculated by using (5.10) [24]. The dilution zone air holes, their size, number, and location are computed as mentioned in Mattingly [3]. The suggested depth of the dilution air jet to have a good penetration target is about 1/3 of liner height for a target value of  $Y_{max}$ . The characteristics of the dilution zone are summarized in Table 5.6.

$$L_{DZ} = D_L (3.83 - 11.83PF + 13.4PF^2) \quad (5.10)$$

**Table 5.6: Dilution Zone Specs**

$L_{SZ}$ [in]	$Y_{max}/dj$	$dj$ [in]	$V_j$ [ft/s]	$N_{h_{SZ}}$
4.1410	2.8485	0.2353	203.3806	404

### 5.3.5 Combustion Chamber Length

The total length of the main combustion chamber is the summation of the length of the primary zone, secondary zone, and dilution zone. Total length is calculated and given in Table 5.7.

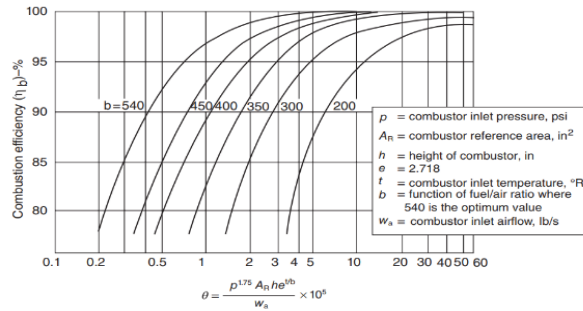


**Figure 5.5: Combustion Efficiency vs.  $\theta$  [23]**

**Table 5.7: Main Combustor Length**

Section	Primary Zone [in]	Secondary Zone [in]	Dilution Zone [in]	Total Length [in]
Length	1.6196	1.0797	4.1410	6.8403

### 5.3.6 Combustor Efficiency

For a gas turbine combustor, Lefebvre[23] suggests a combustor loading parameter (CLP)  $\theta$ , which correlates well with combustion efficiency. CLP parameter is defined as loading parameter that is highly dependent on the reaction rate parameter which is also dependent on the equivalence ratio of the primary zone. The Eq. (5.12) shows the dependency. Based on the amounts of,  $P_{t3}$ ,  $A_{ref}$ ,  $H$ , and  $\phi_{PZ}$ ;  $b$  and CLP can be computed. Next, with the aid of Figure 5.5 combustion efficiency is determined.

$$CLP = \frac{P_{t3}^{1.75} A_{ref} H e^{\frac{T_{t3}}{b}}}{\dot{m}_3} \quad (5.11) \quad b = 382 \left( \sqrt{2 \pm \ln \frac{\phi}{1.03}} \right) \left[ + \text{for } \phi < 1.03, - \text{for } \phi > 1.03 \right] \quad (5.12)$$

**Table 5.8: Combustion Efficiency**

$\phi_{PZ}$	<b>b</b>	CLP	Combustion Efficiency
0.6902	387.3138	$40 \times 10^5$	>99.5 %

### 5.4 Fuel Injection

The process of liquid atomization and evaporation is of essential importance to the performance of a gas turbine combustion system. Typically, two types of liquid atomizers are used; pressure-swirl atomizers and airblast atomizers. The major advantages of pressure-swirl atomizers are good mechanical reliability and sustain

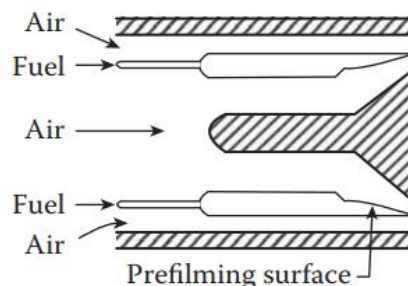


**Figure 5.6: Airblast Atomizer [23]**

combustion at weak mixture strength; however, their disadvantages consist a tendency toward high soot formation at high pressures and potential plugging of the small passages and orifices by contaminants in the fuel. On the other hand, airblast atomizers have some remarkable advantages. First, its fuel distribution is dictated mainly by the airflow pattern, and as a result, the exit temperature traverse is insensitive to variations in fuel flow. Moreover, the parts are protected from overheating by the air flowing over them. Although the airblast atomizer suffers from narrow stability limits and poor atomization quality at startup, these problems can be solved by combining the airblast atomizer with a pilot pressure-swirl atomizer. Based on these merits, airblast atomizer is suitable for combustion system.

### 5.5 Combustor Configuration

There are strict laws about emission production because of global warming. These laws force the aviation industry to produce NOx and CO as least as possible. So, the combustion configuration has paramount importance on emission reduction. There are three methods which are commonly used to reduce the emission production. These methods are RQL (Rich Burn-Quick Quench-Lean Burn), LPP (Lean Premix Prevaporize), and LDI (Lean Direct Injection). RQL combustion is one of the essential contenders in ultralow NOx emission. However, this type of combustion is not suitable for STS-1000 combustion chamber because the combustion is not rich-fuel in the primary zone. As stated in the air partitioning section, combustion occurs at a lean equivalence ratio. Although LPP combustor appears to have the most promise for ultralow NOx combustion, it suffers from the flashback in fuel preparation and autoignition since the long time needed to vaporize and mix at low power conditions fully. Finally, LDI is chosen as the combustion configuration since it has high combustion stability in addition to its light weight.

## 5.6 Emission

Today, the amounts of emissions, especially  $\text{NO}_x$ , are restricted by regulations. Based on Lewis correlation, the amount of produced  $\text{NO}_x$  is about 144.3 ppm. Also, the amount of  $\text{NO}_x$  using correlation by [25] is about 0.0057 lbm/lbm fuel. These amounts show that the combustion configuration and combustor components are suitable to reduce emissions.

## 5.7 Combustor Inflow Data

**Table 5.9: Combustor Inflow Data**

<b>Flow Station Data: Combustor</b>	
Inflow [lb/s]	3.95
Corrected Inflow [lb/s]	0.67
Inflow Total Pressure [psi]	121.58
Inflow Total Temperature [ $^{\circ}\text{R}$ ]	1030.84
Inflow Fuel-air Ratio	0
Inflow Mach #	0.25
Inflow Area [ $\text{in}^2$ ]	4.608
Total Pressure Ratio	0.95

## Chapter 6 Air Intake and Exhaust Duct Design

This chapter details the design of a S-duct intake for the target engine at the loiter phase. This intake should supply the required air mass flow for the centrifugal compressor considering the requirements from the engine cycle analysis. Further, the design of the exhaust component is covered.

### 6.1 Intake Characteristics

Most of the UAVs engines are embedded in the aircraft body. Hence, a possible inlet positioning is at the back and into the body. As a result, S-duct shape is chosen as the inlet type. Moreover, most of the search aircraft integrate their engines at the top of the aircraft in order

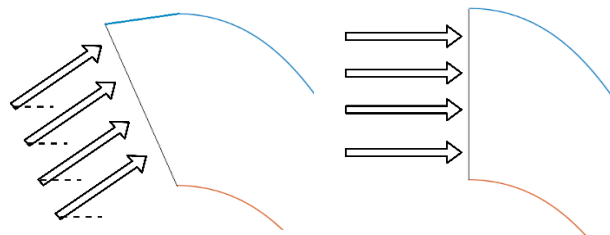


Figure 6.1: Inlet Flow Angle of Attack

to not blocking camera, and keep the proper distance from the ground on take-off and landing. So the inlet would be placed at the top as well.

A search UAV spends most of its time in loiter phase. Since there is not enough information about the inlet flow angle, drag polar, and aerodynamics coefficients of the UAV in the RFP, it is assumed that the flow enters the inlet fully axially and with zero angle of attack.

Since the flight Mach number is in low subsonic regime in all phases of the UAV mission, it can be concluded that the inlet works as a nozzle and accelerates the inlet flow [26]. So the intake should increase the ambient Mach number to the compressor inlet Mach number. In this case, the pressure gradient is always favorable and consequently, there would be no tendency for flow separation through the intake.

### 6.2 Intake Sizing

The general schematic of the STS-1000 engine inlet is shown in Figure 6.2.

#### 6.2.1 Design Assumptions

- An adiabatic process is assumed through the inlet and hence temperature stays constant.
- Considering the technology trend, the inlet pressure loss is assumed to be 1%. [3]

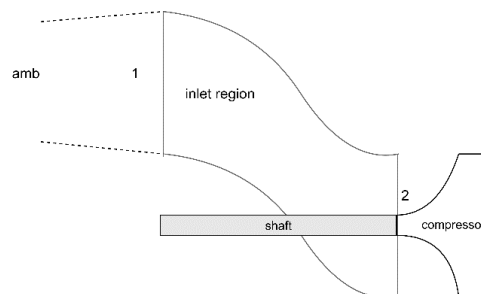


Figure 6.2: Schematic View of the Intake

Design parameters are given in Table 6.1

**Table 6.1: Intake Design Parameter Assumption [27]**

Parameter	Description	Equation	Range	Chosen
SF	Spillage Factor	$\frac{\dot{m}_{engine}}{\dot{m}_{amb}}$	0.85-0.9	0.9
VR	Velocity ratio	$\frac{v_1}{v_{amb}}$	0.5-0.9	0.9

## 6.2.2 Design Parameter Calculation

### Thermodynamic Condition

Considering the isentropic relations and the equation of state, the related thermodynamic properties for the intake design is given in Table 6.2:

**Table 6.2: Intake Flow Thermodynamics Properties**

$T_{ta}$ [°R]	$P_{ta} = P_{t1}$ [psi]	$P_t$ [psi]	$T_1$ [°R]	$\rho_1$ [slug/ft <sup>3</sup> ]	$M_1$
502.2	12.04	11.47	495.3	0.0019	0.26

### Intake Efficiency

As mentioned before, STS-1000 engine inlet acts as a nozzle. Thus, using Eq.(6.1), the nozzle efficiency is calculated to be 0.93.

$$\eta_{inlet} = \frac{1 - \left(1 + \frac{\gamma - 1}{2} M_2^2\right)^{-1}}{1 - \left(\left(\pi_{intake}\right)^{\frac{\gamma - 1}{\gamma}} \times \left(1 + \frac{\gamma - 1}{2} M_2^2\right)^{-1}\right)} \quad (6.1)$$

### Capture Area

Recalling the UAV flight velocity and the STS-1000 engine required mass flow, it is obvious that the inlet operates in a wide range of upstream flow conditions. Figure 6.3 shows the flow streamlines for the different subsonic conditions [4].

In this regard, the effective area at the compressor face is calculated by the following equation.

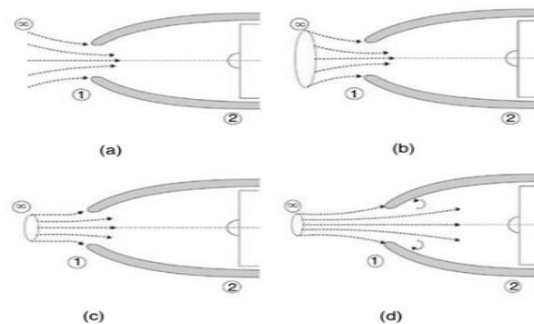


**Figure 6.3: Subsonic Intake Flow Streamlines, a) Ground Run, b) Climb, c) Cruise, d) Top Speed**

$$\frac{A_{amb}}{A_2} \times \frac{SF}{\pi_{intake}} = \frac{M_2}{M_a} \times \left( \frac{1 + \frac{\gamma-1}{2} M_a^2}{1 + \frac{\gamma-1}{2} M_2^2} \right)^{\frac{\gamma+1}{2\gamma-1}} \quad (6.2)$$

The results are presented in Table 6.3.

**Table 6.3: Sectional Intake Area**

$A_{amb} [\text{in}^2]$	$A_1 [\text{in}^2]$	$A^* [\text{in}^2]$	$A_2 [\text{in}^2]$
31.82	31.87	13.96	20.22

### Intake Throat Area

The intake throat area should be sized to assure no choking in the throat. However, this issue is not relevant in our case since the flight Mach number does not exceed 0.4. Eq.(6.3) and Eq.(6.4) are used to calculate the throat area [3].

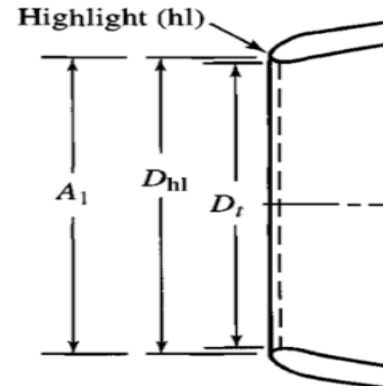


**Figure 6.4: Intake Throat Area [3]**

$$MFP = \frac{\dot{m} \times \sqrt{T_t}}{P_t \times A} = M \times \sqrt{\frac{\gamma}{R}} \times \left( 1 + \frac{\gamma-1}{2} M^2 \right)^{\frac{\gamma+1}{2(1-\gamma)}} \quad (6.3)$$

$$A_{throat} = \left( \frac{\dot{m}_{ca,max} \times \sqrt{T_{ref}}}{P_{ref}} \right) \times \frac{1}{MFP (@ M = 0.8)} \quad (6.4)$$

The maximum mass flow occurs at the take-off is calculated by Eq. (6.5).

$$\dot{m}_{ca,takeoff} = \left( \dot{m}_a \times \frac{\sqrt{\theta_a}}{\delta_a} \right)_{takeoff} = \dot{m}_{a,takeoff} \times \frac{P_{ref}}{\sqrt{T_{ref}}} \times \left( \frac{\sqrt{T_{ta}}}{P_{ta}} \right)_{takeoff} \quad (6.5)$$

The critical throat area is calculated to be 15.96 [in<sup>2</sup>] which this amount is smaller than this intake throat area.

## 6.3 Intake Geometry

In this section, the intake geometry and the positional integration of the STS-1000 engine shaft are discussed. In reality, intake length and height are strong functions of aircraft configuration, dimensions and engine positioning, but since these data is not available in this project, inlet length and height are selected according to reference engine. Baseline engine length is 43 [in] which inlet is about 25% of its length. Hence, since the length of the STS-1000 core engine is about 27 [in], the inlet length would be about 10 [in].

### Intake Center Line Equation

To obtain the intake curvature, the third order Bezier equations are used [28]. To draw this spline in Cartesian coordinates, four points are required which are shown in Figure 6.5.

$$\begin{aligned} x(t) &= (1-t)^3 x_0 + 3t(1-t)^2 x_1 + 3t^2(1-t)x_2 + t^3 x_3 & 0 < t < 1 \\ y(t) &= (1-t)^3 y_0 + 3t(1-t)^2 y_1 + 3t^2(1-t)y_2 + t^3 y_3 & 0 < t < 1 \end{aligned} \tag{6.6}$$

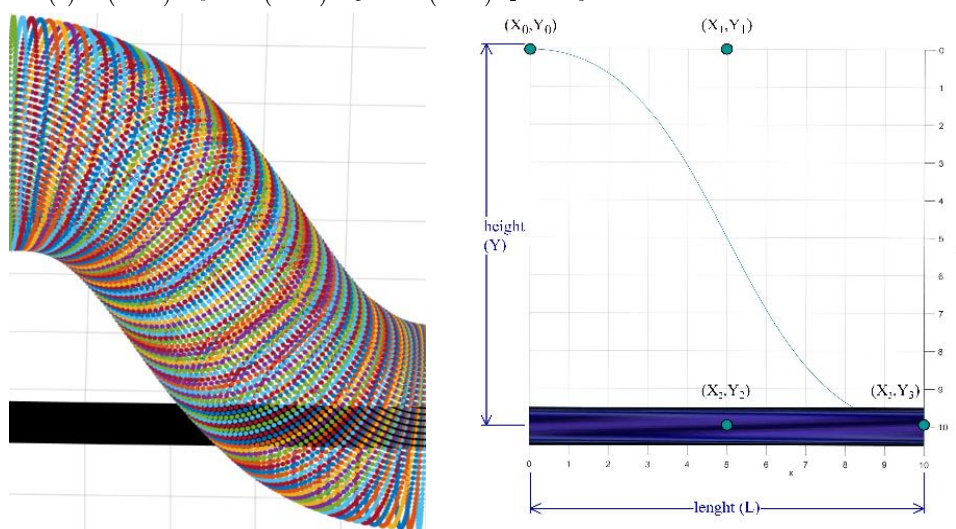


Figure 6.5: a) Final Intake Geometry      b) Center Line Equation

### Selection of Intake Section

Initially, the compressor intake section is assumed as a circle. However, at the intake entrance, it is suggested to have no corners or sharp edge and low similar to have an ellipse. Consequently, circular sections are considered at the end of the intake while starting from a semi-ellipse.

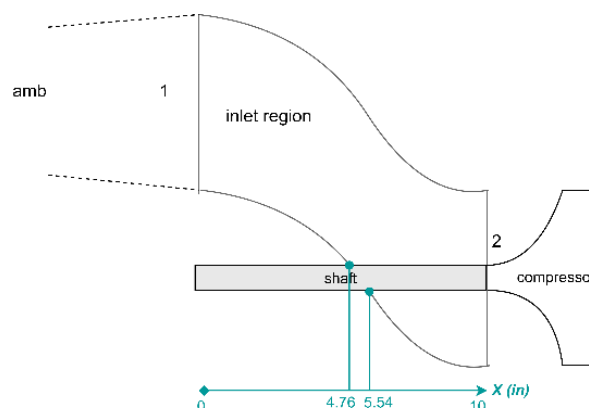


Figure 6.6: Shaft Exit Location

### Shaft Correction in the Intake

It should be noted that the compressor shaft goes through the center of intake and changing the effective area. Thus, the intake geometry needs to be corrected. To correct the area, shaft exit coordinates should be determined, and the subtracted area by the shaft should be added to the primary section area. In this regard, the exact exit position of the engine shaft through the intake is determined.

### Boundary Layer Correction in the Intake

The second correction is for considering the boundary layer effects in the intake. Since the flow is in the turbulent regime, a linear boundary layer growth is approximated. At the intake entrance, the boundary layer this effect is zero and grows at the intake exit; hence, an amount of 6% is added to the initial area [27]. Eventually

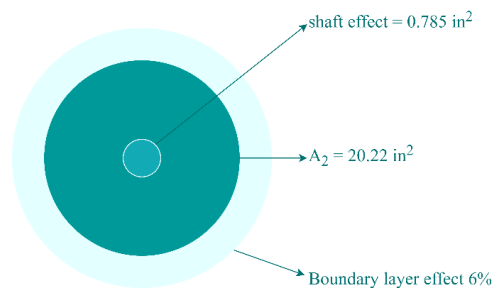


Figure 6.7: Compressor Entrance

at the compressor entrance according to Figure 6.7, the total area is calculated from Eq.(6.6) to be equal 22.27 [in²].

$$A_{compressor} = 0.06 \times (A_2 + A_{shaft}) + A_2 + A_{shaft} \quad (6.7)$$

## 6.4 FOD Problem

It is always possible that an external object enters the aircraft's engine intake during the flight. Therefore, it is important to protect the core engine from possible FOD. Since the engine's intake is of S type, and the flow changes its direction through the intake, foreign objects have little chance to reach the internal components. Further, a lattice screen is also placed at the leading edge of the intake, to prohibit the entrance of external objects.

## 6.5 Anti-icing or De-icing

Ice formation would decrease intake's performance, caused by:

1. Changes in the intake flow angle.
2. Air intake distortion and possible compressor surge.
3. Detached ice from the intake surface and sucked into the engine, and harming the downstream components.

To avoid this problem, generally two different methods are employed, these methods are anti-icing and de-icing. The difference between these two methods is that anti-icing, ice is not allowed to form on the surface whereas in de-icing the ice is removed when the aircraft and engine are at their thresholds [29]. Table 6.4 presents the pros and cons of each system.

Table 6.4: Comparison of De-Icing and Anti-Acing

De-icing	Anti-icing
✓ SFC is much less in this system than the other systems.	✗ It increases SFC since the required energy is supplied from high-pressure compressor stages
✓ It is activated on ordered time intervals.	✗ It consumes so much energy because it is always working.
✓ STS-1000 similar to TPE is supplied with this system.	✗ It is mostly used in conditions where it would be icing during flight.

Since, in our approach, the fuel consumption is more important, the de-icing system is selected.

### De-icing Technique

There are few techniques of de-icing like pneumatic boots, electromagnetic impulse de-icing (EIDI), and electric heaters. Pneumatic boots are not suitable for de-icing because there is a possibility of ice entrance to the compressor which may damage the IGV and impeller. Further, EIDI performs well for large engines. Therefore, in this proposal electric heater is used for de-icing. As shown in Figure 6.8, the heating elements surround the engine [29].

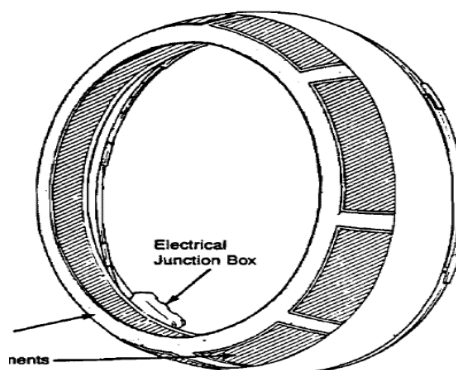


Figure 6.8: Engine Intake and De-Icing Element

## 6.6 Exhaust Duct Design

Recalling the requirements from the cycle design, the exhaust should reduce the turbine exit Mach number to 0.32 at the design point. Therefore, exhaust acts as a diffuser in STS-1000 engine.

### 6.6.1 Assumptions

The following assumptions are made

- Adiabatic process
- The static pressure at the nozzle equals to the ambient pressure.
- Considering the technology trend, the exhaust pressure loss will be 0.01 by 2025.

### 6.6.2 Exhaust Characteristics

The exhaust results are as follows:

Table 6.5: Exhaust Duct Characteristics

$T_{t9}$ [°R]	$P_{t9}$ [psi]	PR	Length [in]	$A^*$ [in <sup>2</sup> ]	$A_9$ [in <sup>2</sup> ]
1290.1	12.16	1.07	3	22.43	43.11

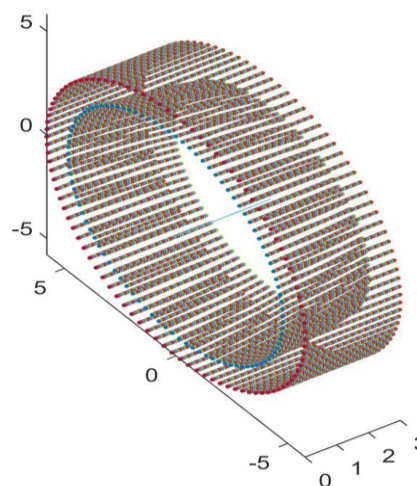


Figure 6.9: Exhaust Geometry

## 6.7 Noise Control

**Inlet:** The airflow in the inlet can be either axial or annular regarding the compressor type. In centrifugal compressor, the airflow is annular with and also include a plenum. The easiest method to insulate intake and compressor noise is using Helmholtz resonator liner in the plenum [30].

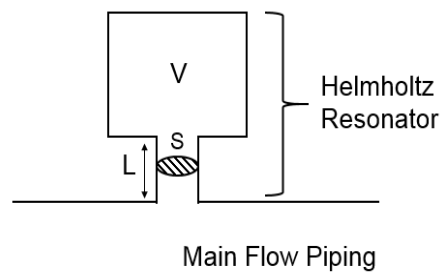


Figure 6.10: Helmholtz Resonator [30]

**Exhaust:** There are three main issues in exhaust insulation:

- The noise attenuation must be carried out over a very wide frequency range from 1kHz to 4 kHz.
- The liner should be able to withstand the high temperature environment at the outlet of the engine.
- The aerodynamic performances of the treated nozzle should be good. A clean flow diffusion must be insured.



Figure 6.11: Multi-duct Device [30]

The multi-duct channel concept has been designed in order to achieve a high-pressure recovery coefficient without increasing the axial length of the nozzle. Moreover, this solution makes available a large surface that can be treated leading to a very good acoustic attenuation. In the present case, the treatment area was more than doubled with respect to a standard single channel nozzle [30].

Two types of liners are used in this concept:

- Helmholtz resonator type with non-constant cavity depth and a resistive layer made of metallic felt
- The other made of glass fibers contained in perforate

Hence, based on the table below the metallic Felt is chosen.

Table 6.6: Exhaust Noise Reduction [30]

Configuration	Metallic Felt	Glass Fibers
$\Delta$ dB(A)	Better☑	
$\Delta$ TPNdB	Better☑	
$\Delta$ Power [%]	Same	Same
$\Delta$ Weight [kg]		Better☑

## 6.8 Material Selection

### Intake

Fiber-glass composite is selected as the intake material. This composite not only has low density but also can tolerate a high amount of force, and is early experience across to the aerospace industries. However, this material suffers from low tolerance of temperature gradients. Fiberglass composites are in different types. For this application, S-2 Glass Epoxy composite family is used since this type of composite is utilized when the component faces high stresses

### Exhaust

According to the nozzle geometry, nozzle material selection should be based on temperature considerations. Recalling the results from the cycle analysis, the selected material has to withstand temperature of at least 1600 °R. Moreover, the material should resist corrosion and exit gas impacts. For this part of the engine, Inconel 22 is chosen as the exhaust material which is an alloy constituted from Nickle.

## 6.9 Intake & Exhaust Duct Inflow Station Data

**Table 6.7: Intake Inflow Data**

Flow Station Data at Intake	
Inflow [lb/s]	3.95
Corrected Inflow [lb/s]	4.74
Inflow Total Pressure [psi]	12.04
Inflow Total Temperature [°R]	502.24
Inflow Fuel-air Ratio	0
Inflow Mach #	0.264
Inflow Area [in <sup>2</sup> ]	31.87
Total Pressure Ratio	0.99

**Table 6.8: Exhaust Inflow Data**

Flow Station Data at Exhaust	
Inflow [lb/s]	4.02
Corrected Inflow [lb/s]	7.73
Inflow Total Pressure [psi]	12.26
Inflow Total Temperature [°R]	1290.14
Inflow Fuel-air Ratio	0.017
Inflow Mach #	0.45
Inflow Area [in <sup>2</sup> ]	31.68
Total Pressure Ratio	0.99

## 6.10 Intake Design Procedure

Finally, the methodology of the intake design is as follows:

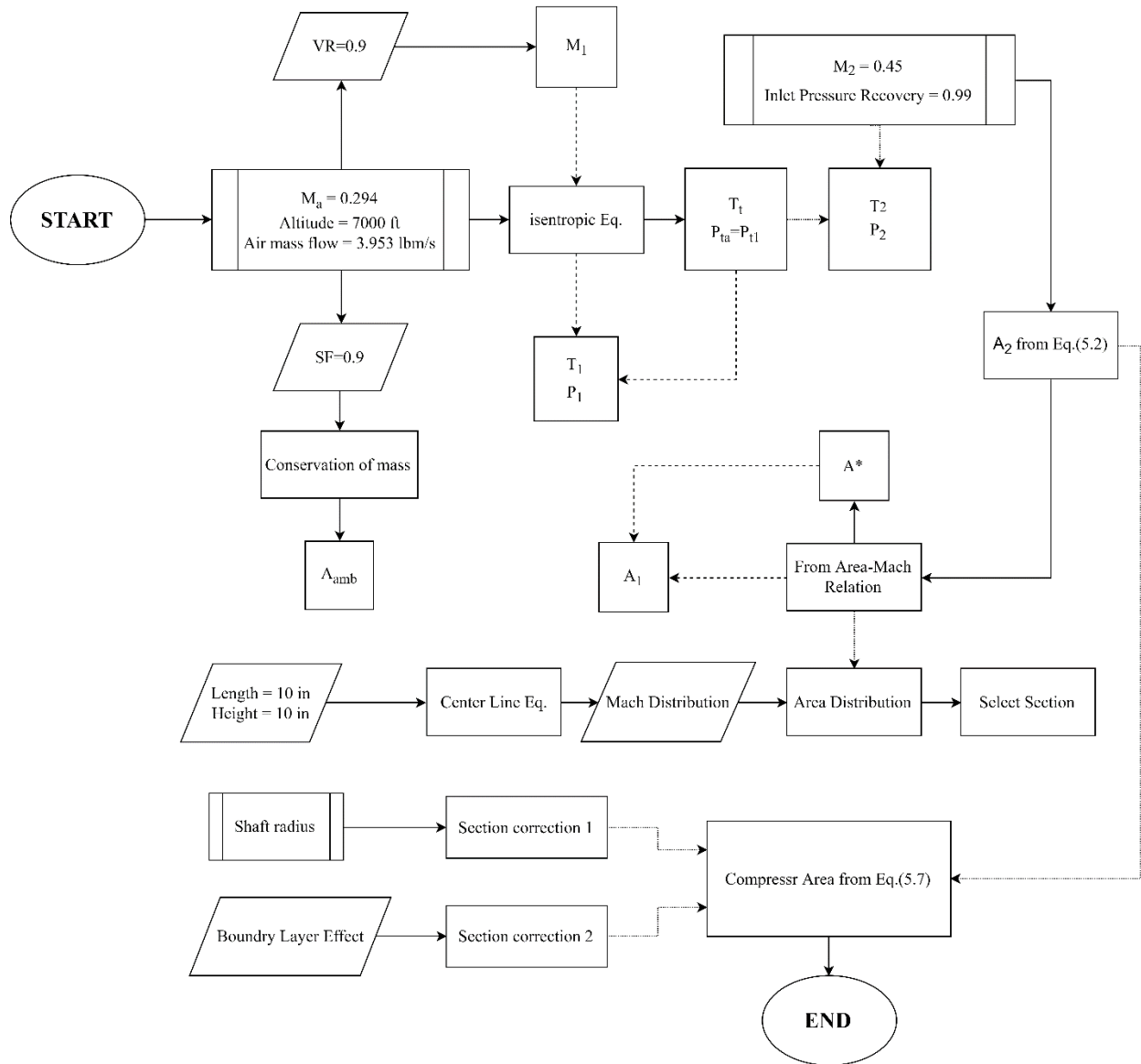


Figure 6.12: Intake Design Approach

## Chapter 7 Mechanical Analysis

In this chapter, the results for the STS-1000 mechanical design analysis are presented. For each component, the material, manufacturing, stresses, and natural frequencies are analyzed, and Campbell diagrams are plotted by using a code developed in MATLAB. Next, bearings type and positions are discussed. Finally, rotor dynamic analysis of the CT and PT shafts including their components are briefly discussed by using MESYS software [31].

### 7.1 Material and Manufacturing

This section details STS-1000 components material and manufacturing. Material properties which are mentioned in this section can be seen in Table 11.1.

#### 7.1.1 Intake

Fiber-glass composite is selected as the intake material. Fiber-glass composites are in different types such as A, C, D, E, R, and S2 Glass. In this application, the S-2 Glass Epoxy composite family should be used because this type of composite is utilized when the part faces high stresses. The manufacturing process of the fiberglass composite is molding. Figure 7.1 shows the schematic of the manufacturing process of the intake.

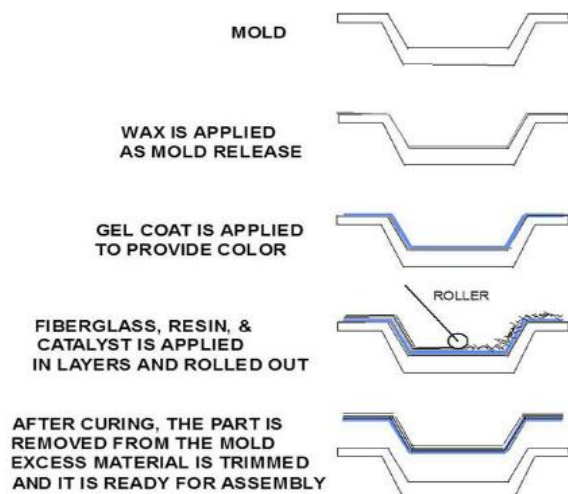


Figure 7.1: Manufacturing of Fiber-glass Composite Schematic

#### 7.1.2 Compressor

The selected material for the compressor is Titanium-6Al-4V. The compressor includes the IGV, impeller, and diffuser. A five-axis computer numerical control (CNC) is used for the manufacturing.

#### 7.1.3 Turbine and Combustion Chamber

Ceramic matrix composites “CMC” have higher temperature and pressure tolerance. Using CMC can

help to reduce NO<sub>x</sub> formation because it can tolerate higher combustion temperatures. It is worth mentioning that

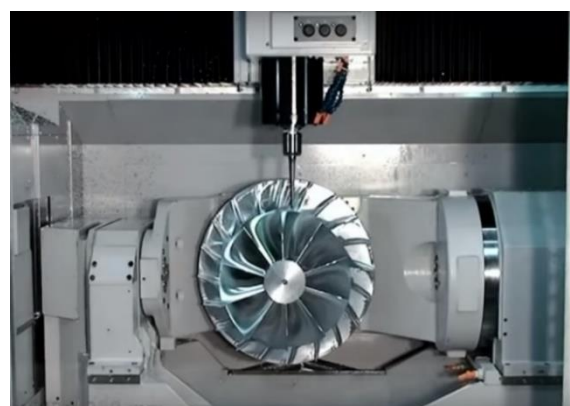


Figure 7.2: A Centrifugal Compressor Manufacturing Using a Five-axis-CNC

CMCs are generally cheaper than super-alloys [32]. CMC application in aero engines has become customary today. Recently, CMC is used by GE Company like GE-9X with TRL of 8.

Both the combustion chamber and the turbine (CT & PT) manufacturing are similar because they are silicon-based CMCs. CMC manufacturing process is as follows. First, SiC fibers are woven to each other in different angles and specific geometry. Second, these fibers are entered in a chemical vapor infiltration which causes the strength of SiC. Then, the chemical vapor infiltration is repeated on the fibers to increase density and cause matrix production. After that, CMC goes to polymer impregnation pyrolysis process which CMC is impregnated with polymer. Finally, CMC is put in the oven. If chemical vapor infiltration is sufficiently done, porosity and deformation will be seen [33].

### 7.1.4 Exhaust Duct

Inconel 22 is used for the exhaust duct and can be produced by casting, machining, cold and warm press. Hence, a 1.5 [mm]-thickness plate of Inconel 22 is used.

## 7.2 Stress Analysis

Through this section, each component stress is calculated as follow:

**Table 7.1: Components Stress Analysis**

Component	Material	Yield Strength [ksi]	Centrifugal Stress [ksi]	Gas bending Stress [ksi]	Thermal Stress [ksi]	Max. Total Stress [ksi]	Margin of Safety
Compressor	Ti-6Al-4V	133	-	-	-	Disk: 93.83	0.42
						Blade: 4.53	28.36
CT	SiC/SiC CMC	363	13.18	3.0616	S: 52.69 R: 33.11	68.93	4.27
PT stage1	SiC/SiC CMC	363	4.93	1.1591	S: 17.72 R: 12.94	23.81	14.24
PT stage2	SiC/SiC CMC	363	7.96	1.0264	S: 26.54 R: 14.00	35.53	9.22

From Table 7.1 it can be seen by inspection that all of the selected materials have a reasonable margin of safety and yield stress.

## 7.3 System Vibration Analysis

Vibrational analysis, natural frequencies calculation, and Campbell diagram are determined. In this section, blades of each component are modeled as a cantilever beam which rotates around the center of the shaft. Natural frequencies of the blades are modeled and calculated with the Rayleigh-Ritz method [34]. Considering initial boundary conditions, ten natural frequencies of each components' blade in their nominal shaft rotational speed are obtained.

According to Kerrebrock [35]: “The possibilities for excitation of a given blade can be represented by a "Campbell diagram" in which the frequencies of the various modes are plotted versus N and lines representing multiples of N are superimposed. Any intersection of the latter with a blade frequency curve within the normal speed range of the machine is a potential source of destructive vibration. Not all can be avoided, of course. The strongest excitation usually results from resonances with N, 2N, 3N, and perhaps 4N excitations, so it is usual to avoid these.” The results are shown in Table 7.2, Table 7.3, and Figure 7.3.

**Table 7.2: Components’ Blade Natural Frequencies**

Component Freq (KHz)	1 <sup>st</sup>	2 <sup>nd</sup>	3 <sup>rd</sup>	4 <sup>th</sup>	5 <sup>th</sup>	6 <sup>th</sup>	7 <sup>th</sup>	8 <sup>th</sup>	9 <sup>th</sup>	10 <sup>th</sup>
<b>CT</b>	34.7	48.1	76.5	81.4	97.7	111.2	123.2	132.4	151.8	160.4
<b>PT Stage1</b>	21.6	27.3	50.6	52.3	75.9	78.9	93.7	102.2	108.4	112.3
<b>PT Stage2</b>	12.3	17.7	34.1	38.3	46.7	47.2	59.6	62.9	68.6	76.7

**Table 7.3: Components’ Disk Natural Frequency**

Disk Freq (Hz)	1 <sup>st</sup>	2 <sup>nd</sup>	3 <sup>rd</sup>	4 <sup>th</sup>	5 <sup>th</sup>	6 <sup>th</sup>	7 <sup>th</sup>	8 <sup>th</sup>	9 <sup>th</sup>	10 <sup>th</sup>
<b>CT</b>	3198.22	3198.60	3212.40	3353.23	3353.96	4047.01	4047.15	5315.65	5315.77	5956.11
<b>PT Stage1</b>	1764.09	1764.35	1945.39	2042.17	2042.24	2075.43	3099.47	3099.52	4569.10	4569.20
<b>PT Stage2</b>	2159.77	2200.76	2200.94	2433.67	2610.82	2610.86	4027.73	4027.95	5926.98	5927.01

As mentioned before, critical speeds should not be in the range of components’ nominal rotational speed. If a critical speed is in that range, different techniques should be used to prevent it as in the following.

### 7.3.1 Techniques to Prevent Critical Speeds

To hinder the critical speeds reaching unsafe regions, different techniques are used which are categorized into three classes.

#### Geometrical Parameters

In this class, geometrical parameters of blades are modified. It should be noted that all of the modifications have to be checked by a turbomachinery designer so that it does not affect the blade’s aerodynamic performance significantly. These methods are **changing in thickness, considering the taper ratio for the blade, and changing the chord length.**

## Mechanical Friction Devices

Adding mechanical friction devices to components would change the blades' natural frequencies, and consequently, it prohibits the critical speeds reaching the forbidden region. These methods are as follow:

- **Blade Shroud:** this method reduces the tip clearance loss in addition to changing the natural frequencies.
- **Split ring:** these are a kind of static dampers which affect the natural frequency and also its response amplitude.

## Material

Changing the material of the components may hinder the critical speeds reaching an unsafe zone. The effective parameter in natural frequency is  $E / \rho$ . It should be pointed out that the selected material has to bear stresses and operational temperature.

## 7.4 Bearing Selection and Positioning

Bearings have a critical role in engine performance. Rotational elements are balanced at least by two bearings [35].

Bearings enhance shaft efficiency as well as shaft stability and engine rotor dynamics.

**Table 7.4: Components' Disk Natural Frequency**

<b>Used in aero-engines or not</b>	
<b>Roller bearing</b>	✓ Used!
<b>Tapered bearing</b>	✗ not used on turbine engine spools since they do not like operating at high DN values, due to the high friction losses created where the roller big end rubs against the race shoulders.[35]
<b>Ball bearing</b>	✓ Used!
<b>Magnetic bearing</b>	✗ Not used in aero-engines until today.

The STS-1000 engine considered using roller and ball bearings. Further, it should be said that magnetic bearings will not penetrate aircraft aviation engines until 2025 [35].

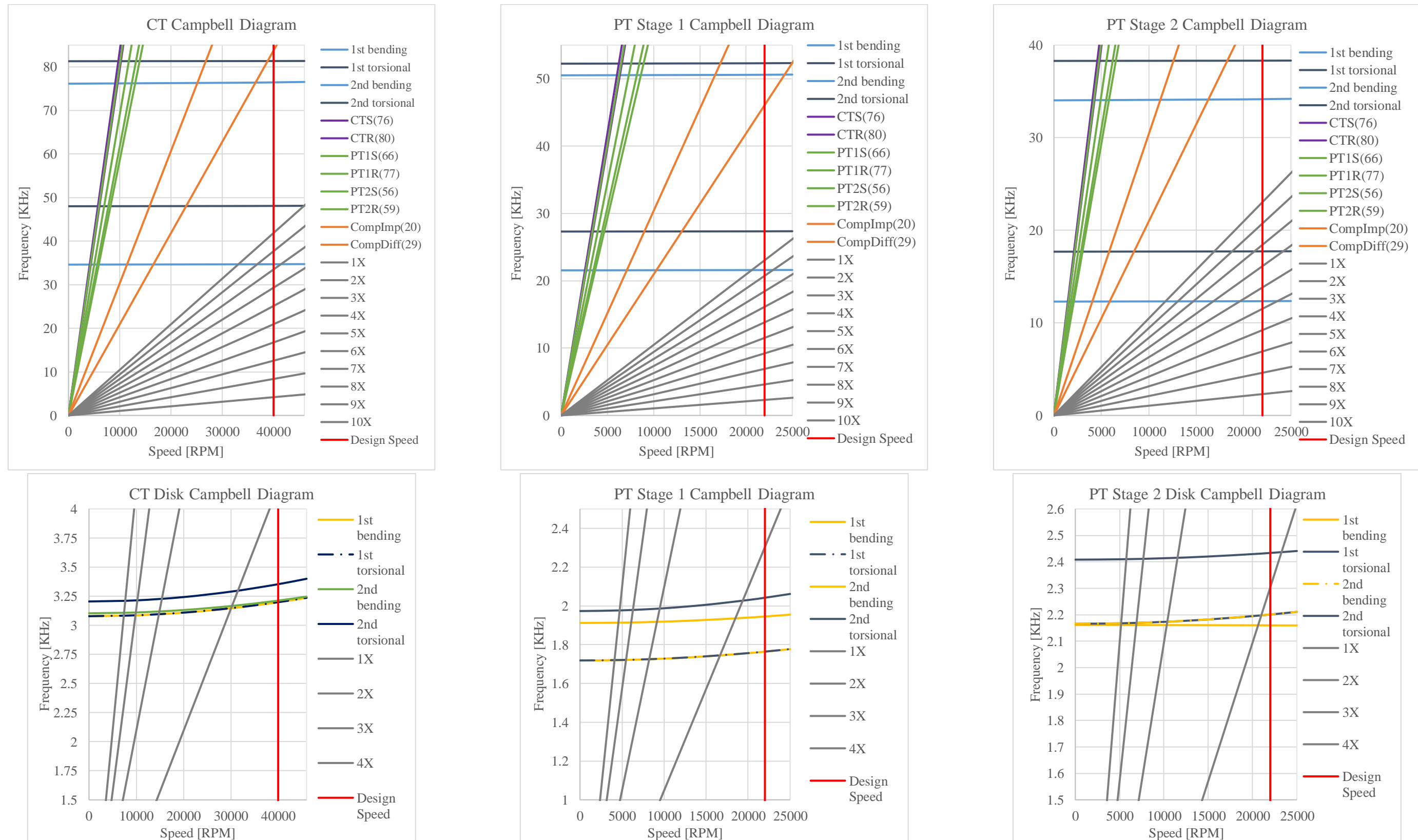


Figure 7.3: Campbell Diagram of Turbine Disks and Blade

### 7.4.1 Bearing Material

The M50NiL is used as the bearing materials. It is a high-speed bearing steel that is melted as VIM + VAR melt type, and its grade has increased molybdenum which helps to improve the wear resistance and strength at high temperatures. The inner and outer rings, as well as the ball and roller bearings, need to be made of a material that has a high heat resistance and fracture toughness. The carburized steel known as (AISI) M50NiL fits both needs. The material for the cage must also be chosen. Using current aircraft examples, the cages will be (SAE) 4340 alloy steel. The properties of both materials are given in Table 7.5.

**Table 7.5: Bearing Material Properties**

Material	Density [lb/in <sup>3</sup> ]	Hardness [HRC]	Tensile Strength Yield/Ultimate [ksi]	Fracture Toughness [ksi.in <sup>2</sup> ]	Fatigue Life [L <sub>10</sub> Dynamic Life Factor]
AISI M50NiL	0.285	47	174/203	50-52	12-16
SAE 4340	0.284	30	103/161	45.5	~

### 7.4.2 Bearings Positioning

Rotational components of the engine, specifically the turbine and compressor should be supported radially and axially. Since there is a longitudinal thermal expansion across the engine, the supporting bearing is selected to be ball type so that it bears the axial and radial forces, and the remaining are of roller type to afford longitudinal displacement caused by thermal expansion [35]. According to [34] and [36], it is recommended to have the position of the ball bearings in the cold section of the engine. The general configuration of the bearings type and position are illustrated in Figure 7.5.

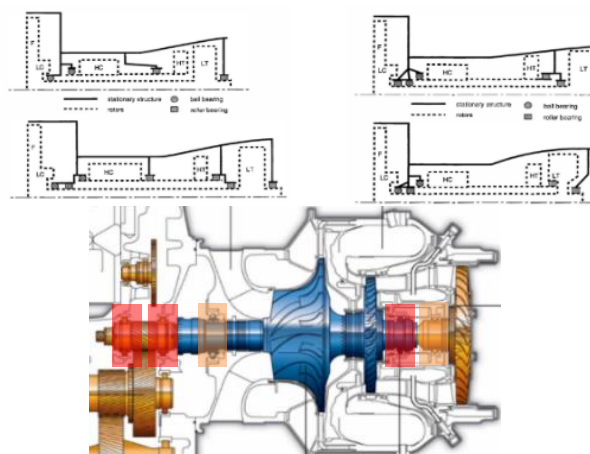


**Figure 7.4: Bearings' Positioning Examples [35]**

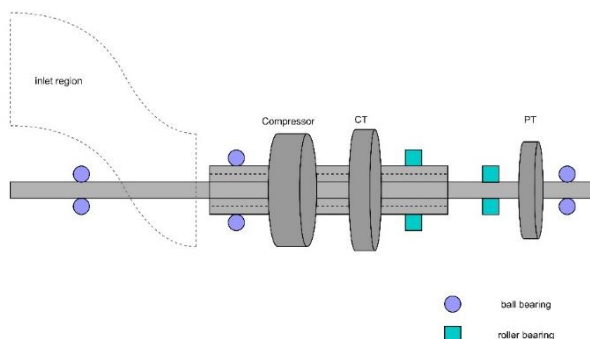


**Figure 7.5: Engine Bearings' Positioning of STS-1000**

### 7.5 Shaft Design

It should be recalled that the STS-1000 engine has two spools: a hollow shaft for the compressor turbine and one shaft for the power turbine. It should be noted that shaft material is Ti-5Al-2.5Sn.

Torsional moments and forces are computed by Eq.(7.1). The results are shown in Table 7.6.

$$M_t = \frac{\text{SHP} \times 63025}{\text{RPM}}, \text{ Force} = \frac{M_t}{R_{\text{mid}}} \quad (7.1)$$

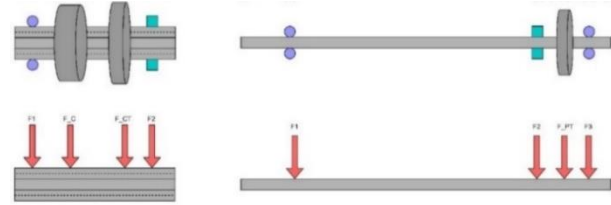


Figure 7.6: Position of the Forces

Table 7.6: Shaft Design Parameters

Parameter	Solid Shaft	Hollow Shaft	Parameter	Solid Shaft	Hollow Shaft	Parameter	Compressor	CT	PT
<b>K<sub>f</sub></b>	2	2	<b>Power [hp]</b>	953	1161.62	<b>R<sub>mid</sub> [in]</b>	5.53	4.56	5.3
<b>K<sub>τ</sub></b>	1.6	1.5	<b>Speed [rpm]</b>	220000	44210	<b>F [lbf]</b>	299.46	363.16	515.12
<b>F.S</b>	2.5	2.5	<b>M<sub>t</sub> [lbf.in]</b>	2730.13	1655.99				

According to Figure 7.7, the standard distance between the two shafts' radii is almost 0.2. Consequently, the inner radius is calculated [37].

$$d_{\text{inner, hollow shaft}} = 0.4 + d_{\text{solid shaft}} \quad (7.2)$$

Using the Eq. (7.3) and (7.4) and considering the safety factor, the initial shaft diameter is calculated [38].

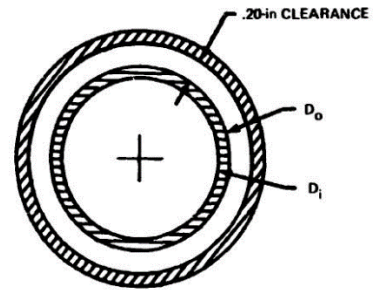


Figure 7.7: Cross Sections of Shafts

- **Solid Shaft** :  $d = \sqrt[3]{\frac{32FS}{\pi} \sqrt{k_f^2 \left( \frac{M_m}{S_y} + \frac{M_a}{S_e} \right)^2 + k_{fs}^2 \left( \frac{T_m}{S_y} + \frac{T_a}{S_e} \right)^2}} \quad (7.3)$

- **Hollow Shaft** :  $d_o = \frac{(d_o^4 - d_i^4)}{\frac{128 \times FS}{\pi} \sqrt{K_f^2 \left( \frac{M_m}{S_y} + \frac{M_a}{S_e} \right)^2 + K_\tau^2 \left( \frac{T_m}{S_y} + \frac{T_a}{S_e} \right)^2}} \quad (7.4)$

A schematic of the shaft geometry is illustrated in Figure 7.8. It should be mentioned that its modeling is discussed in rotor dynamic section.

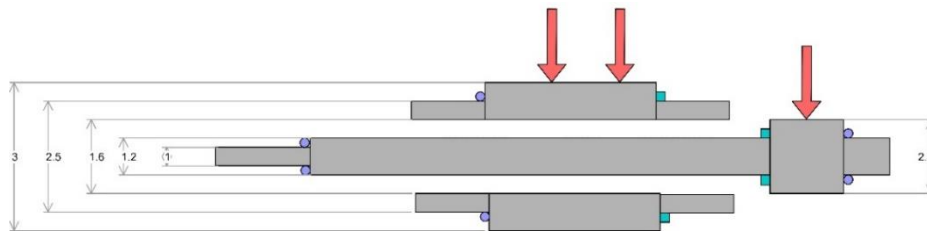


Figure 7.8: Schematic of Shafts and Diameter of Each Section

## 7.6 Shafts' Rotor Dynamic Analysis

Modeling of the shaft and the rotor dynamic analysis are presented. The analysis is done by using MESYS software.

### 7.6.1 Shafts Modeling

After having determined the bearings' positions, the shaft is modeled in MESYS, and the model is shown in Figure 7.9.

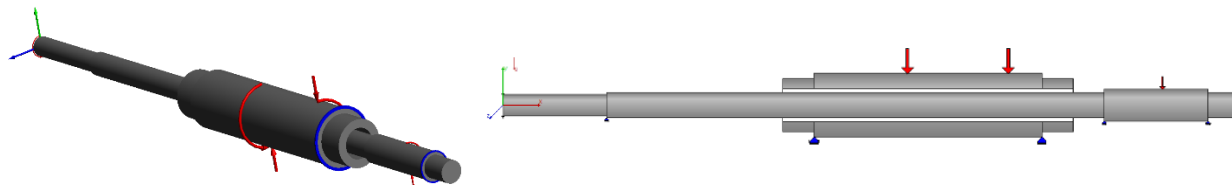
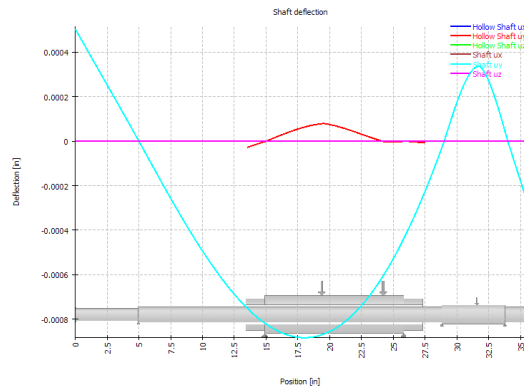


Figure 7.9: 2D and 3D Schematic of Shafts

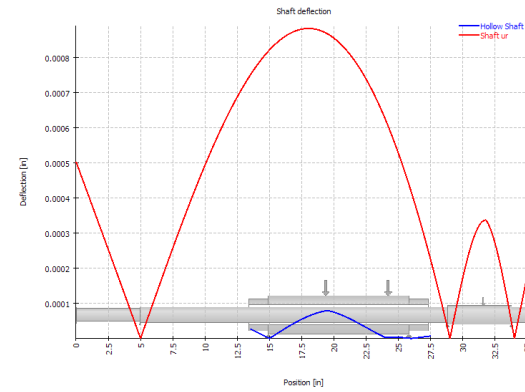
Campbell diagram and software results are explained in this section. Plots of deflection, forces, moments, and stresses are presented at Figure 7.10. In Table 7.7, natural frequencies are shown, and the Campbell diagram are shown in Figure 7.11.

Table 7.7: Natural Frequencies of Shafts

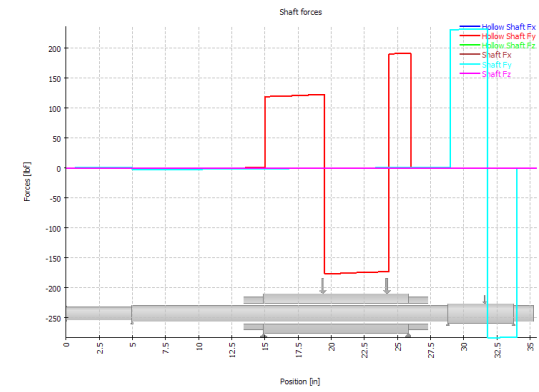
No.	Freq. [RPM]	Freq. [Hz]	Type	No.	Freq. [RPM]	Freq. [Hz]	Type
1	1	0.02	Torsional 'Hollow Shaft'	11	106427	1773.78	Radial 'Shaft', Backward whirl (-1.00)
2	5	0.08	Torsional 'Shaft'	12	107075	1784.59	Radial 'Shaft', Forward whirl (+1.00)
3	14476	241.26	Radial 'Shaft', Backward whirl (-1.00)	13	117332	1955.53	Radial 'Hollow Shaft', Backward whirl (-1.00)
4	14570	242.83	Radial 'Shaft', Forward whirl (+1.00)	14	122541	2042.34	Radial 'Hollow Shaft', Forward whirl (+1.00)
5	40558	675.97	Radial 'Shaft', Backward whirl (-1.00)	15	171287	2854.79	Radial 'Shaft', Backward whirl (-1.00)
6	40875	681.25	Radial 'Shaft', Forward whirl (+1.00)	16	172428	2873.8	Radial 'Shaft', Forward whirl (+1.00)
7	62097	1034.95	Radial 'Shaft', Backward whirl (-1.00)	17	224305	3738.41	Torsional 'Shaft'
8	62476	1041.27	Radial 'Shaft', Forward whirl (+1.00)	18	243857	4064.28	Radial 'Shaft', Backward whirl (-1.00)
9	101304	1688.4	Axial 'Shaft', Forward whirl (+0.72)	19	245767	4096.12	Radial 'Shaft', Forward whirl (+1.00)
10	103623	1727.05	Torsional 'Shaft', Forward whirl (+0.18)	20	262554	4375.9	Axial 'Hollow Shaft'



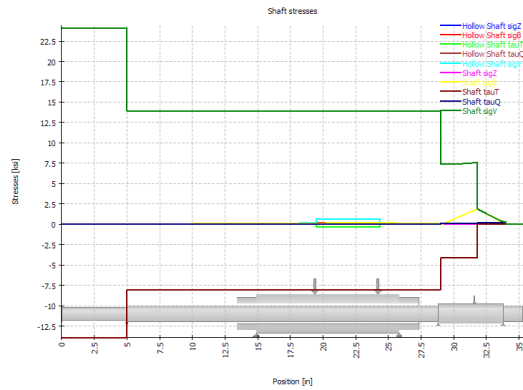
a) Deflection



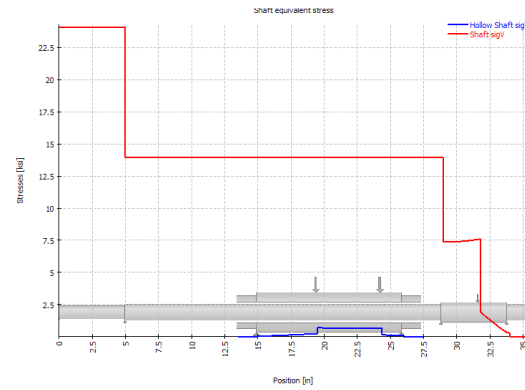
b) Radial Deflection



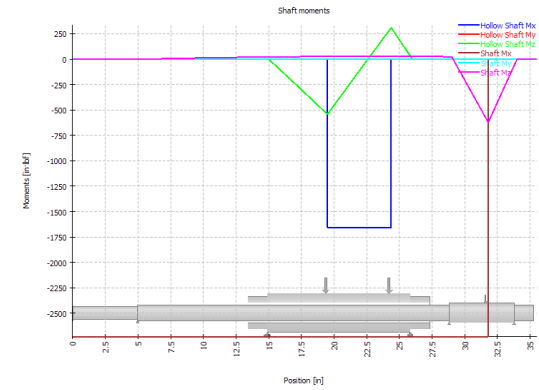
c) Force



d) Stresses



e) Equivalent Stresses on Shafts



f) Moments

Figure 7.10: Plots of Deflection (a, b), Forces (c), Stresses (d, e), and Moments (f)

Shafts mode shapes are as Figure 7.13 and Figure 7.13. Also, the Campbell diagram of the rotor dynamic analysis is shown in Figure 7.11.

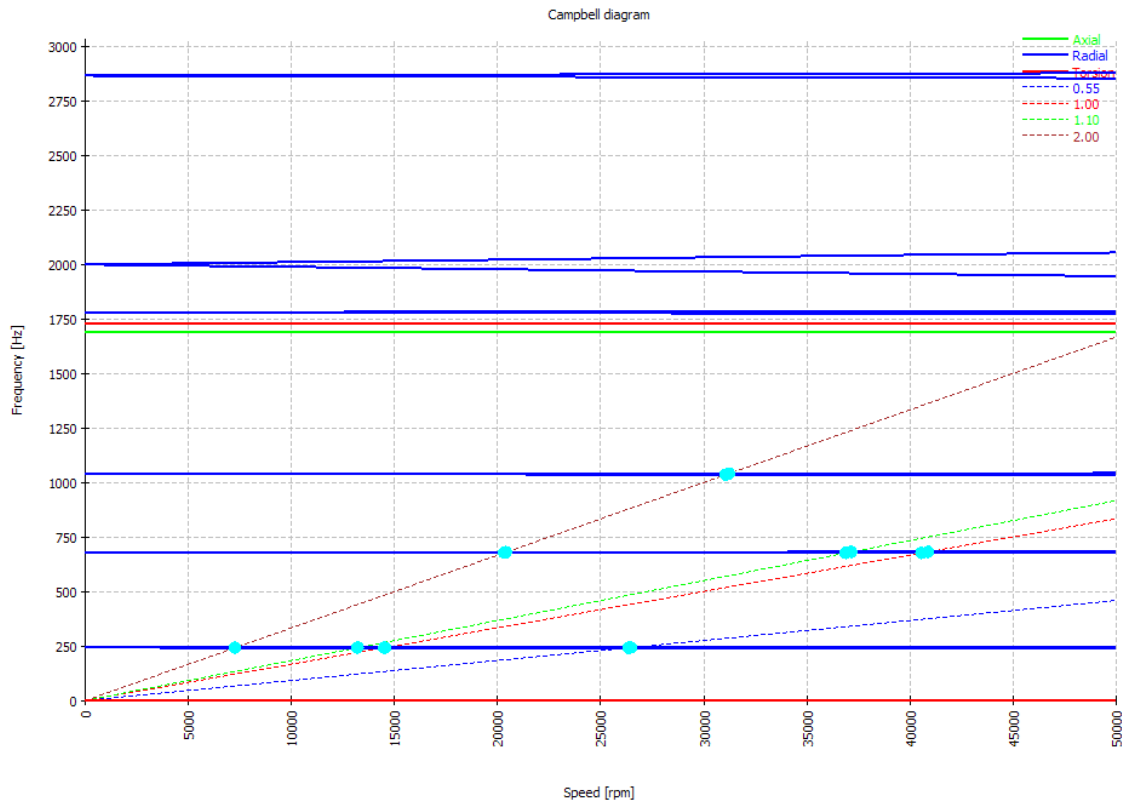


**Figure 7.11: Campbell Diagram**

Speed level for both shafts are shown in Table 7.8.

**Table 7.8: Shafts Speed Levels**

Speed Level	0.55	1.0	1.1	2.0
Element	Shaft (1X)	Hollow Shaft (1X)	Shaft (2X)	Hollow Shaft (2X)

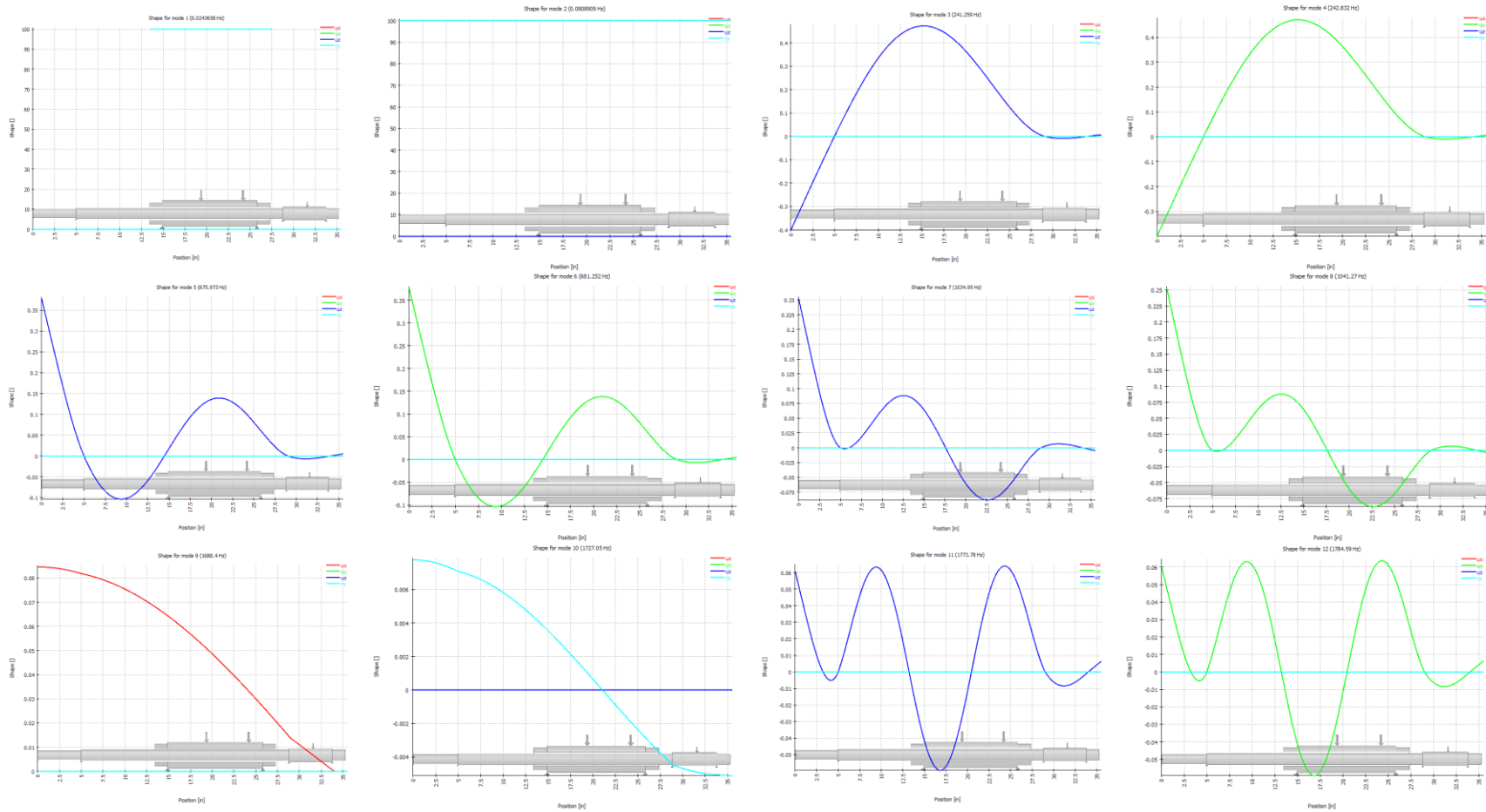


Figure 7.12: Shafts Mode Shapes

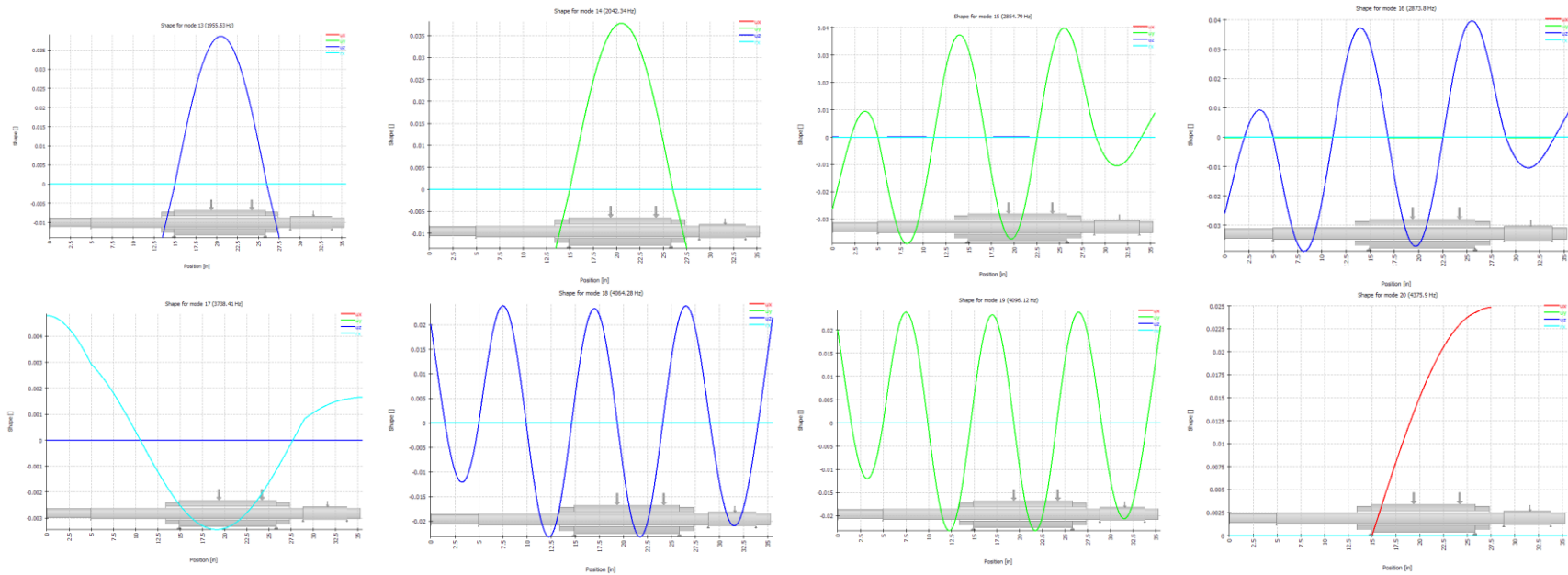


Figure 7.13: Shafts Mode Shapes (Continued)

## Chapter 8 Identification and Selection of Engine Subsystems

This chapter describes the subsystems that are used in STS-1000 engine. These subsystems provide essential features that are critical for the successful operation of any aircraft engine. First, the specifications and details of the oil and lubrication system are discussed. After that, fuel and engine control systems are explained in details.

### 8.1 Oil and Lubrication System

The main purpose of any lubricant is to reduce the friction contact interface between bearing and gear and reduce temperature [40]. The major components of a typical lubrication system are oil tank, oil pressure pump, and supply lines, scavenge pumps and return lines, filters and strainers, oil cooler, etc. (Figure 8.1) [39].

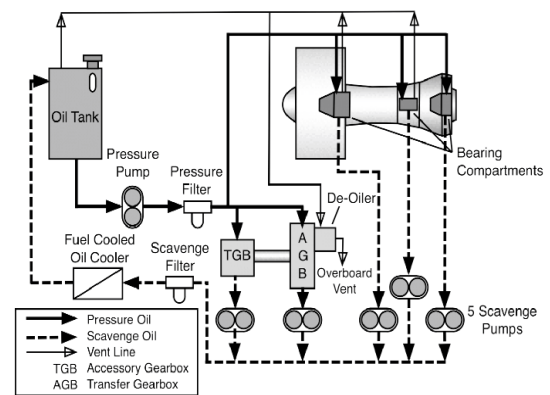


**Figure 8.1: A Typical Lubrication System [39].**

Considering the pressure regulation, there are two types of systems: the relief valve system, and the full flow system. In the relief valve system (or constant pressure system), the pressure at the pump exit is maintained at a specific value over the engine operating range by a relief valve that returns excessive oil into the tank. The full flow system operates without any pressure regulation device. Thus, the oil flow in the supply lines is a function of the operating speed of the pressure pump, the supply line, and oil nozzle cross sections and of the oil viscosity. This leads to changing oil pressure with changing engine shaft speeds [39].

The full flow system uses smaller pumps compared to the relief valve system. Such a system saves weight and is easier to adjust because it has no pressure regulating valve [39]. Hence, the lubrication system of the STS-1000 is selected to be a full flow system.

#### 8.1.1 STS-1000 Lube System

Engines use a wet-sump, dry-sump, or a combination of both as lubrication system. Wet-sump engines store the lubricating oil in the engine or gearbox. Dry-sump engines use an external tank mounted on the engine or somewhere in the aircraft structure near the engine. The dry-sump system carries a larger oil capacity, and an oil cooler is usually

included to control the temperature [40]. The STS-1000 engine employs a dry-sump high pressure as a lubrication system to cool the compressor and turbine bearings. This system consists of a high-pressure pump; five scavenge pumps, an oil filter with a bypass valve, a pressure regulator, and an oil tank.

### 8.1.2 Oil Cooling

To maintain the oil temperature within the set limits, it requires the installation of an oil cooler in the system. The cooling medium may be fuel, air, or a combination of them [42]. The oil cooler was chosen as a Fuel-Oil Heat Exchanger (FOHE). The Fuel-Oil Heat Exchanger cools the hot oil and preheats the fuel for combustion [40]. It has a smaller volume compared to an air-oil heat exchanger of the same cooling capacity. In addition, this system is effective the during ground operation and increases the combustion efficiency [39].

### 8.1.3 Oil Selection

For oil selection, the standard for current and near-future engines follow the lubricating oil performance specification, MIL-PRF-23699F STD or O-156 [43]. The STS-1000 engine uses the AeroShell Synthetic Turbine Oil 500 since it meets and exceeds the performance specification. The above-mentioned oil type has the following characteristics:

- It has low enough viscosity to flow readily between tightly fitted, rapidly moving parts. Also, it has a high enough viscosity to prevent metal-to-metal wear.
- It does not break down under high temperatures and pressures.
- It has a low enough pour point to flow readily when starting under extremely low temperatures.
- It has a high enough flash and fire point, so it does not burn or vaporize under high heat. [40]

The properties of this lubricant are shown in Table 8.1

**Table 8.1: AeroShell 500 Oil Properties Compared to Mil-Spec [43]**

Properties	MIL-PRF-23699G Grade STD SAE AS5780B Grade SPC	AeroShell 500 Typical Properties
Oil type	Synthetic ester	Synthetic ester
Kinematic viscosity [mm <sup>2</sup> /s]		
@ 100 °C	4.90 to 5.40	5.17
@ +40 °C	23.0 min	25.26
@ -40 °C	13000 max	8996
Flashpoint Cleveland Open Cup [°C]	246 min	256
Pourpoint [°C]	-54 max	<-54

## 8.2 Fuel System

The engine fuel system purpose is to pressurize, control, and atomize the fuel into the combustion chamber to satisfy the speed and power demands on the engine [42]. It includes an engine driven fuel pump, a fuel control assembly, and fuel-oil heat exchanger. The STS-1000 engine uses an electronically controlled fuel system, with signals from full authority digital engine control (FADEC). The fuel shut-off valve is electrically actuated during the start cycle and upon engine shutdown and can be closed manually by actuating the fuel shutoff or feather handle.

## 8.3 Engine Control System

The STS-1000 engine control is provided by use of FADEC (Full Authority Digital Engine Control). FADEC provides complete control of the engine, functions are performed automatically, and thus the pilot/flight control system workload is reduced. The main task of the FADEC are fuel control, isochronous power turbine speed control (maintains a constant rotor speed), acceleration control, limitation of the turbine temperature, engine speeds and torque, IGV actuator, etc.

If a FADEC system is used for engine control, this has the advantage that its logic can process the influencing parameters faster than a hydromechanical control system [39]. Therefore, this capability of the system is used for additional functions to optimize the engine operation. Additional to the basic engine control functions of power management and fuel control the following functions are usually assigned to the system [44].

- Monitoring and fault detection for the system and all the connected components
- Data source for engine indication
- Starting, shutdown and ignition control

The basic engine control concept is shown in Figure 8.3. A closed-loop control system is often adopted for aircraft engine control to obtain a better tracking ability and increase its robustness. Figure 8.2 shows a closed-loop control system block diagrams for a typical process. Condition monitoring is considered a major part of preventive maintenance [44]. Maintenance cost and time can be reduced by “Condition Monitoring” carried out by the FADEC.

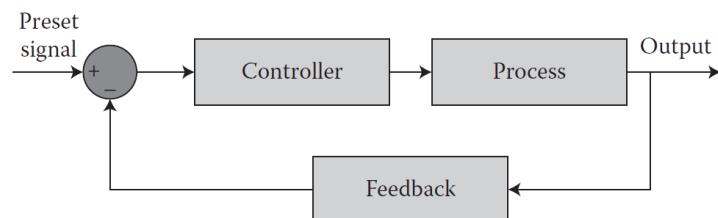


**Figure 8.2: Block Diagram of a Closed-Loop Control System [44].**

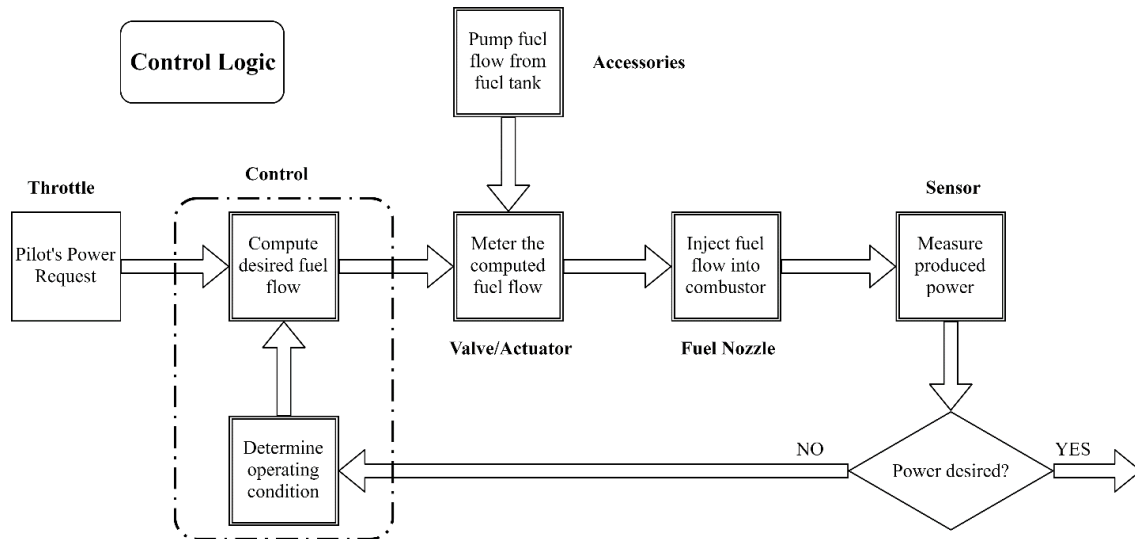


Figure 8.3: Functional Process Diagram of a Simple Engine Control System [45].

## Chapter 9 Cost Analysis

This chapter discusses the candidate engine cost analysis. To estimate the engine cost, based on available references, three main cost types are defined: unit cost, maintenance cost, and operating cost. It is tried to compare the total and maintenance and operating cost of TPE331-10 with STS-1000.

### 9.1 Unit Cost

Regarding the engine parameters such as TIT and thrust, the engine unit cost can be estimated, based on [46]. By this way, candidate engine unit cost is about 25% more expensive than baseline engine since it utilizes more advanced materials and more complex manufacturing.

### 9.2 Maintenance Cost

The following parameters are used in maintenance cost estimation: maintenance intervals, shop visit man hour per engine flight hour, the material cost in shop visit, and life limited part cost. Shop visit timelines and maintenance cost is calculated by using compressor stage number, compressor and turbine blades velocity, temperature, and pressure of each part which are introduced in [47].

#### 9.2.1 Maintenance Intervals (Shop Visit)

In the shop visit, engine parts are inspected and in the case of failure or defect, will be replaced. Shop visit times varies with UAV range. It is assumed that the UAV is a medium-range according to [48]. By considering the thrust and weight of the engine, after 28000 flight hours engine should be overhauled.

#### 9.2.2 Shop Visit Man Hour per Engine Flight Hour

The required labor hour during a shop visit is described herein. Man hour is determined based on engine operating hours which first and second shop visits determine this amount. The first shop is required to have about 0.48 man hour per engine flight hour and 1.06 man hour per engine flight hour for the second shop visit.

#### 9.2.3 Material Cost

Cost of materials is an expense which will be spent on changing some components of the engine in shop visit. By using [47], it will be seen that about 20 percent of engine unit cost should be spent on the material in each overhaul.

### 9.2.4 Life-limited Part Cost (LLP Cost)

Relating to the range of target UAV, after specific operation time, some engine components such as turbine and compressor need to be changed entirely. LLP cost reflects expenditures for the LLP replacement. This cost can be estimated by using [48]. It can be seen that LLP cost for the candidate engine is about the same as baseline engine in each engine flight cycle but it can be achieved that due to higher endurance of STS-1000, its LLP cost per hour is about 23 percent less than TPE331-10.

In Table 9.1 the comparison of maintenance parameters of STS-1000 and the baseline engine is shown.

**Table 9.1: Comparison of Maintenance Cost**

Maintenance parameters	STS-1000	TPE331-10
Maintenance intervals [engine flight hour]	28000	29000
Shop man hour per engine flight hour (first shop visit)	0.48	0.54
Shop man hour per engine flight hour (second shop visit)	1.06	1.2
Material cost in the shop	0.2 of unit cost	0.2 of unit cost
LLP cost [engine flight hour]	23% less than baseline	

### 9.3 Operating Cost

An engine operating cost comparison is done between STS-1000 and TPE331-10 herein based on engine flight hour. This comparison is based on engine fuel consumption, cost of materials, labor shop visit cost [47], and LLP cost [48]. As it can be seen in Figure 9.1, which the costs are scaled to the operating cost of the baseline engine. the material operating cost of candidate engine is more expensive than

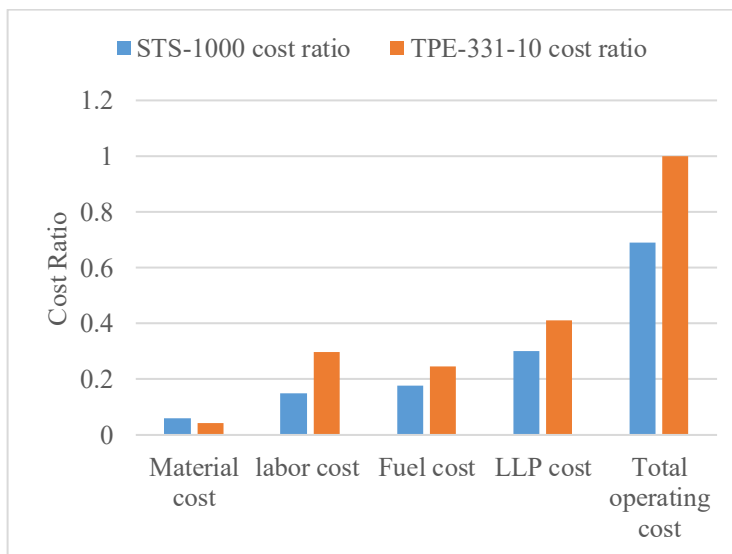


**Figure 9.1: Operating Cost Comparison**

the baseline engine. However, the fuel cost per hour of STS-1000 is less than the baseline engine due to better fuel consumption. Eventually, STS-1000 operating cost is 30% less than the baseline engine.

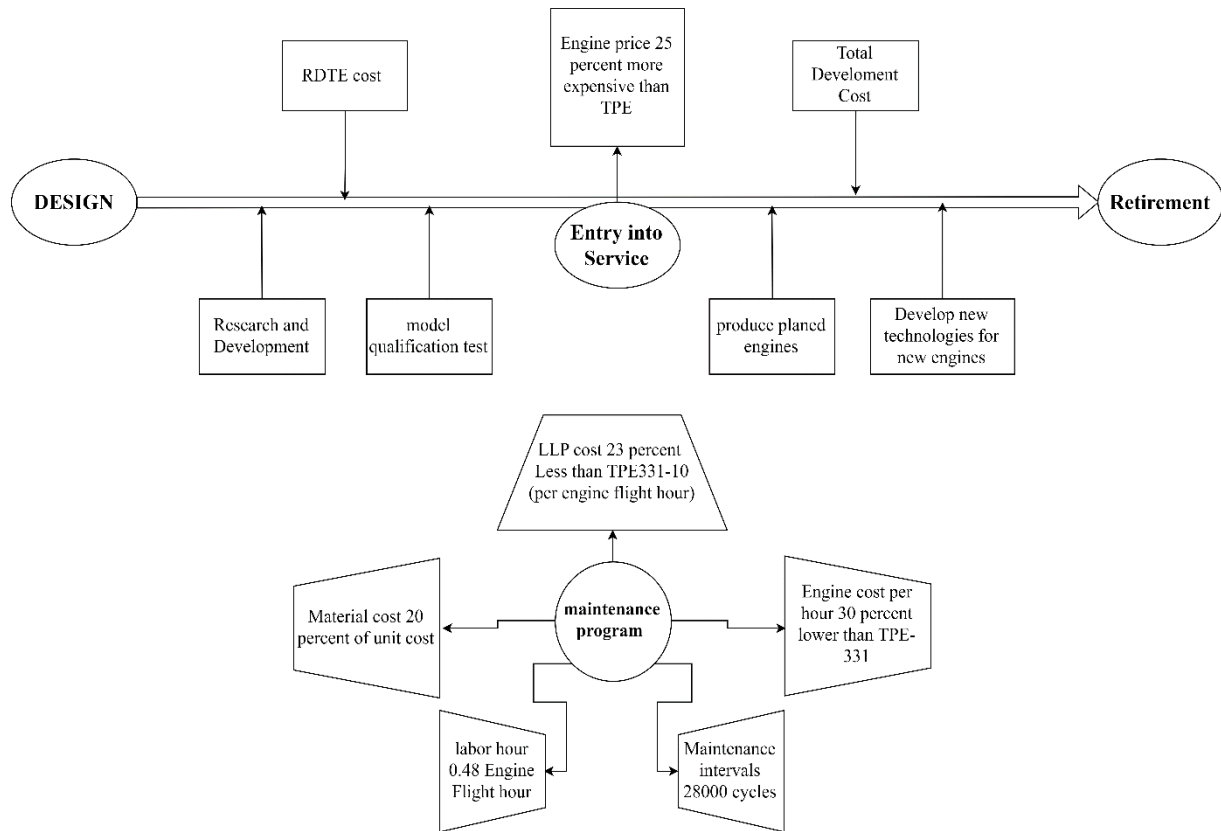


**Figure 9.2: Flowchart of STS-1000 Engine Cost**

## Chapter 10 Engine Weight Estimation

To estimate the engine weight, CAD volumes and density of selected materials are used. Also, for the components such as accessories, and oil system which are not included in the CAD model, their weight is estimated from estimations in references. In this section, the below items result in significant weight reduction compared to the baseline engine.

- High-Tech and lighter materials are used
- The compressor stages are reduced to one stage
- Dimensions and volume of the engine are approximately reduced by 30%
- There is no need for the gearbox since PT rotational speed is constant

Therefore, based on engine components modeling, calculating their volumes, and the density of selected materials, the weight of each component is shown in Table 10.1

**Table 10.1: Engine Components Volume, Density, Weight**

Component	Material	Volume [in <sup>3</sup> ]	Density [lb/in <sup>3</sup> ]	Weight [lb]
<b>Intake</b>	S-2 Glass Epoxy composite	15.01	0.129	1.93
<b>Shaft</b>	Titanium-5Al-2.5Sn	41.6	0.162	6.73
<b>Halo shaft</b>	Titanium-5Al-2.5Sn	64.33	0.162	10.42
<b>Compressor</b>	Titanium-6Al-4V	128.34	0.16	20.53
<b>Combustor</b>	SiC/SiC CMC	180.36	0.112	20.2
<b>Turbine</b>	SiC/SiC CMC	5.27	0.112	0.6
<b>Disks</b>	Inconel 718	162.25	0.296	48.26
<b>Nozzle</b>	Inconel 22	11.55	0.324	3.74
<b>Sum</b>				<b>112.41</b>

To estimate engine accessories which includes power plant controls, accessory drives, oil cooler, and ignition system, oil, and starting, the weight estimation method is used [49]. Also, the casing of the engine is about 15% of engine weight statistically [50], the above amounts are about 85% of the engine's weight. Therefore, the weight of each component and engine total weight is detailed in Table 10.2.

**Table 10.2: Final Engine Weight**

Engine Components Weight [lb]	Accessories weight [lb]	Casing Weight [lb]	Dry engine weight [lb]
112.41	103	38.01	<b>253.42</b>

Hence, STS-1000 weight is 34.17% lighter than the baseline engine.

# Chapter 11 Engine Flow Path and 3D CAD

Regarding Chapter 7, the material properties of each component are shown in Table 11.1. The cross-section, flow path, and each component material of the STS-1000 are shown in Figure 11.1.

**Table 11.1: Material Properties of each Component**

Component	Material	Density [lb/in <sup>3</sup> ]	Max Service temperature [F]	Tensile Strength, Yield [psi]
<b>Intake</b>	S-2 Glass Epoxy composite	0.129	350	350266
<b>Shaft</b>	Titanium-5Al-2.5Sn	0.162	896	120000
<b>Hollow Shaft</b>	Titanium-5Al-2.5Sn	0.162	896	120000
<b>Compressor</b>	Titanium-6Al-4V	0.16	783	133000
<b>Combustor</b>	SiC/SiC CMC	0.112	2550	363000
<b>Turbine</b>	SiC/SiC CMC	0.112	2550	363000
<b>Discs</b>	Inconel 718	0.296	1300	160000
<b>Nozzle</b>	Inconel 22	0.324	1800	52900
<b>Bearing Balls &amp; Rollers</b>	AISI M50NiL	0.285	752	174000
<b>Bearing Cages</b>	SAE 4340	0.284	1099	103000

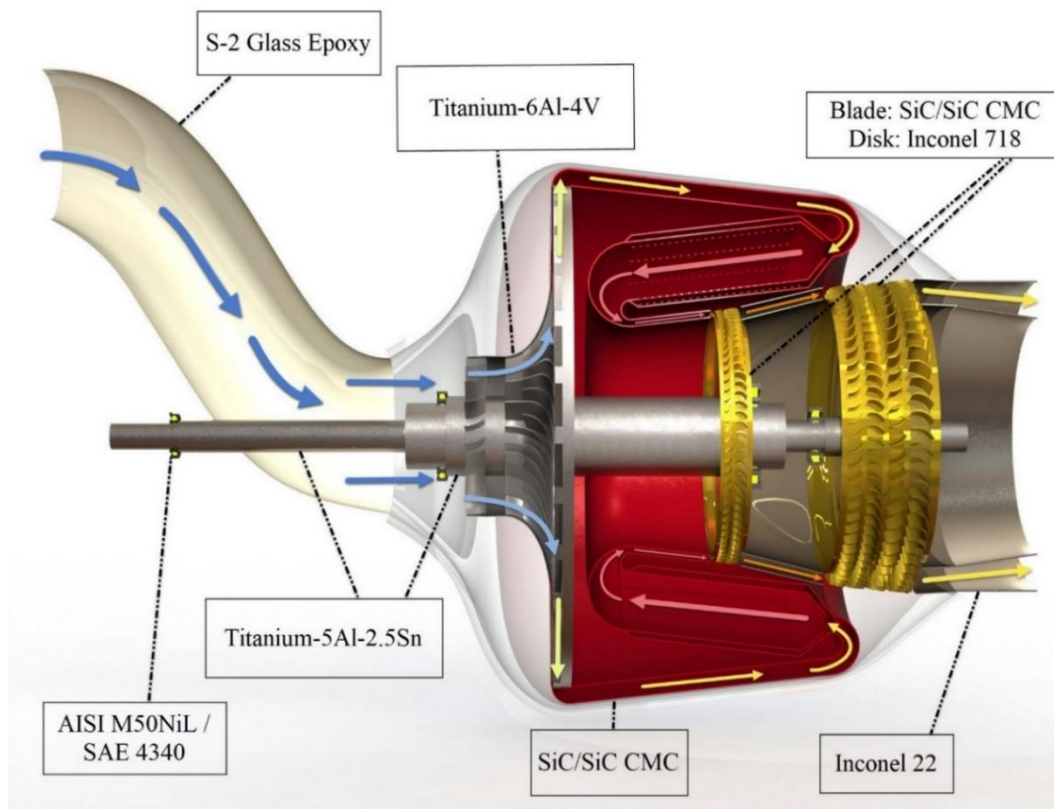


**Figure 11.1: STS-1000 Cross-section and Flow Path**

Finally, the 3D CAD model of the STS-1000 engine and its compressor, combustion chamber, turbines, and shafts are as follows:

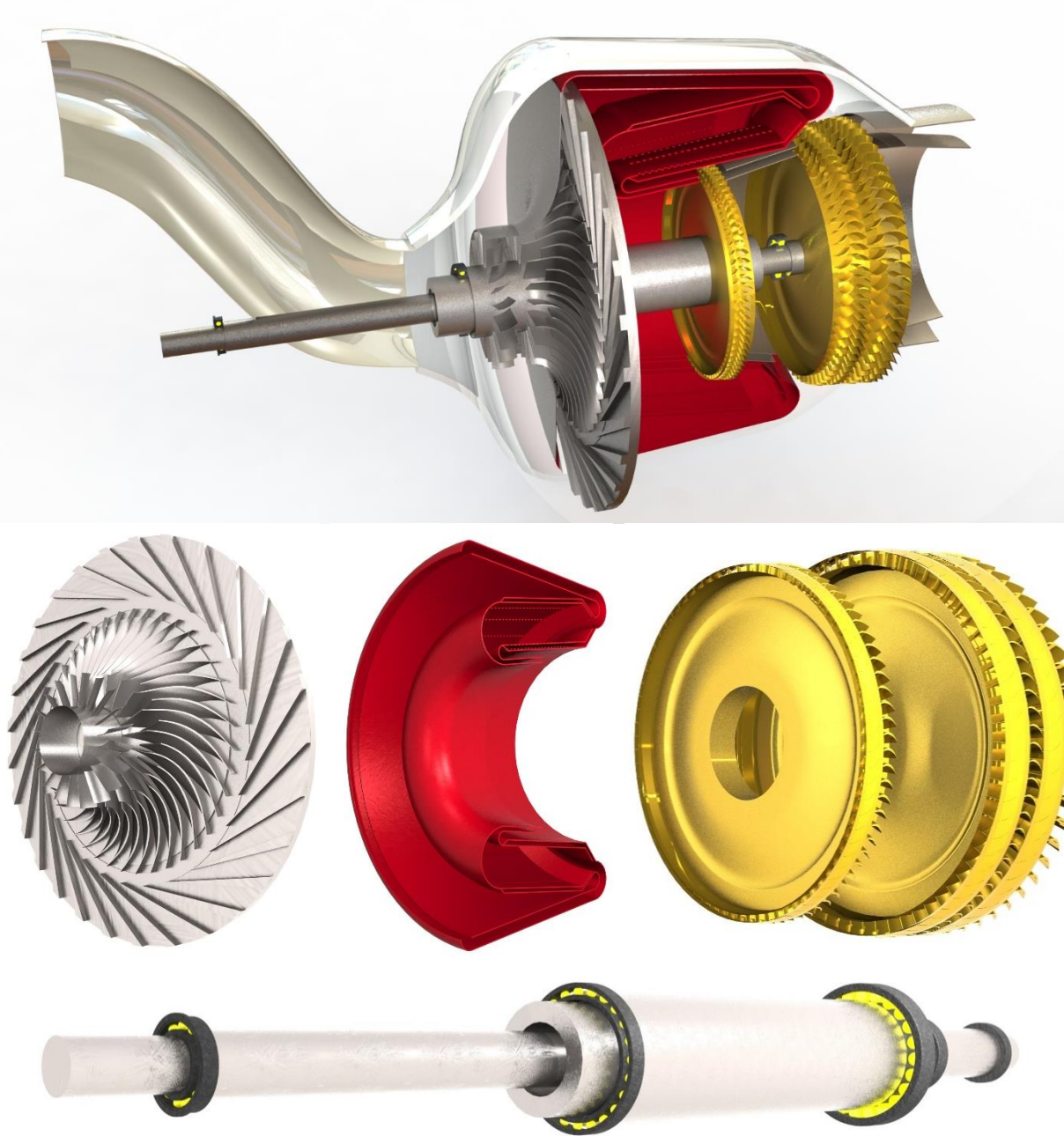


Figure 11.2: STS-1000 Engine 3D CAD Model

## Chapter 12 Conclusion and Recommendation

A split single-shaft turboshaft engine referred to “Sharif TurboShaft 1000 (STS-1000)” is designed as a candidate engine to replace TPE331-10 for the next generation “Hybrid Electric Medium Altitude Long Endurance Search and Rescue UAV” by the year 2025. STS-1000 consists of a hot gas generator (HGG) and a split power turbine (PT). The hot gas generator contains a single stage centrifugal compressor, a reverse annular combustion chamber, and an uncooled single stage axial compressor turbine whereas the power turbine has two axial stages. While the spools of the PT and HGG are split and thus only fluid-mechanically coupled to each other; however, the PT-spool runs through the HGG-spool and is intended to drive a power generator at the cold end of the HGG.

As outlined in this report, compared to TPE331-10, STS-1000 has a higher turbine inlet temperature, a lower stage number for the air compressor, and requires less mass flow rate. Therefore, STS-1000 has not only a lower weight due to both shorter engine length and smaller air capture area but also has higher degree of flexibility for engine-airframe integration. As a result, while the engine could easily be positioned inside the UAV airframe, the required air mass flow rate could be fed by a S-type air intake.

Further, the rotor components (i.e., AC, CT, and PT) have relatively higher efficiencies due to recent and foreseen technological advancements in aerodynamics and materials. As a consequence, STS-1000 has not only higher thermal efficiency and lower specific fuel consumption but also higher power-to-weight ratio. This enables the UAV either to execute longer loiter times and/or carry heavier payload. In addition, STS-1000 is very compact, low in complexity, and might even be considered for being scaled-up if required. The proposed engine has higher life cycle and lower maintenance cost.

Furthermore, it should be emphasized that in addition to commercial software (GSP11 and MESYS) used in this report, few codes are also developed in the MATLAB® environment. These codes are used to (1) compute the cycle analysis of both TPE331-10 and STS-1000 engines at the design point and off-design conditions, (2) identify the design point for the STS-1000, and (3) to carry out the aero-thermodynamic analysis across the AC, CT, and PT, air intake, and the exhaust duct. It should be mentioned that for identifying the design point for the STS-1000 a methodology is developed rather than a simple try and error approach or a shooting technique.

# References

- [1] Foundation, A., Design, S., & Team, U. (2018). Candidate Engines for a Hybrid Electric Medium Altitude Long Endurance Search and Rescue UAV-Request for Proposal. 1–17.
- [2] GSP Development Team. (2014). GSP 11 licensed to Team FARAS.
- [3] Mattingly, J. D., Ohain, H. Von, & Schetz, J. A. (1801). “Elements of Propulsion : Gas Turbines and Rockets Department of Mechanical Engineering.”
- [4] El-Sayed, A. F. (2016). Fundamentals of aircraft and rocket propulsion. In *Fundamentals of Aircraft and Rocket Propulsion*. <https://doi.org/10.1007/978-1-4471-6796-9>
- [5] Benzakein, M. J., GE Aircraft Engines “The Future of the Jet Engine,” Cincinnati, OH, USA, Spring, 2017.
- [6] <http://www.ga-asi.com/predator-b2818>
- [7] A. Whitfield, N.C. Baines - Design of Radial Turbomachines-Longman (1990).pdf. (n.d.).
- [8] EASA Arrius Type-Certificate Data Sheet
- [9] William J. McAnally, “10:1 Pressure Ratio Single Stage Centrifugal Compressor Program.”  
Osborne, C., Osborne, C., Runstadler, P. W., Runstadler, P. W., Stacy, W., & Stacy, W. (1975).
- [10] Aerodynamic and Mechanical Design of an 8:1 Pressure Ratio Centrifugal Compressor. Nasa Cr-134782, 147.
- [11] Nagpurwala, H. (n.d.). Design of Centrifugal Compressor-1. 1–60.
- [12] “Centrifugal Compressor-A strategy For Aerodynamic Design and Analysis (2000)”, Aungier.pdf. (n.d.).
- [13] Chatwin, C. R. (2017). Design & Manufacture of Gas Turbines for Aircraft by University of Sussex. (April). <https://doi.org/10.13140/RG.2.2.35884.05760>
- [14] Borisavljević, A. Limits, Modeling and Design of High-Speed Permanent Magnet Machines. Ph.D. Thesis, Delft University of Technology, Delft, The Netherlands, 2011.
- [15] Aerospace, D., München, M. T. U., Royce, R., & Gmbh, M. T. R. (2001). The successful development history of the mtr390 turboshaft engine from the definition of the design to the series production.
- [16] Dixon, S. L., & Hall, C. A. (2010). Fluid mechanics and thermodynamics of turbomachinery. Burlington, MA: Butterworth-Heinemann/Elsevier
- [17] E. A. Baskharone, *Principles of Turbomachinery in Air-Breathing Engines*. Cambridge: Cambridge University Press, 2006
- [18] Lewis, R. I. (1996). Turbomachinery performance analysis. London: Arnold.
- [19] Farokhi, S., “*Aircraft Propulsion*.” 2nd Edition, John Wiley & Sons Ltd, West Sussex, United Kingdom, 2014. Print.
- [20] Aungier, R. H. (2006). *Turbine aerodynamics: Axial-flow and radial-inflow turbine design and analysis*. New York: ASME Press.
- [21] Schobeiri, M. T. (2017). Gas turbine design, components and system design integration. In *Gas Turbine Design, Components and System Design Integration*
- [22] H.I.H. Saravanamuttoo, G.F.C. Rogers, and H. Cohen, *Gas Turbine Theory*, Prentice Hall, 5th edn.,2001, p. 313.
- [23] Lefebvre, A. H., & Ballal, D. R. (2010). Gas turbine combustion: Alternative fuels and emissions. Boca Raton: Taylor & Francis.
- [24] Melconian, J.W. Modak, Combustors design, in: Sawyer's Gas Turbine Engineering Handbook: Theory & Design, Vol.1, 1985, Turbomachinery International Publications, Connecticut

- [25] Joachim Kurzke, Ian Halliwell, “*Propulsion and Power, An Exploration of Gas Turbine Performance Modeling*” Springer International Publishing 2018.
- [26] Rajiv Ranjan. Performance Evaluation Of Conventional Turboprop Engines
- [27] Ghorbanian, K., “Aircraft Engine Design Course”, Sharif University of Technology, Spring 2017-18
- [28] Yurko, I., & Bondarenko, G. (2014). A New Approach to Designing the S-Shaped Annular Duct for Industrial Centrifugal Compressor. International Journal of Rotating Machinery, 2014
- [29] Rosenthal, H., D. Nelepovitz, and H. Rockholt. De-Icing of Aircraft Turbine Engines. Tech. no. DOT/FAA/CT-87 /37. N.p.: n.p., n.d. Print.
- [30] Ph. Joubert, M.L Ortiz, S. Durand, P. B. (n.d.). Acoustic Liners Integration on a Turboshaft Engine.
- [31] MESYS engineering consulting software, version 10-2018, licensed to Team FARAS
- [32] <http://www.matweb.com/search/DataSheet.aspx?MatGUID=a20cd777870348a7a8ca82739d76eaf1>
- [33] 47. Halbig, M., Jaskowiak M., Kiser J., and Dongming Z. "Evaluation of Ceramic Matrix Composite Technology for Aircraft Turbine Engine Applications." Composites 22.1 (1991): 73. NASA. Web. 10 Feb. 2017
- [34] Thomson, W. T., & Dahleh, M. D. (1997). *Theory of Vibration with Applications-Prentice Hall (1997).pdf*.
- [35] Kerrebrock, J. L. (1977). *Aircraft Engines and Gas Turbines*.
- [36] <http://freepatentsonline.com/7926291.html>
- [37] R. J. Pera. E. Onat, G. W. Klees. E. Tjonneland (1855). A Method to Estimate Weight and Dimensions of. (May 1977). National Aeronautics & Space Administration
- [38] Budynas, R. G., Nisbett, J. K., & Shigley, J. E. (2011). Shigley's mechanical engineering design. New York: McGraw-Hill
- [39] Andreas Linke-Diesinger, “*Systems of Commercial Turbofan Engines, An Introduction to Systems Functions*” 2008 Springer-Verlag Berlin Heidelberg
- [40] "Chapter 5 *Jet Aircraft Engine Lubrication Systems - Navy Bmr.*"
- [41] <http://www.flight-mechanic.com/turbine-engine-lubrication-systems/>
- [42] TPE331 Pilot Tips
- [43] "AeroShell Synthetic Turbine Oil 500 Data Sheet." Global Industrial Solutions.
- [44] Asgari, H., & Chen, X. “*Gas Turbines Modeling, Simulation, and Control Using Artificial Neural Networks.*” Taylor & Francis Group, LLC.
- [45] Dr. Sanjay Garg. Fundamentals of Aircraft Turbine Engine Control.
- [46] Birkler, J. L., Garfinkle, J. B., & Marks, K. E. (1982). Development and production cost estimating relationships for aircraft turbine engines.
- [47] Kang, M., & Ogaji, S. (2008). GT2008-50564 Air Transport Association of America. Asme & Gt, 1–9..
- [48] Seemann, R., Langhans, S., Schilling, T., & Gollnick, V. (2011). Modeling the Life Cycle Cost of Jet Engine Maintenance Air Transport System View project IATA Technology
- [49] Roskam, J. (1997). Airplane design. Lawrence, Kan: DARcorporation.
- [50] Pantalone, G., Blanco, E. de la R., Wilcox, K., Reduction, P. for A. T. N. and E., & Administration, F. A. (2016). TASOPT Engine Model Development